Topology Optimization and Failure Analysis of Deployable Thin Shells with Cutouts

Thesis by
Serena Ferraro

In Partial Fulfillment of the Requirements for the
Degree of
Doctor of Philosophy

CALIFORNIA INSTITUTE OF TECHNOLOGY
Pasadena, California

2020
Defended December 2, 2019

Serena Ferraro
ORCID: 0000-0002-6038-7863

ACKNOWLEDGEMENTS

When I first came to the United States I did not have a clear idea of where my path would lead me, but I can certainly say that I could have never imagined it leading me to the completion of a Ph.D. at Caltech. How could I belong to such a prestigious school, where some of the most brilliant minds have made incredible discoveries in different fields of science? Yet, here I am today, filled with gratitude towards all the wonderful people that supported me and believed in me when I could not.

First and foremost, I want to thank my advisor Professor Sergio Pellegrino. He has guided my research efforts and always encouraged me to strive for excellence. Whether in our one-to-one or weekly group meetings, he has taught me the importance of persevering in one's efforts and growing from one's mistakes. Amongst the countless, invaluable lessons I can mention here, I will acknowledge a very recent one by paraphrasing his own words: "While everyone might have a little fear of criticism in presenting novel research, one should always seek criticism to improve their work rather than settling for consensus. It is a matter of character."

I would also like to thank all members of my candidacy and defense committees: Prof. Guruswami Ravichandran, Prof. Chiara Daraio, Prof. Kaushik Bhattacharya, and Dr. Mehran Mobrem. Their feedback has had a very positive impact on my research.

I extend my gratitude to my mentors and collaborators at JPL and NASA Langley who worked with me during my NASA Space Technology Research Fellowship (NSTRF) internships. Dr. Bill Doggett and Dr. John Dorsey made me feel welcomed from the very first day at NASA Langley. I have received great feedback and support from them. Dr. Case Bradford has introduced me to the wonderful world of the Jet Propulsion Laboratory for which I fell in love with. It is also because of his mentorship that I decided to join the JPL family after graduation.

I want to acknowledge my soon-to-be employers and mentors Young Lee, Peter Kahn, and Randy Herrera for giving me the opportunity of a lifetime. They have made my last year at Caltech so much more fun, thinking that all my hard work had paid off and that I would joint JPL as I have always dreamed to. I am excited to start my career with them. I also want to sincerely thank the person who made this possible, Dr. Kristina Hogstrom. She has mentored me since I first joined Caltech and has always been an inspiration to me.

I am thankful for financial support from my NSTRF fellowship that allowed me to pursue research in deployable space structures. Equally, I want to thank the Keck Institute for Space Studies (KISS) that supported me during my first year at Caltech. I extend my gratitude to Prof. Tom Prince, for welcoming me into the KISS family, and to Michele Judd, for the elegance with which she juggles so many responsibilities. Michele is a role-model to me, a person of integrity, passion, and grit who carries on her work tirelessly and always with a smile.

I want to thank the entire GALCIT community for making our graduate student lives much easier. My gratitude goes to Prof. Beverley McKeon and Prof. Dan Meiron who helped me navigate through the subtleties of obtaining my master's degree, choosing my candidacy and defense committees, and so on. I am also grateful to Kate Jackson, Christine Ramirez, Rosemary Cheng (Binh), Peggy Blue, Dimity Nelson, Jamie Meighen-Sei, Stephanie Rider, and Petros Arakelian. I also want to thank the GALCIT machine shop, Joe Haggerty and Ali Kiani, for patiently interpreting my drawings and helping with last minute issues. A heartfelt thank you goes to Dr. Jackie Gish, who has been there to support me both personally and professionally. I have learned a great deal from her and often sought her advice and am thankful for it.

I am grateful for being part of the Autonomous Assembly of a Reconfigurable Space Telescope (AAReST) project and I thank the mission leaders at Caltech, John Baker and Dr. James Breckinridge, for mentoring us through the project. I also want to thank my Ae105 instructors, Dr. Greg Davis, Dr. Anthony Freeman, and Dr. Dan Scharf for providing my very first insight into a space mission.

I want to acknowledge Prof. Ole Sigmund for welcoming me to his class on topology optimization at the Technical University of Denmark. I am grateful for his honest feedback to my research and for his dedication to this exciting field, which sparked my curiosity and led me to detailed studies on the subject.

I would like to thank my colleagues and labmates at the Space Structures Laboratory (SSL) at Caltech, both past and present, for their moral and technical support. They have listened to my presentations, helped me building prototypes, reviewed my manuscripts, troubleshot equipment, and most importantly shared so many good times with me: Dr. Manan Arya, Dr. Miguel Bessa, Dr. Stephen Bongiorno, Dr. Federico Bosi, Max Braun, Dr. Luke Chen, Dr. Melanie Delapierre, Charles Dorn, Dr. Terry Gdoutos, Dr. Ashish Goel, Dr. Armanj Hasanyan, Dr. Kristina Hogstrom, Dr. Kathryn Jackson, Dr. Wilfried Jahn, Uba Kanthasamy, Dr. Christophe Leclerc,

Corentin Lubeigt, Dr. Yang Li, Dr. Chinthaka Mallikarachchi, Michael Marshall, Antonio Pedivellano, Harsha Reddy, Fabien Royer, Dr. Maria Sakovsky, Arthur Schlothauer, Charles Sommer, Dr. John Steeves, Dr. Thibaud Talon, Alan Truong, Dr. Yuchen Wei, Alexander Wen, Fabian Wiesemueller, and Dr. Lee Wilson.

My gratitude goes to the one person who gave me a chance when no one else would, Prof. Valeria La Saponara. Not only she offered me a position in her composite materials laboratory at UC Davis, but she allowed me to attend her classes and welcomed me into her life. She is the most generous, kind-hearted, and selfless person I know, and I look up to her both personally and professionally.

I want to thank my dearest friends who shared with me the struggles and joy of our first year at Caltech. Without them I would have never made it through that challenging year: Kevin Bonnet, Christopher Chatellier, Dr. Chandru Dhandapani (Gigi), Dr. Cecilia Huertas, Dr. Christophe Leclerc, Dr. Matthew Leibowitz, Kirsti Pajunen, Dr. Greg Phlipot, Dr. Jean-Christophe Veilleux, Dr. Vidyasagar, and Dr. Nelson Yanes. I also want to thank those who made me part of their lives in the United States and became a family away from home: James Christensen and Hazel Lim, Prof. Riccardo and Maddalena De Salvo, Erik Dygulski and Mollie McCabe, Rudy Hernandez and his wonderful family, Tony and Emily Gomez, Siavash Peiday Saheli, Dr. Akshay Sridhar, and Joey and Alex Traina.

I am grateful for so many new friends, but also for the ones who have always been there. I thank all the wonderful people from my hometown in Italy who have shared with me some of the best moments of my life. Amongst them, a special thank you goes to Mariangela Farro, the sister I chose for myself since that very first morning we met in the corridors of our middle school.

I give my warmest thanks to my family, who has always believed in me and loved me unconditionally. To my mother, Maria, who has taught me the value of being good to others, especially when it is most difficult to do so; to my father, Donato, whose determination has always inspired my own; and to my brother, Tiziano, who is the only one that will always, truly understand where I come from. I also want extend my gratitude to my acquired family, Bonnie, Mark, and Kaitlyn Schwab. I could not have been luckier to become part of such a good-hearted family.

Last, but surely not least, I thank the most important person in my life, my husband Matt. He has shared with me every step of my Ph.D., from the very first thought I had about applying to Caltech, when I was not sure I should even try, to the day I

defended and kept looking at him in the crowd to find my strength. He has celebrated my accomplishments, comforted me when things did not go as well, made me laugh when I was stressed, waited for me to come home late at night, worried when I was down and never showed any sign, and he has always supported and encouraged me. He is my stronghold, my partner in crime, and the reason why I keep challenging myself to be a better version of me.

ABSTRACT

Shell structures with cutouts are widely used in architectural and engineering applications. For thin, lightweight, and deployable space structures, cutouts are cleverly positioned to fold and store the structure in a small volume. To maintain shape accuracy, these structures must fold without becoming damaged and must be stiff in their deployed configurations. Intuitive designs often fail to satisfy these two requirements. This research proposes solutions to the topology optimization of composite, thin shell structures with cutouts.

A novel optimization algorithm was developed that makes no assumptions on the initial number, shape, and location of cutouts on deployable thin shells. The algorithm uses a density-based approach, which distributes the material within the structure by assigning a density parameter to discretized locations. This parametrization of the design domain allows for the finding of new features and the connectivity of the domain, thus providing a completely general formulation to the optimization problem. The goal is to study the effects of volume and stress constraints imposed in a deformed configuration of thin shell structures. While classical topology optimization studies focus on finding solutions to linear problems, this method is applicable to geometrically nonlinear problems and implements stress constraints in the deformed, and hence most stressed, configuration of these shells. A mathematical formulation of the optimization problem and interpolation schemes for stiffness tensor, volume, and stress are presented. A sensitivity analysis of objective function, volume, and stress constraints is provided. Finally, solutions for a thin plate and a tape spring are proposed.

Density-based methods are computationally expensive when applied to large structures and complex shapes because of the large number of design variables. To address these challenges, two optimization methods that provide more specific solutions to the problem of composite, deployable shells are proposed. The first method uses level sets to parametrize the cutouts, thereby restricting the design space and simultaneously limiting the number of design variables. This greatly reduces the computational cost. Using this approach, successful solutions are found for stiff, composite, thin shells with complex shapes that can fold without becoming damaged. The second method uses a spline representation of the contour of a single cutout on the shell, thus performing fine tuning of the shape of the cutout. Modeling techniques that simulate localized strain and experimental methods for studying the

quasi-static folding of these composite shells are developed. A laminate failure criterion suitable for thin, plain-weave composites is used in simulations to predict the onset of failure in folded shells. Numerical results are validated with folding experiments that demonstrated good agreement with numerical solutions.

Lastly, it was discovered that many of the best performing solutions have multiple closely spaced cutouts, as opposed to current designs for deployable space structures that have fewer large cutouts. This leads to the formation of small strips of material between cutouts. Hence, the behavior of thin, plain-weave composite material was characterized and the first study on size-scaling effects at small length scales ($\leq$ 15 mm) in this type of material was performed. Size-scaling effects on stiffness and strength shown in this study were introduced in numerical simulations of deployable thin shells. The study demonstrates that the prediction of the onset of failure in folded shells strongly depends on these size effects. Numerical predictions are corroborated by an experimental investigation of localized damage in thin strips of material forming between cutouts. Deployable shells resulting from the optimization studies are built and tested and localized damage is measured via digital volume correlation techniques.

PUBLISHED CONTENT AND CONTRIBUTIONS

Ferraro, S. and S. Pellegrino (2019). "Topology Optimization of Composite Self-Deployable Thin Shells with Cutouts". In: *AIAA Scitech 2019 Forum*. DOI: 10.2514/6.2019-1524.
S. Ferraro contributed finite element model, optimization studies, manufacturing of laboratory prototypes, and experiments.

– (2018). "Self-Deployable Joints for Ultra-Light Space Structures". In: *2018 AIAA Spacecraft Structures Conference*. DOI: 10.2514/6.2018-0694.
S. Ferraro contributed design concept of self-deployable joint, finite element model, manufacturing of laboratory prototypes, and experiments.

TABLE OF CONTENTS

LIST OF ILLUSTRATIONS

Number *Page*

LIST OF TABLES

Chapter 1

INTRODUCTION

1.1 Motivation and Background

Shell structures are widely used in different architectural and engineering applications. They are lightweight and can serve multiple purposes, as shown in Fig. 1.1. NASA's Orbit Pavilion, Fig. 1.1a, is an example of shells used in architectural installations. Shells are also used in robotic applications, for instance as soft actuators in robots that can crawl (Rafsanjani, Zhang, et al., 2018), like the ones shown in Fig. 1.1b. Thin shells are broadly used in deployable space structures. An example of doubly curved thin shells developed for a deployable reflector antenna is found in Fig. 1.1c, which shows the Mobile Satellite (MSAT-2) spacecraft. Another example of a partially folded, doubly curved shell is shown in Fig. 1.1d. This shell can be folded, without affecting its geometric integrity, because surface discontinuities, namely cutouts, are introduced.

A classical example of shells with cutouts, needed not to fold the structure but to provide windows in an aircraft fuselage, is shown in Fig. 1.1e. The de Havilland Comet, first commercial airliner to use jet engines, embodies some of the challenging aspects of placing cutouts in shells. Its thin exterior skin was subject to metal fatigue, due to the pressurisation-depressurisation cycle during landing and take-off. This led to development of cracks from the corner of one of the square cabin windows and a consequent catastrophic depressurisation of the cabin during commercial service. Finally, Fig. 1.1f shows the radar antenna used on the Mars Express mission, launched by the European Space Agency (ESA) in 2003. This is another example of thin shells used for deployable space structures and how cutouts can be cleverly placed on a cylindrical shell, namely a boom, to fold it and store it in a smaller volume. Shells made of high modulus materials, like the Mars Advanced Radar for Subsurface and Ionospheric Sounding (MARSIS) antenna, are difficult to fold, due to strain localization near the hinge area, and also to deploy (Mobrem and Adams, 2009a; Mobrem and Adams, 2009b).

All the examples shown have cutouts to fulfill different purposes. While in many applications one cannot avoid placing cutouts in shells, the number, position, and shape of such cutouts is often a designer's choice. This choice can be made intu-

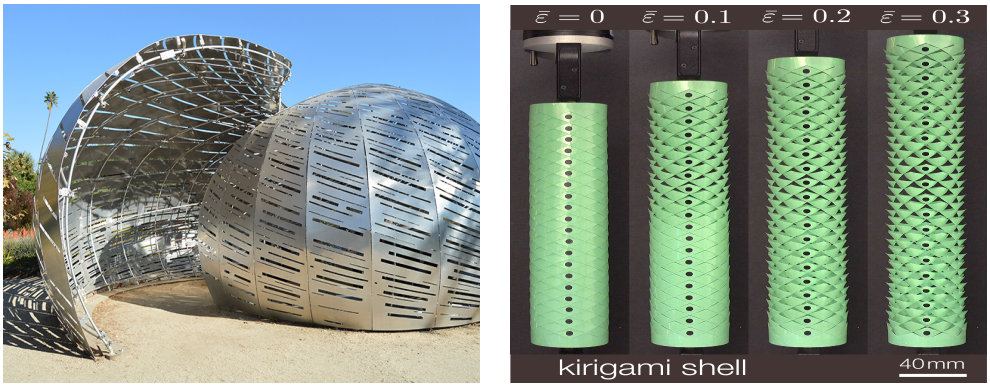

(a)

(b)

(c)

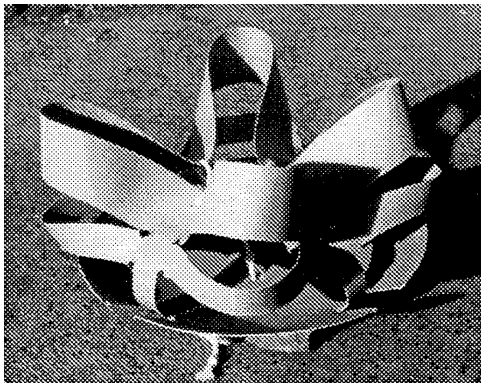

(d)

(e)

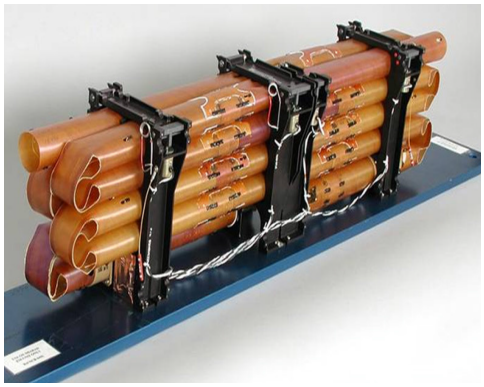

(f)

Figure 1.1: (a) NASA's Orbit Pavilion, an outdoor installation that produces sounds representing the movement of the International Space Station and 19 Earth Science satellites. Image courtesy of NASA Jet Propulsion Laboratory, (b) kirigami cylindrical shells, with triangular cuts, used as crawlers (Rafsanjani, Jin, et al., 2019), (c) MSAT-2 spacecraft during ground testing with two spring-back reflectors, one deployed and one folded. Image courtesy of Canadian Space Agency, (d) foldable dish concept with surface discontinuities (Greschik, 1996), (e) de Havilland Comet, world's first commercial jet airliner (Withey, 1997), (f) MARSIS radar antenna consisting of flattenable and foldable tubes (Mobrem and Adams, 2009a).

itively, based on knowledge of the structure and its purpose (Footdale, Banik, and T. Murphey, 2010), or it can be guided by optimization techniques. For instance, Tan and Pellegrino (2006) and Mallikarachchi and Pellegrino (2010) provide examples of shape optimization of composite thin shells with geometrical nonlinearities. The objective of these optimization studies is to maximize the bending stiffness of the deployed structure. Shape optimization is limited to modifying a few features of the structure, which usually describe its geometric boundaries. A more general technique to place cutouts in shells is topology optimization, which changes the topology of the structure entirely. Studies performed by Maute and Ramm (1997) use this approach to optimize shells with static loading and boundary conditions, while Geiss et al. (2019) optimize shells undergoing large deformations.

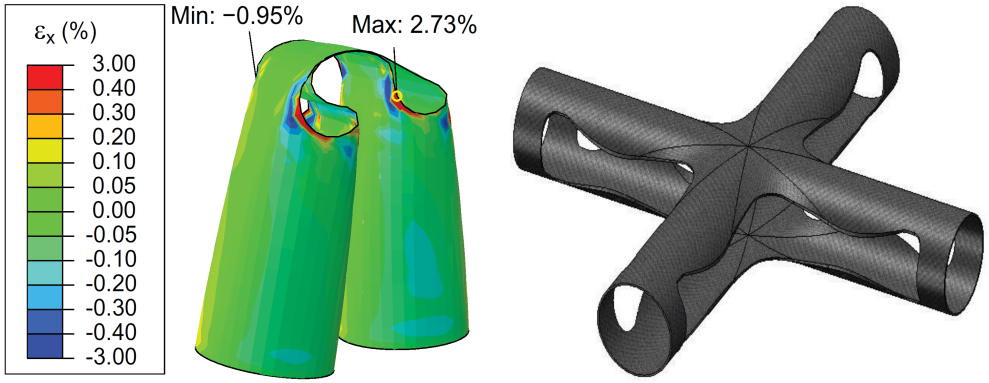

Figure 1.2: (a) strain concentration in fully folded boom with hinges (Mallikarachchi and Pellegrino, 2010), (b) compliant hinge concept (Footdale, Banik, and T. Murphey, 2010).

A challenging problem for topology optimization techniques (Bendsøe and Sigmund, 2013) is optimizing structures that:

1. consist of very thin shells, for instance shells that are hundreds of microns thick and centimeters or meters long;
2. are made of anisotropic material, like composite laminates often used in space applications;
3. undergo large displacements, because one must account for geometrical nonlinearities;
4. form regions of localized strain when deformed, because a stress constraint must be applied to the deformed configuration of the structure.

Examples of this type of structures are shown in Fig. 1.2. A tape-spring hinge, made by cutting small slots in a thin-walled tube (Mallikarachchi and Pellegrino, 2011), is shown in Fig. 1.2a. Tape-spring hinges are traditionally built in straight tubes. However, this concept can be extended to build different types of hinges. For instance, Fig. 1.2b shows a double hinge made entirely of fiber-reinforced polymers, which can reliably self-deploy using the potential energy of its stowed configuration (Footdale, Banik, and T. Murphey, 2010). The main advantage of this approach is the implementation of a lightweight technology that can provide low-cost building blocks for large space structures.

Another challenge in optimizing composite, foldable structures is to prevent localization of strain near the cutouts, as shown in Fig. 1.2a, which can lead to failure. To do so, one must employ suitable techniques for predicting failure and measuring localized damage within the structure. Failure criteria for anisotropic (Tsai and Wu, 1971) and fiber reinforced (Hashin and Rotem, 1973) materials should be able to provide an estimate for the onset of failure at a point of the foldable structure, but Mallikarachchi and Pellegrino (2013) showed that when applied to the prediction of failure of thin, plain-weave laminates, poor correlation between predictions and experiments was found. While numerically predicting failure of such structures is a challenge in itself, measuring localized damage via experiments is also difficult and size effects must be considered (Bažant and J. L. Le, 2017).

1.2 Research Objective and Outline

The overall objective of the research presented in this thesis is to optimize the topology of deployable thin shells with cutouts, so that they can be folded without damage, while also maximizing the deployed stiffness. This study proposes the first approach to the topology optimization of shells made of composite material, modeled with geometrically nonlinear finite element analysis, and imposing stress constraints in the deformed configuration.

To fulfill this research objective, three optimization methods are presented, starting from the most general approach, applicable to thin shells in bending, and incrementally building up to more specific solutions to the problem of composite, deployable shells. The first method uses a density-based approach and makes no assumptions on initial shape or location of cutouts, but it is limited by the large number of design variables, which makes it computationally expensive when considering larger structures or complex shapes. The second method uses level-set functions to place

cutouts on the shells and makes assumptions on the type of functions to be used, thus restricting the design space. This method greatly reduces the number of design variables and it is applied to composite thin shells with complex shape. Finally, the third method uses a spline representation of the contour of a single cutout on the shell, thus performing fine tuning of the shape of the cutout.

Chapter 2 presents the first optimization method and describes a new algorithm, based on a density distribution approach, that is capable of assigning volume and stress constraints in the deformed (hence most highly stressed) configuration of thin shells in bending. Solutions to the topology optimization problem of a thin, bending plate and tape spring are presented and three challenging aspects are considered: first, geometrical nonlinearities, second, a global stress constraint, and third, decoupling of topology optimization and the corresponding computational mechanics method, such as a finite element method.

Chapter 3 develops modeling and experimental techniques for studying the quasi-static folding of composite shells with complex shape. A particular challenge associated with these techniques is the simulation of localized strains. A laminate failure criterion is used to predict the onset of failure in folded shells. First, preliminary designs obtained using physical intuition are presented. Then, two optimization methods are detailed and solutions for thin shells forming a 90° corner and made entirely of fiber reinforced composite material are proposed.

Chapter 4 presents the first experimental study of size-scaling effects on thin plain-weave samples with width ranging between 15 and 1 millimeters. The results of this work are combined with the previous optimization studies by introducing size-scaling effects in the numerical analysis of deployable shells forming a corner and analyzing how size affects the onset of damage in thin shells made of plain-weave composite material. Additionally, experiments are performed to measure localized damage near the cutouts using a digital volume correlation technique.

Chapter 5 concludes the thesis and discusses future research directions.

Chapter 2

DENSITY-BASED APPROACH TO TOPOLOGY OPTIMIZATION OF BENDING DOMINATED SHELLS WITH GEOMETRICAL NONLINEARITIES

2.1 Introduction

The problem of optimal placement of cutouts in thin shell structures to perform designated tasks, such as reproducing certain sounds (Delgado and Goods, 2015) or folding and deploying (Mobrem and Adams, 2009b), has been the object of studies for many decades. Topology optimization provides a general solution to this problem. Particularly, a density-based approach allows for the redistribution of material within a design domain, thus changing the initial topology of a structure and finding new features, such as cutouts. The main advantage is that no assumptions on the initial shape or the location of the cutouts are necessary.

Open source topology optimization algorithms have been written (Andreassen, Clausen, et al., 2011) and broadly used for different applications. While many studies have demonstrated the large applicability of this method, few examples of solutions are provided for thin shells undergoing large displacements. This chapter introduces a density-based method for topology optimization, its mathematical formulation, and implementation. The goal is to study the effects of volume and stress constraints imposed in a chosen deformed configuration of a thin shell structure and to develop an algorithm that can apply these constraints.

2.2 Background and Layout of the Chapter

Structural optimization methods can be grouped in two very general categories: traditional shape optimization and topology optimization. In the first case, the geometry of a structure is defined by contours or surfaces that enclose an area or volume continuously filled with material. Hence, only the boundaries of the design domain have to be parametrized by shape functions to solve the optimization problem. This leads to a reasonably small number of design variables used to optimize the structure, which are the control nodes of the shape functions. However, the optimization process cannot generate new boundaries. Only contours or surfaces that are present in the initial layout can be varied and the topology of the structure remains unchanged. Size optimization can be regarded as a subset of shape opti-

mization problems. Here, a single or a few design variables are chosen to describe the size of the structure or one of its members (e.g. the diameter of a rod in a pin-jointed structure).

In the second case, there is an additional distinction to make between density-based methods, first formalized by Bendsøe and Kikuchi (1988), and level-set methods, introduced by S. Osher and Sethian (1988). A comprehensive review of topology optimization approaches was done by Sigmund and Maute (2013). In a density-based method, the material within the structure is distributed by assigning a density parameter to discretized locations. The density parameter can vary continuously between its limit values, 0 an 1. A density of 0 is a numerical description for a void. This parametrization of the design domain allows to find new features, such as the number, location, and shape of holes and the connectivity of the domain (Bendsøe and Sigmund, 2013). The objective is to reach the optimal layout of a structure, where the only known quantities are the initial domain, boundary conditions, and applied loads.

Similarly, a level-set method allows to change the topology of a structure by providing a way to describe the position and track the movement of its geometric boundaries (Sethian and Wiegmann, 2000; S. J. Osher and Santosa, 2001; M. Y. Wang, X. Wang, and Guo, 2003; Allaire, Jouve, and Toader, 2004). A scalar level-set function is constructed as follows. If a point within the design domain generates negative values of the level-set function, the point belongs to a new domain defined as void. If it generates positive values, the point belongs to a different domain defined as solid. Finally, null values of the level-set function describe the boundaries of the structure. In two dimensions, the level-set method corresponds to representing a closed curve Γ using an auxiliary function ϕ, called the level-set function. The curve Γ is described as the null values of ϕ using the equation $\Gamma = \{(x, y) \mid \phi(x, y) = 0\}$. The level-set method manipulates Γ implicitly (i.e. without an explicit parametrization of the contour of the curve), through the function ϕ.

A set of solutions obtained performing topology optimization, via density-based method, on thin shells in bending are presented here. Shell structures are some of the most broadly used in engineering applications and they are very interesting for lightweight deployable space structures applications (Pellegrino, 2015). Nevertheless, topology optimization of shell structures, especially considering large displacements and bending behaviour, is not a very explored field. Some early examples of shell structures optimized via an adaptive scheme, including both ma-

terial topology and shape optimization, are provided by Maute and Ramm (1997). More recent developments in investigating topology optimization methods for shells are provided by the following: Bendsoe et al. (2005), who discuss broader applications for density-based methods, including optimization of laminated composite shell structures; Lund (2009) and Townsend and H. A. Kim (2019), who investigate buckling problems; Geiss et al. (2019), who optimize and build shells undergoing large deformations.

One important aspect of topology optimization is to find an analytical formulation of the sensitivities of the objective function and the constraints. This is necessary for implementing gradient-based algorithms that achieve faster convergence to an optimal solution. An overview of design sensitivity analysis is provided by Tortorelli and Michaleris (1994). Geometrical nonlinearities (hence large displacements) were considered in the topology design of compliant mechanisms by different authors, such as Buhl, Pedersen, and Sigmund (2000), Gea and Luo (2001), Bruns and Tortorelli (2001), Pedersen, Buhl, and Sigmund (2001), and Saxena and Ananthasuresh (2001). Particularly interesting for the type of structures studied here, such as plates in bending, is the work performed by Pajot and Maute (2006), which makes use of a co-rotational finite element method that satisfies equilibrium equations in a reference system that is local to each element.

Another important aspect is the implementation of stress constraints. One approach is to assign stress constraints locally, on each element or group of elements of a finite element discretization of the structure, thus generating a large number of constraints. Local stress constraints are particularly useful to capture stress concentration in the structure and limit a local stress measure to allowable values (Duysinx and Bendsøe, 1998; Pereira, Fancello, and Barcellos, 2004; Bruggi and Venini, 2008; Paris et al., 2009). Nevertheless, a large number of constraints can be computationally expensive. Therefore, a global stress measure is a common way to impose stress constraint (Duysinx and Sigmund, 1998; Guilherme and Fonseca, 2007; De Leon et al., 2015). C. Le et al. (2010) provide a list of algorithms and stress constraints used to optimize 2D, L-bracket designs.

This chapter presents studies of the effects of volume and stress constraints in topology optimization of thin shells. Both small and large displacements are considered. An algorithm capable of performing topology optimization of thin shells undergoing large displacements, and subject to volume and stress constraints in deformed configuration, is shown. A significant advantage of the computational framework

provided here is decoupling of the optimization solver, that provides a new topology at each step, from the finite element software that performs a structural analysis of any given topology. This allows to outsource the finite element analysis to commercial software. A similar concept was developed by Chung et al. (2019) who use OpenMDAO, an open-source computational framework for multidisciplinary design optimization.

First, a mathematical formulation of the optimization problem and interpolation schemes for stiffness tensor, volume, and stress are presented. The problem studied is to maximize the stiffness of shells in the initial configuration (deployed) while constraining volume and stress in either initial or deformed configuration. A sensitivity analysis of the objective function, volume, and stress constraints is provided. The new algorithm developed here is described in detail. First it is tested on a classical benchmark problem, the Messerschmidt-Bölkow-Blohm (MBB) Beam problem, and the result is compared to the one obtained by Andreassen, Clausen, et al. (2011). Then a study of thin plates in bending is performed and solutions to linear problems are examined against solutions obtained with the commercial tool Abaqus Topology Optimization Module (ATOM) 2017-HF5. Finally, geometrically nonlinear problems are studied and solutions for a thin plate and a tape spring are presented.

2.3 Optimization Problem and Interpolation Schemes

In a density-based approach the design domain is discretized by N finite elements and the relative density ρ_e of material in each element is a design variable. An N-vector containing the design variables is denoted $\boldsymbol{\rho}$. Two sets of variables are to be considered: design variables, $\boldsymbol{\rho}$, and state variables, $\mathbf{u}$. These are coupled by a state equation that for given fixed values of the design variables returns values of the state variables. An optimization formulation solving the problem of distributing a limited amount of material in the design domain, such that the objective function f is minimized and stress constraints are satisfied, can be written as:

$$\begin{aligned} \min_{\boldsymbol{\rho},\mathbf{u}} \quad & : f(\boldsymbol{\rho},\mathbf{u}) \\ \text{subject to} \; & : V(\boldsymbol{\rho}) \leq V^* \\ & : \boldsymbol{\sigma}(\boldsymbol{\rho},\mathbf{u}) \leq \boldsymbol{\sigma}^* \\ & : \mathbf{0} \leq \boldsymbol{\rho} \leq \mathbf{1} \\ & : \mathbf{R} = \mathbf{0} \end{aligned} \tag{2.1}$$

where $V(\boldsymbol{\rho})$ is the volume of the structure as function of design variables, V^* is the upper bound on material volume, $\boldsymbol{\sigma}(\boldsymbol{\rho}, \mathbf{u})$ is the stress field in the structure as function of both design and state variables, $\boldsymbol{\sigma}^*$ is a vector of stress constraints, and $\mathbf{R}$ is the residual in obtaining the structural equilibrium in a nonlinear finite element formulation.

A classical topology optimization problem is the minimization of compliance (Bendsøe and Sigmund, 2013), which will also be the focus of this chapter. This implies finding the optimal density distribution to obtain the stiffest possible structure, given certain applied loads or displacements and constraints. Hence, the objective function in Eq. 2.1 can be written as:

$$f(\boldsymbol{\rho}, \mathbf{u}) = \mathbf{F}^T \mathbf{u} \tag{2.2}$$

where $\mathbf{F}$ and $\mathbf{u}$ are the load and displacement vectors, respectively.

Both objective function and constrains must be written as functions of the design variables. Since the optimization problem written in Eq. 2.1 is continuous, i.e. $\rho_e \in [0, 1]$, the interpolation schemes must be defined so that stiffness, volume, and stress can be interpolated between their possible minimum and maximum values. A broad summary of interpolation schemes chosen by different authors is provided by C. Le et al. (2010). Since the compliance can be written as a function of the stiffness tensor (Andreassen, Clausen, et al., 2011), using the state equation, an interpolation scheme for the stiffness would automatically allow to write the compliance as a function of the design variables. The scheme chosen here follows the modified Solid Isotropic Material with Penalization (SIMP) approach (Sigmund, 2007):

$$C^e_{ijkl}(\rho_e) = C^{min}_{ijkl} + {\rho_e}^p (C^0_{ijkl} - C^{min}_{ijkl}) \qquad \rho_e \in [0, 1] \tag{2.3}$$

where $C^e_{ijkl}(\rho_e)$ is the stiffness tensor for element e, C^{min}_{ijkl} is a very small stiffness value assigned to void regions in order to prevent the stiffness matrix from becoming singular, C^0_{ijkl} is the stiffness tensor for solid isotropic material (where $\boldsymbol{\rho} = \mathbf{1}$), and p is a penalization factor (which was set equal to 3 in the results shown in this chapter). Interpolation schemes for volume and stress are chosen as follows:

$$V(\boldsymbol{\rho}) = \sum_{e=1}^{N_{el}} \rho_e v_e \qquad \rho_e \in [0, 1] \tag{2.4}$$

$$\sigma_{ij}(\boldsymbol{\rho}, \mathbf{u}) = \rho_e^q \, \sigma_{ij}^0 \qquad \rho_e \in [0, 1] \tag{2.5}$$

where N_{el} is the total number of elements that discretize the structure, v_e is the volume of each element, σ_{ij}^0 is the stress vector for solid isotropic material (where $\boldsymbol{\rho} = \mathbf{1}$), and q is a penalization factor.

2.4 Technique to Maximize the Stiffness of a Structure with Volume and Nonlinear Stress Constraints

A problem of interest when optimizing foldable (and self-deployable) structures is to maximize the stiffness in the deployed configuration while preventing the structure from being damaged when it is folded. The same type of problem will be studied in chapter 3, which investigates the shape and topology optimization using a level-set method of self-deployable, composite joints. Hence, the set of solutions presented here will focus on either minimizing (force driven case) or maximizing (displacement driven case) the strain energy of the structure, calculated in the initial configuration, while setting some constraints to either reduce the volume of the structure or prevent it from being damaged by constraining the stress to a maximum allowable value. Minimizing or maximizing the strain energy of a structure, depending on whether the problem if force or displacement driven, leads to maximizing its stiffness. A schematic description of the problem is presented in Fig. 2.1.

Let us assume that the structure is subject to an imposed rotation, θ. The blue curve shows an incremental scheme to reach through a geometrically nonlinear solution a folded configuration that satisfies the equilibrium condition between internal and external loads. Since the goal is to maximize the stiffness of the structure in the initial configuration (deployed), there is no reason to use a nonlinear formulation to calculate the strain energy. A linear perturbation around the initial configuration is used instead. The state equation for the linear finite element analysis is:

$$\mathbf{K}\,\mathbf{u} = \mathbf{F} \tag{2.6}$$

where $\mathbf{K}$ is the stiffness matrix of the structure and $\mathbf{F}$ and $\mathbf{u}$ are the load and displacement vectors, respectively. Using this equation, the objective function assumes the classical form of compliance (Andreassen, Clausen, et al., 2011), which, except for a constant coefficient (1/2), is the strain energy of the structure . Equation 2.2 can be rewritten as follows:

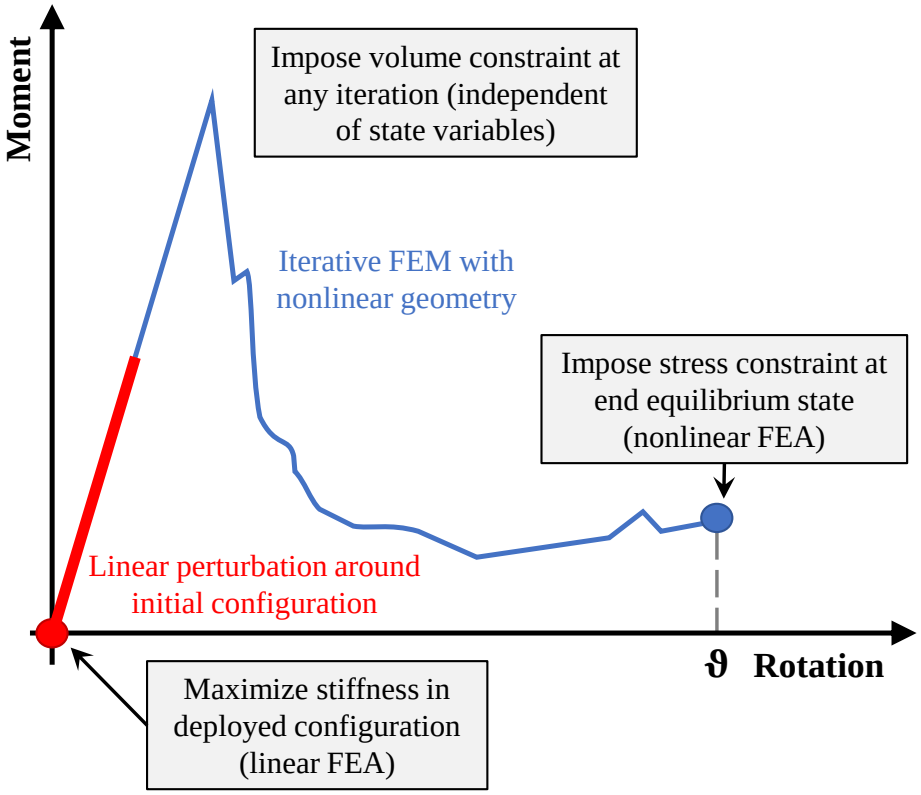

Figure 2.1: Description of the type of problems solved in this chapter. The blue curve is a representative plot of internal loads, G, and displacements, u, for nonlinear problems. If an external load F is applied, the corresponding equilibrium displacement u is found using an iterative solver. A linear perturbation around the initial condition, red curve, allows to calculate the initial stiffness of the structure, while a stress constraint is imposed at the end equilibrium state of a nonlinear formulation. A volume constraint can be applied at any iteration, since it is independent of the state variables.

$$f(\boldsymbol{\rho}, \mathbf{u}) = \mathbf{F}^T \mathbf{u} = \mathbf{u}^\mathbf{T}\mathbf{K}\mathbf{u} = \sum_{e=1}^{N_{el}} C^e_{ijkl}(\rho_e)\, \mathbf{u}^\mathbf{T}_\mathbf{e}\mathbf{k_0}\mathbf{u_e} \tag{2.7}$$

where $\mathbf{u_e}$ is the element displacement vector and $\mathbf{k_0}$ is the element stiffness matrix for an element with unit stiffness tensor. Recall that the stiffness matrix $\mathbf{K}$ is symmetric, hence $\mathbf{K^T} = \mathbf{K}$.

A volume constraint is independent of the state variables and can be imposed at any point during the finite element analysis. In this case, the nonlinear formulation is only needed to impose a stress constraint in the folded configuration of the structure. In fact, the stress distribution in the structure depends on the state variables and its

values change at different iterations of the nonlinear finite element analysis.

In finite element-based, stress-constrained topology optimization problems one would ideally enforce one or more stress constraints in each finite element or a scalar stress-related constraint in each element, such as the highest expected component of the stress in that element or a single stress value derived from a failure criterion (e.g. von Mises stress). Using this approach, one would have to apply as many constraints to the optimization problem as the number of elements, which would be computationally expensive. Although efficient formulations for imposing local stress constraints have been implemented (Silva, Beck, and Sigmund, 2019a; Silva, Beck, and Sigmund, 2019b), a common way to deal with stress constraints is to select one global stress measure (C. Le et al., 2010; De Leon et al., 2015). An intuitive choice would be to use the maximum value of the stress in the design domain. Nevertheless, this choice would preclude the use of a gradient-based algorithm, since the maximum function is not differentiable.

In this work, the global P-norm stress measure (Duysinx and Sigmund, 1998) is applied in order to approximate the maximum stress in the design domain. This formulation aims to control the stress level by capturing the global trend of the maximum stress. However, for problems with very localized high stresses one cannot assure that the stress is below the critical value in all areas. This stress constraint can be written as:

$$\sigma_{PN}(\boldsymbol{\rho}, \mathbf{u}) = \left(\sum_{e=1}^{N_{el}} (\sigma_{VM,e})^P \right)^{1/P} \leq \sigma^* \tag{2.8}$$

$$\sigma_{VM,e}(\boldsymbol{\rho}, \mathbf{u}) = \rho_e^q \, \sigma_{VM,e}^0 \tag{2.9}$$

where $\sigma_{VM,e}$ is the element von Mises stress measure, which can be written as a function of the element von Mises stress measure for solid isotropic material $\sigma_{VM,e}^0$ (where $\boldsymbol{\rho} = \mathbf{1}$), using the interpolation scheme in Eq. 2.5, and P is the stress norm parameter. It can be proven that for $P \to \infty$, the P-norm approaches the maximum stress. However, for high values of P the degree of nonlinearity and discontinuity of the problem increases, thus increasing the chances of finding a poor local minima. For the results shown in this chapter the value $P = 6$ was adopted.

2.4.1 Sensitivity Analysis of Objective Function and Constraints

The optimization problem defined in Eq. 2.1 has a very large design space, with the number of design variables equal to the number of elements in the structure. While a global stress measure can be adopted to solve the issue of having many constraints, as described before, the size of the design space remains a computational challenge. A gradient-based optimization algorithm is desirable in this case, hence an analytical formulation of derivatives of objective function and constraints must be found.

2.4.1.1 Adjoint Method to Calculate Derivatives of Objective Function

In adjoint methods the derivatives of the displacement are not calculated explicitly. Hence the sensitivity analysis is simplified (Bendsøe and Sigmund, 2013). For the problem at hand one can rewrite the objective function by adding a zero term:

$$f(\boldsymbol{\rho}, \mathbf{u}) = \mathbf{F}^T \mathbf{u} - \boldsymbol{\lambda}^T (\mathbf{K}\mathbf{u} - \mathbf{F}) \tag{2.10}$$

where $\boldsymbol{\lambda}$ is a vector of Lagrangian multipliers. Assuming the external loads to be independent from the displacement field, the derivative of the objective function becomes:

$$f'_e(\boldsymbol{\rho}, \mathbf{u}) = \frac{\partial f(\boldsymbol{\rho}, \mathbf{u})}{\partial \rho_e} = \frac{\partial f(\boldsymbol{\rho}, \mathbf{u})}{\partial \mathbf{u}} \frac{\partial \mathbf{u}}{\partial \rho_e} = \left(\mathbf{F}^\mathbf{T} - \boldsymbol{\lambda}^T \mathbf{K}\right) \frac{\partial \mathbf{u}}{\partial \rho_e} - \boldsymbol{\lambda}^T \frac{\partial \mathbf{K}}{\partial \rho_e} \mathbf{u} \tag{2.11}$$

Because $\mathbf{K}\mathbf{u} - \mathbf{F} = \mathbf{0}$, from Eq. 2.6, the Lagrangian multiplier vector $\boldsymbol{\lambda}$ can be chosen freely. To eliminate the unknown $\frac{\partial \mathbf{u}}{\partial \rho_e}$ from Eq. 2.11, $\boldsymbol{\lambda}$ is chosen such that:

$$\left(\mathbf{F}^\mathbf{T} - \boldsymbol{\lambda}^T \mathbf{K}\right) = 0 \tag{2.12}$$

This equation is in the form of an equilibrium equation and for the chosen objective function one obtains directly that $\boldsymbol{\lambda} = \mathbf{u}$, without any additional computations. Hence, the derivative of the objective function becomes:

$$f'_e(\boldsymbol{\rho}, \mathbf{u}) = -\boldsymbol{\lambda}^T \frac{\partial \mathbf{K}}{\partial \rho_e} \mathbf{u} = -\mathbf{u}^\mathbf{T} \frac{\partial \mathbf{K}}{\partial \rho_e} \mathbf{u} \tag{2.13}$$

Finally, given the form of the stiffness matrix $\mathbf{K}$, from Eq. 2.3 and 2.7, this derivative is of the particularly simple form:

$$f'_e(\boldsymbol{\rho}, \mathbf{u}) = -p{\rho_e}^{p-1} \left(C^0_{ijkl} - C^{min}_{ijkl} \right) \mathbf{u_e^T k_0 u} \tag{2.14}$$

2.4.1.2 Derivatives of Constraints

Given the form of the volume of the structure, Eq. 2.4, the derivative can be written as:

$$V'_e(\boldsymbol{\rho}) = \frac{\partial V(\boldsymbol{\rho})}{\partial \rho_e} = v_e \tag{2.15}$$

The P-norm of the stress, Eq. 2.8, has a much more complex derivative. An example of the sensitivity analysis of the von Mises equivalent stress for a linear finite element formulation is given by Silva, Beck, and Sigmund (2019a). To simplify the derivative and avoid the adjoint problem, this work assumes that ${\sigma_{VM,e}}^0$ is constant and therefore:

$$\frac{\partial \sigma_{VM,e}(\boldsymbol{\rho}, \mathbf{u})}{\partial \rho_e} = \frac{\partial \left({\rho_e}^q \right)}{\partial \rho_e} \sigma^0_{VM,e} + {\rho_e}^q \cancelto{0}{\frac{\partial \left(\sigma^0_{VM,e} \right)}{\partial \mathbf{u}}} \frac{\partial \mathbf{u}}{\partial \rho_e} \approx \frac{\partial \left({\rho_e}^q \right)}{\partial \rho_e} \sigma^0_{VM,e} \tag{2.16}$$

This assumption leads to a simpler form of the derivative of the P-norm of the stress:

$$\sigma'_{PN}(\boldsymbol{\rho}, \mathbf{u}) \approx \frac{1}{P} \left(\sum_{e=1}^{N_{el}} \left(\rho_e^q \sigma^0_{VM,e} \right)^P \right)^{\frac{1}{P}-1} \sum_{e=1}^{N_{el}} \left(Pq \left(\rho_e^q \sigma^0_{VM,e} \right)^{P-1} \rho_e^{q-1} \sigma^0_{VM,e} \right) \tag{2.17}$$

A simplified sensitivity analysis of the stress constraint allows to run the geometrically nonlinear finite element simulation only once for the initial guess, which is usually a solid isotropic structure ($\boldsymbol{\rho} = \mathbf{1}$). The advantage is to avoid well-known problems, such as nonconvergence of solutions due to large element distortions (Bruns and Tortorelli, 1998; Buhl, Pedersen, and Sigmund, 2000; Bruns and Tortorelli, 2003; Yoon and Y. Y. Kim, 2005; F. Wang et al., 2014). Additionally, this assumption does not prevent the proposed algorithm from satisfying the stress constraint when convergence is reached, according to Eq. 2.18.

2.4.2 Description of the Algorithm

A block diagram that describes the algorithm developed here is shown in Fig. 2.2. The optimization loop starts with an initial guess where all density values are set

equal to 1. Loads and boundary conditions are applied to the structure and a finite element analysis is performed. The analysis is implemented in two steps, as illustrated in Fig. 2.1. First, a geometrically nonlinear finite element analysis is performed and the von Mises stress field for fully solid structure, $\boldsymbol{\sigma}^{\mathbf{0}}_{\boldsymbol{VM}}$, is calculated in the deformed configuration. This analysis is only done once, at the first iteration, for the fully solid structure ($\boldsymbol{\rho} = \mathbf{1}$). Second a linear finite element analysis is performed to calculate the objective function, $f(\boldsymbol{\rho}, \mathbf{u})$. The algorithm makes use of commercial software, Abaqus 2017, to carry out the finite element analysis.

From equation 2.7, the objective function can be calculated as the sum of the strain energies in each element. Hence, one set of variables extracted from Abaqus is the strain energy density, called 'ESEDEN', in each finite element. The second set of variables is the von Mises stress, called 'MISESMAX', in each finite element. For a shell element 'MISESMAX' represents the maximum Mises value among all the section points in the layer. The next guess for the design variables in the optimization loop is found using a gradient-based solver, which minimizes (or maximizes) the objective function and imposes certain constraints. The solver chosen for this work is the method of moving asymptotes (MMA) written by Svanberg (1987). The convergence criterion is:

$$\max\left(|\rho_e^{i+1} - \rho_e^i|\right) \leq 0.01 \qquad e = 0, 1, 2...N_{el} \tag{2.18}$$

where i is the current iteration counter.

The architecture of the algorithm is structured in a pattern similar to the 88 lines, MATLAB code (Andreassen, Clausen, et al., 2011) developed as an extension and improvement of the well-known code presented by Sigmund (2001). In order to ensure the existence of solutions to the topology optimization problem and avoid the formation of checkerboard patterns (Diaz and Sigmund, 1995; Jog and Haber, 1996; Sigmund and Petersson, 1998), a filter is applied to the sensitivities of the compliance as follows:

$$\widehat{\frac{\partial f(\boldsymbol{\rho}, \mathbf{u})}{\partial \rho_e}} = \frac{1}{\max(\gamma, \rho_e) \sum_{i=1}^{N_i} H_{ei}} \sum_{i=1}^{N_i} H_{ei} \rho_i \frac{\partial f(\boldsymbol{\rho}, \mathbf{u})}{\partial \rho_i} \tag{2.19}$$

where N_i is the set of elements i for which the center-to-center distance $\Delta(e, i)$ to element e is smaller than the filter radius r_{min}, γ is a small positive number (e.g. 10^{-3}) that avoids division by zero, and H_{ei} is a weight factor defined as:

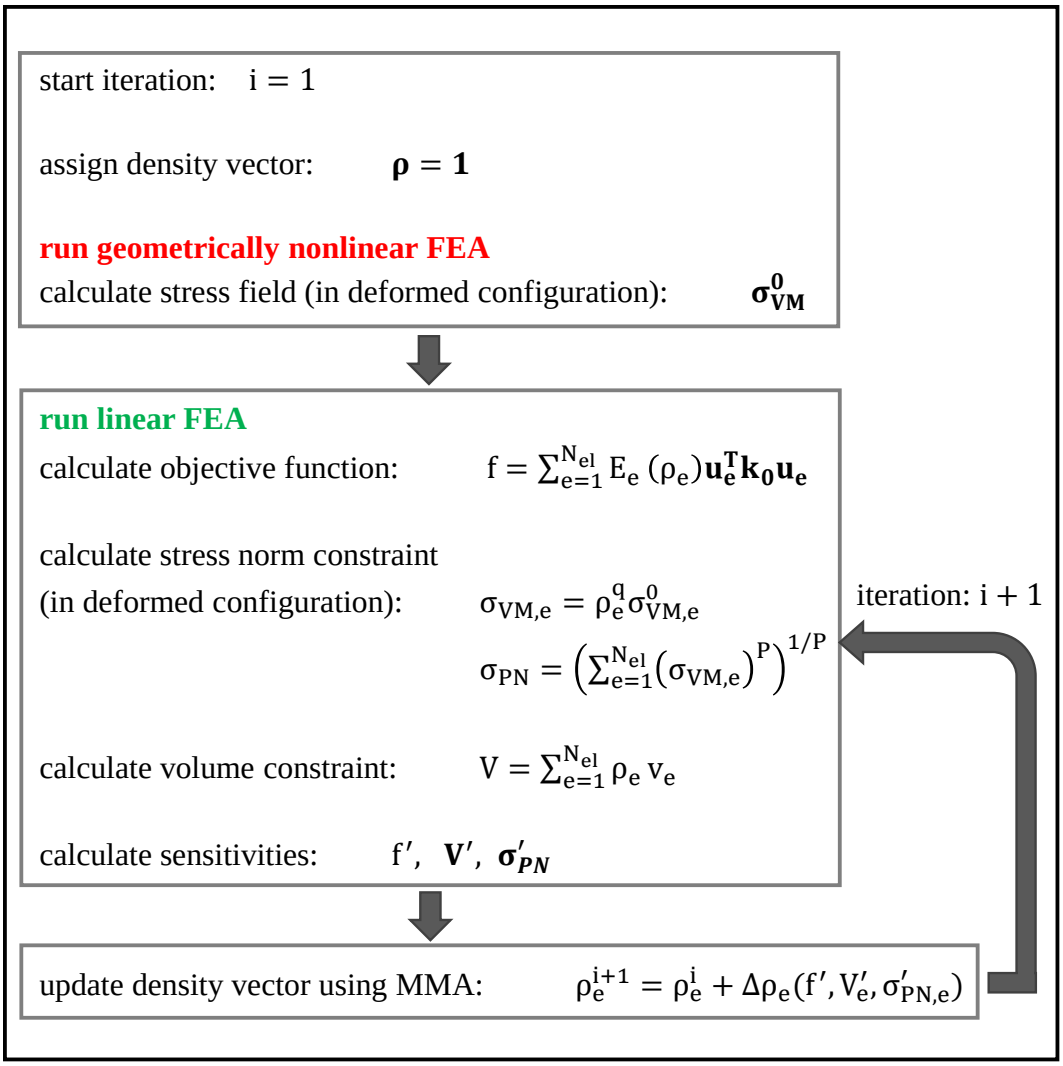

Figure 2.2: Block diagram of the algorithm developed in this study.

$$H_{ei} = \max(0, r_{min} - \Delta(e, i)) \tag{2.20}$$

One key feature of the algorithm developed here is the decoupling of the finite element formulation from the optimization step. By doing so, the finite element formulation can be outsourced to a software of choice, hence opening many possibilities for studying complex structures undergoing large displacements and/or large deformations. Figure 2.3 describes how the algorithm is implemented. A Python script interfaces with Abaqus and MATLAB software. The first part of the script assigns the geometry of the structure, boundary conditions, mesh discretization, and optimization parameters such as material and stress penalization factors, etc. A material distribution is also assigned and each element is associated with a different

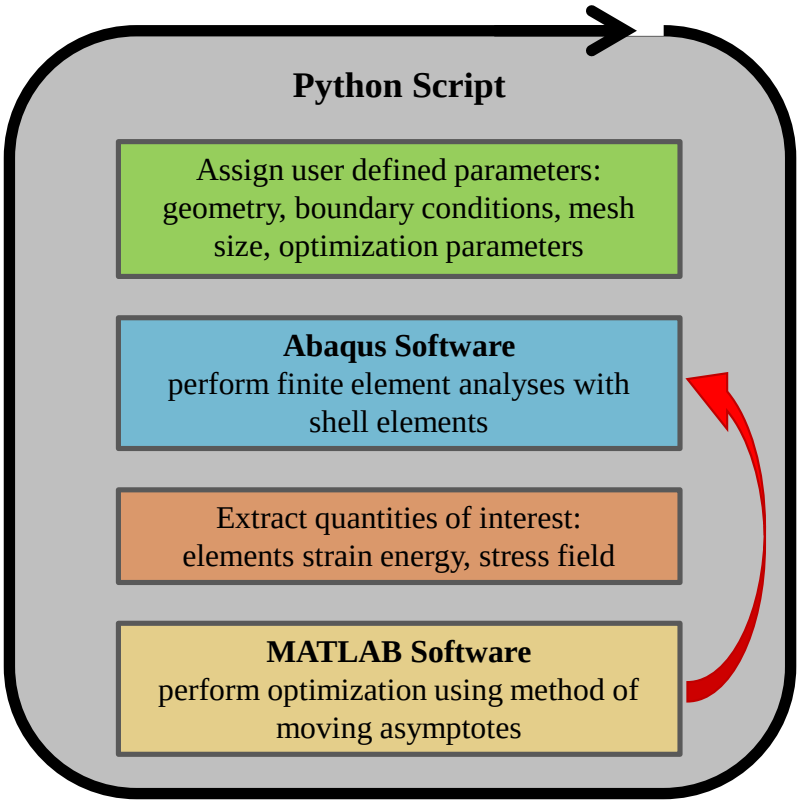

Figure 2.3: Algorithm implementation.

elastic tensor. Subsequently, a finite element analysis of the structure is performed by Abaqus and quantities of interest are extracted from the result of the analysis. Finally, a new material distribution is generated according to the results from the MMA solver through the optimization process, implemented in MATLAB.

2.5 Reference Problem: Messerschmidt-Bölkow-Blohm (MBB) Beam

A well-known benchmark problem for topology optimization algorithms is the MBB beam. A solution to this problem is provided by Andreassen, Clausen, et al. (2011) and replicated in Fig. 2.5a, using the 88 lines, MATLAB code. The design domain, shown in Fig. 2.4, is rectangular and discretized with square elements. This is a two-dimensional problem. The beam is simply supported at the bottom right corner, thus constraining the vertical displacement, and is symmetric. Symmetry is exploited using simply supported boundary conditions at the center of the full beam. Hence, only half beam is analyzed. A concentrated force pushes down the center of the full beam.

A compliance minimization problem (hence minimizing strain energy and max-

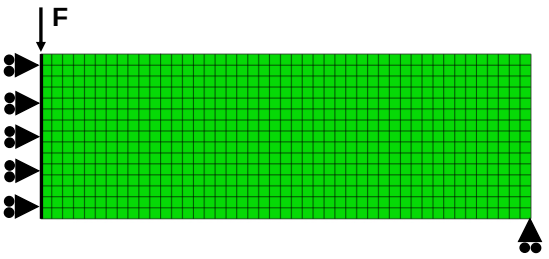

Figure 2.4: Design domain of an MBB beam with boundary conditions.

imizing stiffness) with volume constraint is solved. The finite element analysis is linear and uses CPS4 (plane-stress, 4-nodes, and bi-linear) elements in Abaqus 2017. Mesh and elements are chosen to match the finite element formulation used by Andreassen, Clausen, et al. (2011) so that results can be compared. The results shown in Fig. 2.5 were obtained for a mesh of 675 (45 × 15) elements. The side of each element is 1 mm long, hence, the full structure is 45 mm in length and 15 mm in height. The structure is isotropic and hence the material parameters are the Young's modulus and Poisson's ratio. Equation 2.3 can be rewritten as:

$$E_e(\rho_e) = E_{min} + \rho_e{}^p(E_0 - E_{min}), \qquad \rho_e \in [0, 1] \tag{2.21}$$

where E stands for Young's modulus. The Young's modulus of the fully solid material is E_0 = 1 GPa and the Poisson's ratio is ν = 0.3. The concentrated force is F = 1 N. The stiffness penalization parameter is p = 3 and the minimum radius for compliance sensitivity filtering is r_{min} = 1.4 mm. Finally, the upper bound on material volume is $V^* = 0.5\, V_0$, which corresponds to eliminating half of the material from the solid structure (where V_0 is the volume of the solid structure).

As we can see in Fig. 2.5 the two results obtained from the 88 lines, MATLAB code and the algorithm presented here are comparable. The solution obtained with the MATLAB code is presented in grey scale values of the density parameter in each element, Fig. 2.5a. This is a default output and it was not modified to distinguish its results from the ones generated by the algorithm developed in this study. Darker elements possess a higher density value. Hence, elements in black have density ρ_e = 1 and elements in white (which blend with the background) have density ρ_e = 0. This choice allows to easily visualize the optimal topology of the structure with black cross beams appearing in the design domain. Some grey elements are

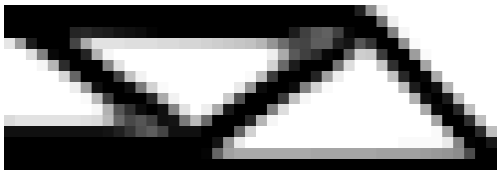

(a)

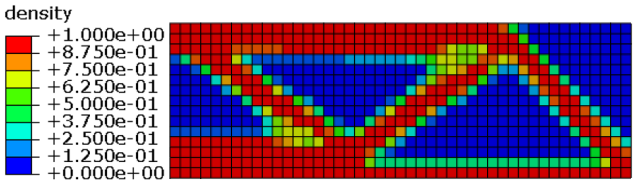

(b)

Figure 2.5: A solution to the MBB problem (a) MATLAB code (Andreassen, Clausen, et al., 2011), (b) new algorithm developed here.

still present, but they can be eliminated using different filtering schemes (Sigmund, 2007).

The solution obtained with the algorithm developed in this study is presented in Fig. 2.5b. The values of the density in each element range from 0, corresponding to a dark blue color, to 1, corresponding to a red color. Ideal results for a binary representation of the optimal topology, where each element either exists ($\rho_e = 1$) or doesn't ($\rho_e = 0$), would only show a dark blue background with a red structure appearing once the optimization has converged. Because of sensitivity of solutions to filtering schemes, some results presented in this chapter will be more binarized than others. When using the algorithm developed here, elements with intermediate density values will be represented in different colors other than blue or red. The intermediate values are reported in a legend next to each new solution. For this benchmark, MBB beam problem, the solution generated by the new algorithm matches well the reference solution, including elements with intermediate densities.

2.6 Thin Plate in Bending

A class of problems that is less explored by existing topology optimization techniques but is of great interest to find optimal topologies for deployable space structures, is that of thin, bending structures undergoing large displacements. Some examples are found in Pajot and Maute (2006), Rupp et al. (2009), and Geiss et al. (2019). Recently, a level-set method has been used to find topologies that maximize the first

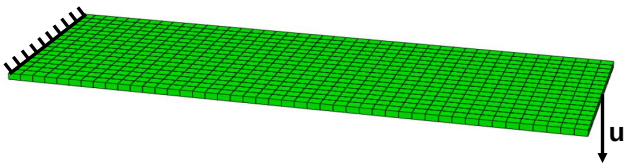

Figure 2.6: Design domain of a plate in bending with boundary conditions.

buckling mode of shell structures subject to a mass constraint (Townsend and H. A. Kim, 2019). These types of structures are discretized with shell elements in a finite element-based analysis of the problem.

One straightforward example of this class of problems is shown here. The design domain, shown in Fig. 2.6, is a thin, flat plate, which is clamped at one end. An out-of-plane nodal displacement u is imposed at the middle node of the other end of the plate. Shell elements type S4R where chosen for this study. This is a commonly used type of shell element and it did not give any convergence issues when performing implicit finite element simulations using Abaqus 2017. The elements have in-plane dimensions of 1 mm $\times$ 1 mm and thickness of 0.1 mm. A mesh of 720 (45 $\times$ 16) elements was used to obtain the following results. Hence, the full plate is 45 mm long, 16 mm wide, and 0.1 mm thick. The material is isotropic with Young's modulus E_0 = 70 GPa and Poisson's ratio is ν = 0.33. The imposed end displacement is u = 10 mm. Since the problem is displacement driven (instead of force), the objective function in Eq. 2.7, which is a sum of strain energy in each element, must be maximized instead of being minimized.

The maximum Mises stress distribution on the plate is shown in Fig. 2.7. Both linear and geometrically nonlinear finite element formulations were used to analyze the structure. Geometrical nonlinearity in this case only changes the stress distribution slightly. Hence, it is interesting to study whether this change affects the results of a stress constrained topology optimization analysis.

Three cases of topology optimization were performed. The first case aims to find a topology that maximizes the stiffness of the structure in the initial (undeformed) configuration, while applying a volume constraint. For this case, a linear finite element analysis is sufficient. The second case aims to find a topology that maximizes the stiffness of the structure in the initial (undeformed) configuration, while simultaneously applying a volume and a stress constraint in the initial configuration. Also, in this case, a linear finite element analysis can be used. Finally, the third

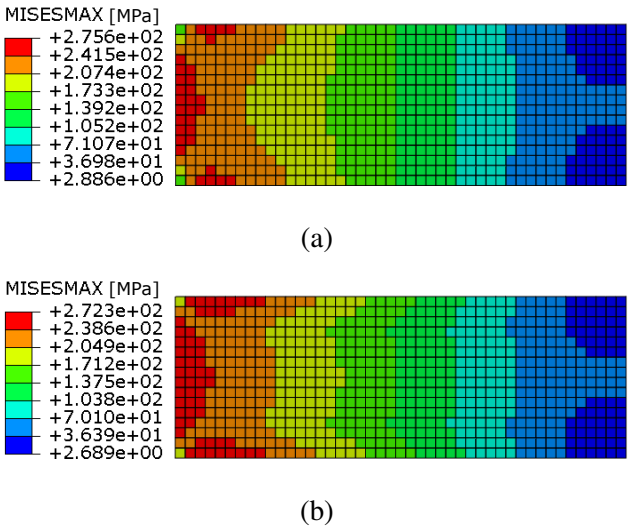

Figure 2.7: Maximum Mises stress distribution in a plate of uniform thickness with boundary conditions shown in Fig. 2.6 and analyzed with (a) linear FEM, (b) geometrically nonlinear FEM.

case aims to find a topology that maximizes the stiffness of the structure in the initial (undeformed) configuration, while simultaneously applying a volume and a stress constraint in the deformed configuration. For this last case, both linear and geometrically nonlinear finite element analysis are used.

For the first two case studies, a comparison between the algorithm developed here and the commercially available Abaqus Topology Optimization Module (ATOM) 2017-HF5 is provided. ATOM 2017-HF5 can efficiently perform size, shape, and topology optimization of isotropic shell structures. Hence, it can be used to examine the results obtained with the algorithm proposed in this study. Particular care was taken to assign the same optimization parameters to both algorithms, such as stiffness penalization factor, p, convergence criterion, and material interpolation scheme (SIMP). It was not possible to assign a stress penalization factor, q, and a stress norm parameter, P, to ATOM 2017-HF5. This indicates that it imposes stress constraints differently from the method used here. The values of these parameters are provided later in this chapter in each subsection describing the specific case study.

For the last case study, no comparison is provided, since ATOM 2017-HF5 cannot assign a stress constraint in a deformed configuration to a structure discretized with shell elements.

A summary of the results is shown in Table 2.1, while the following subsections

provide the details of the study. First, the table shows that the maximum Mises stress value for the volume constrained example is always higher than the maximum Mises stress value for examples with both volume and stress constraints (although the volume constraint remains the same in each case). For a thin plate in bending, a volume constraint does reduce the maximum Mises stress on the plate, if compared to the initial structure. Nevertheless, it does not automatically satisfy the imposed stress constraint.

Second, the table shows that the maximum stress reached when imposing a stress constraint on the deformed configuration is lower than the one reached when imposing the same constraint on the initial configuration, although the strain energy is slightly higher.

Finally, run-time values show one of the limitations of the algorithm proposed here, which takes much longer to reach convergence when compared to a commercial software like ATOM 2017-HF5. The added time is occupied by assigning new density values, ρ_e, to each element, and by the interaction between the different parts of the algorithm, such as a MATLAB script for the MMA optimization solver and Abaqus software for the finite element analysis.

Table 2.1: Topology optimization of thin plate in bending: summary of results

	Constraint	ATOM	Our Algorithm
Strain Energy [N mm]	Vol.	43.78	44.74
	Vol. + Init. Stress	39.90	39.12
	Vol. + Def. Stress	-	41.29
Volume Fraction	Vol.	0.499	0.500
	Vol. + Init. Stress	0.498	0.500
	Vol. + Def. Stress	-	0.500
Maximum Stress [MPa]	Vol.	205.0	199.7
	Vol. + Init. Stress	190.6	176.6
	Vol. + Def. Stress	-	173.9
Run-Time 6 CPUs [s]	Vol.	64	8505
	Vol. + Init. Stress	72	7983
	Vol. + Def. Stress	-	14291

2.6.1 Application of Volume Constraint

Results from the first case study are shown in Fig. 2.8. The stiffness penalization parameter chosen for this problem is $p = 3$ and the minimum radius for sensitivity filtering is $r_{min} = 1.4$ mm. Finally, the upper bound on material volume is $V^* =$

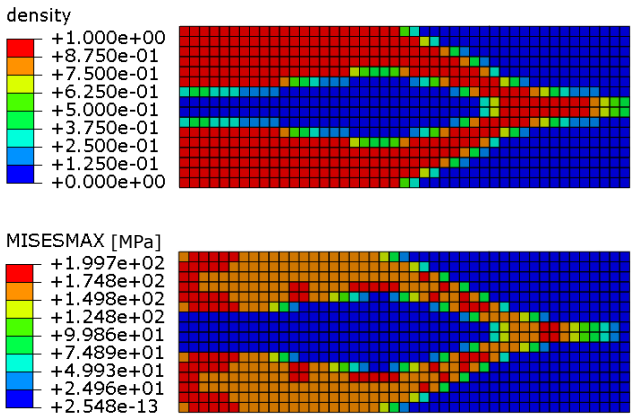

(a)

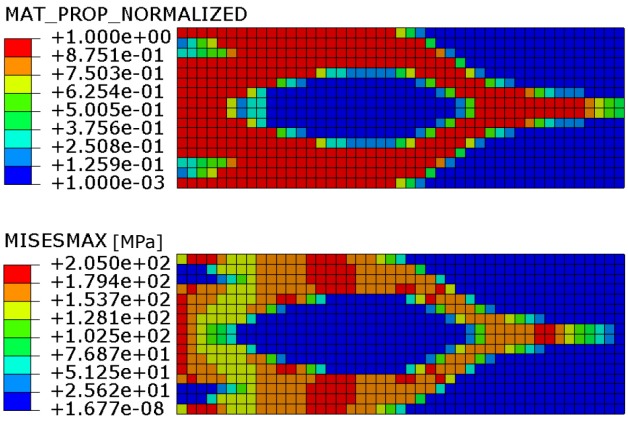

(b)

Figure 2.8: Solutions to thin plate in bending problem with volume constraint obtained with (a) algorithm presented here, (b) ATOM 2017-HF5 software.

0.5 V_0, which corresponds to eliminating half of the material available in the fully solid structure. Figure 2.8a shows the results obtained using the algorithm proposed here. Both an upper view of the density distribution, with an optimal topology of the structure outlined in red, and maximum Mises stress field on the same topology are presented. Figure 2.8b shows the results obtained using ATOM 2017-HF5.

The values of objective function (strain energy) and volume fraction, $V(\boldsymbol{\rho})/V_0$, are plotted in Fig. 2.9 for each iteration of the algorithm developed here. In the first few iterations the strain energy decreases and the volume fraction reaches its constrained value of 0.5. Afterwards, the volume fraction remains constant while the strain energy is maximized.

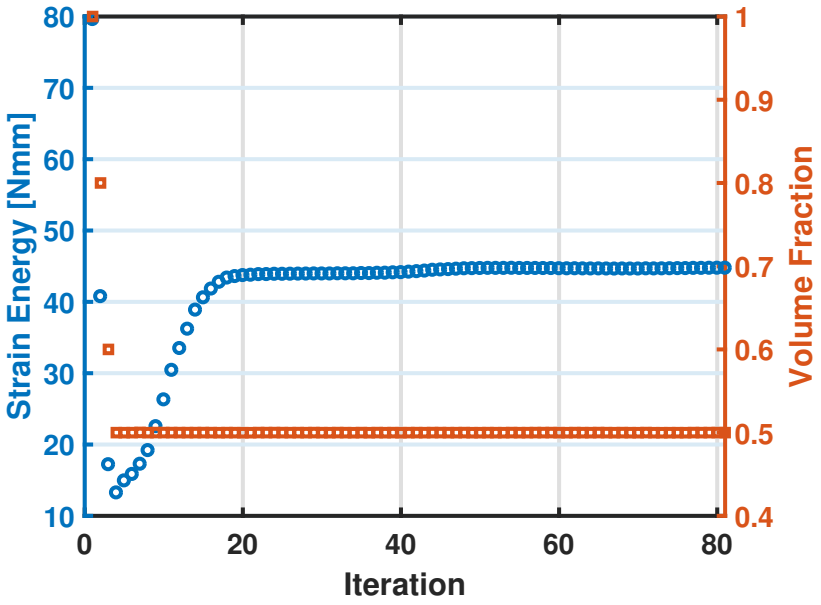

Figure 2.9: Convergence plot for a thin plate in bending with volume constraint. Values of objective function (strain energy) and constraint (volume fraction) are plotted at each iteration of the algorithm presented in this study.

2.6.2 Application of Volume and Stress Constraints in Initial Configuration

Results from the second case study are shown in Fig. 2.10. Stiffness penalization and filtering parameters are the same as in the volume-constrained example. In addition to a volume constraint, which corresponds to removing 50% of the material in the solid plate, a stress constraint in the initial configuration is applied. A stress penalization parameter $q = 1/2$ and a norm parameter $P = 6$ were chosen. The constraint limits a global stress measure of the final topology to be less than (or equal to) 70% of the same global stress measure of the solid plate (set as initial guess).

Figure 2.10a shows the results obtained using the algorithm proposed here. Both an upper view of the density distribution and maximum Mises stress field are presented. The density distribution is similar to the one obtained imposing only a volume constraint, but the maximum Mises stress value is lower. To reduce the stress values at the clamped edge, the new topology distributes material along the edge, leaving only a smaller cutout in the center. This happens because all the elements that discretize the structure are part of the design domain, including elements with boundary conditions. Hence, these elements may vanish. Figure 2.10b shows the results obtained using ATOM 2017-HF5. Also in this case the elements with

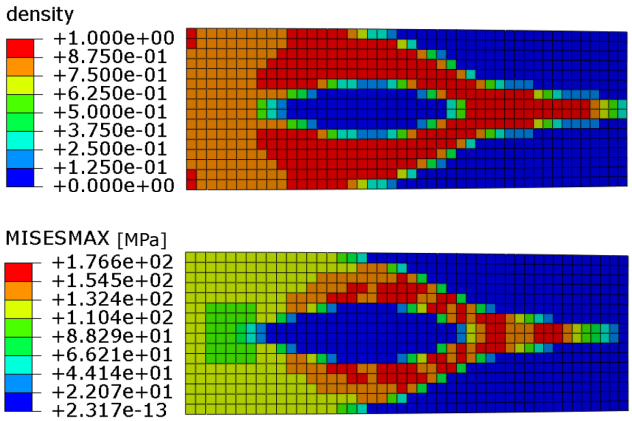

(a)

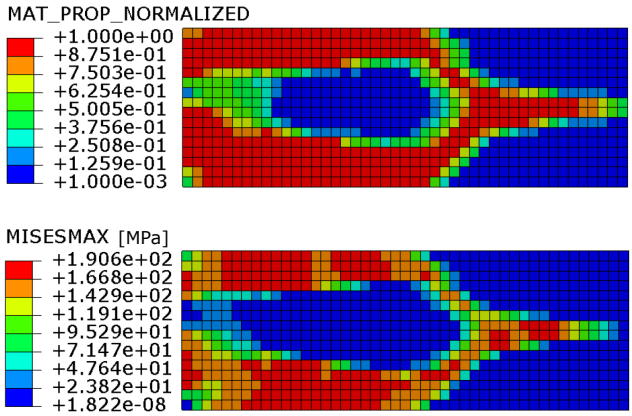

(b)

Figure 2.10: Solutions to thin plate in bending problem with volume and stress constraints in initial configuration obtained with (a) algorithm presented here, (b) ATOM 2017-HF5 software.

boundary conditions were included in the design domain.

The values of the objective function (strain energy), volume fraction, $V(\boldsymbol{\rho})/V_0$, and linear stress fraction, $\sigma_{PN}(\boldsymbol{\rho}, \mathbf{u})/\sigma^0_{PN}$, calculated at the initial configuration are plotted in Fig. 2.11 for each iteration of the algorithm developed here.

2.6.3 Application of Volume and Stress Constraints in Deformed Configuration

The results for the third case study are shown in Fig. 2.12. Stiffness penalization, filtering, stress penalization, and norm parameters are kept the same as in the second case study. The key difference is that this time the stress constraint was applied in the

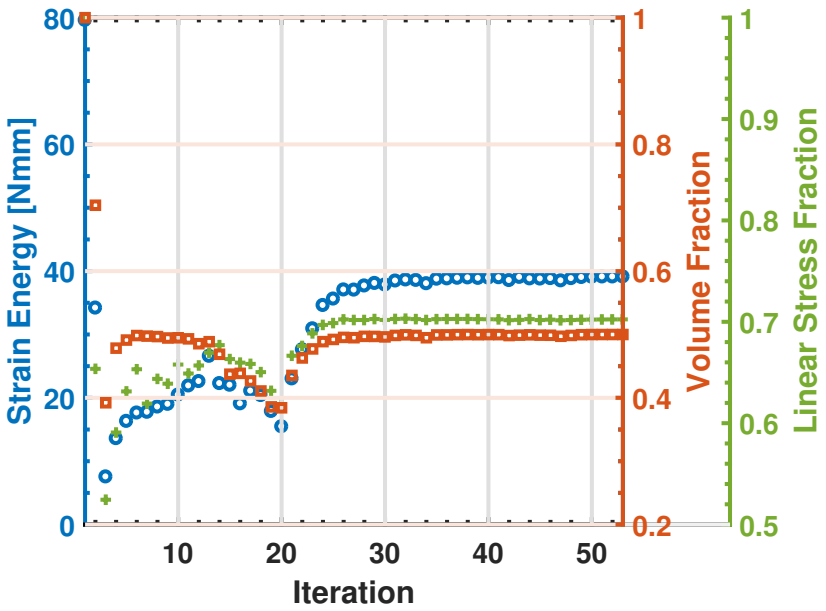

Figure 2.11: Convergence plot for thin plate in bending with volume and linear stress constraints. Values of objective function (strain energy) and constraints (volume fraction and stress fraction in initial configuration) are plotted at each iteration of the algorithm presented in this study.

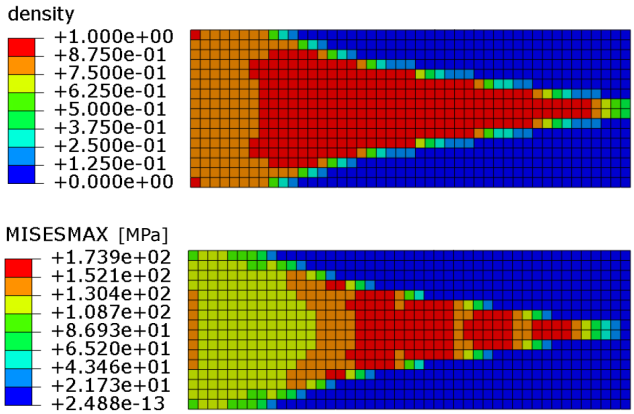

Figure 2.12: A solution to the thin plate in bending problem with volume and stress constraints in deformed configuration obtained with the algorithm presented here.

deformed configuration. Hence, a geometrically nonlinear finite element analysis was used to calculate the maximum Mises stress field on the solid plate, $\boldsymbol{\sigma}^{\mathbf{0}}_{\boldsymbol{VM}}$.

Although for this particular problem the stress field on the solid plate calculated with a linear finite element analysis is not very different from the one calculated with a nonlinear finite element analysis, Fig. 2.7, this small difference does affect

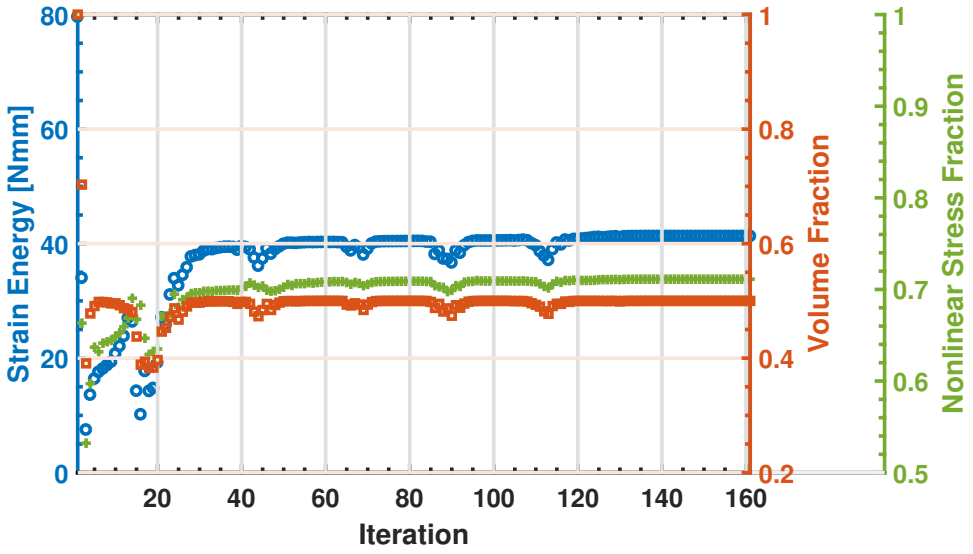

Figure 2.13: Convergence plot for thin plate in bending with volume and nonlinear stress constraints. Values of objective function (strain energy) and constraints (volume fraction and stress fraction in deformed configuration) are plotted at each iteration of the algorithm presented in this study.

the results of topology optimization. Figure 2.12 shows both optimized density distribution and maximum Mises stress field on this new shape. For this example, more material was removed from the sides of the plate, instead of creating a cutout in the middle of the plate as in the previous examples, thus forming a triangular shape. Since ATOM 2017-HF5 cannot apply a stress constraint in the deformed configuration on structures discretized with shell elements, the only result available is the one obtained using the algorithm developed in this study.

The values of objective function (strain energy), volume fraction, $V(\boldsymbol{\rho})/V_0$, and nonlinear stress fraction, $\sigma_{PN}(\boldsymbol{\rho}, \mathbf{u})/\sigma^0_{PN}$, calculated in the deformed configuration are plotted in Fig. 2.13 for each iteration of the algorithm developed here.

2.7 Thin Folding Tape Spring

Applying a stress constraint in deformed configuration is particularly important for shell structures that exhibit snap through during the course of the folding process, and thus develop very different stress fields when analyzed with linear and geometrically nonlinear finite element formulations. An example of this type of structures are tape springs, which are thin-walled, elastic strips with curved cross-section. Tape springs are most commonly used as tape measures, known as carpenter tapes. Because they can self-deploy using the strain energy formed in their folded configuration, tape

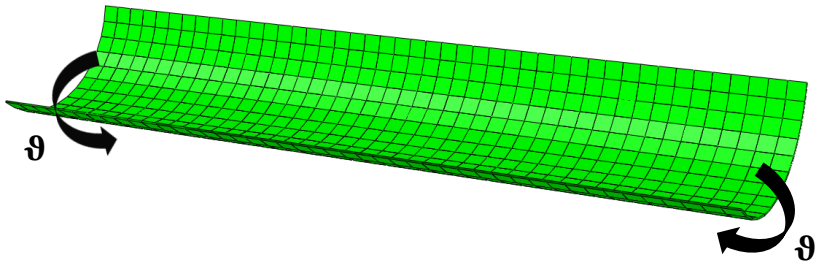

Figure 2.14: Design domain of a folding tape spring with boundary conditions.

springs have also been used for space applications, e.g., antennas for CubeStats (Dontchev, 2009) or a type of deployable boom known as STEM (Rimrott, 1966). Hence, maximizing the stiffness of a deployable tape spring, while limiting its weight and preventing it from being damaged when folded, is a very relevant problem for the space structures community.

The design domain is shown in Fig. 2.14 and it is a tape spring with transverse radius of curvature of 6 mm, aperture angle of 120°, and uniform thickness of 0.1 mm. The tape spring is 45 mm long and discretized with 585 shell elements. The material is isotropic with Young's modulus $E_0 = 70$ GPa and Poisson's ratio $\nu = 0.33$. Two equal and opposite rotations, θ, are applied at the two ends of the cylindrical shell. Each rotation is 30°, for a total folding angle of 60°. Since the problem is rotation driven, the objective function must be maximized.

The maximum Mises stress distribution on the plate is shown in Fig. 2.15. Both linear and geometrically nonlinear finite element formulations were used to analyze the structure and the results are shown respectively in Fig. 2.15a and 2.15b.

The problem of maximizing the stiffness of the tape spring in the initial configuration, while imposing a volume constraint and a stress constraint in the deformed configuration, was solved using the algorithm developed in this study. A volume constraint was set to remove half of the material from the solid structure. Concurrently, a stress constraint was set to limit a global stress measure (which approximates the maximum Mises stress value), calculated in the deformed configuration, to half the value of the same stress measure in the solid structure. Stiffness penalization is $p = 3$, filtering radius ir $r_{min} = 1.3$ mm, stress penalization is $q = 1/2$, and norm parameter is $P = 6$. To provide a comparison, a similar problem was solved using ATOM 2017-HF5 software, but imposing volume and stress constraints in the initial

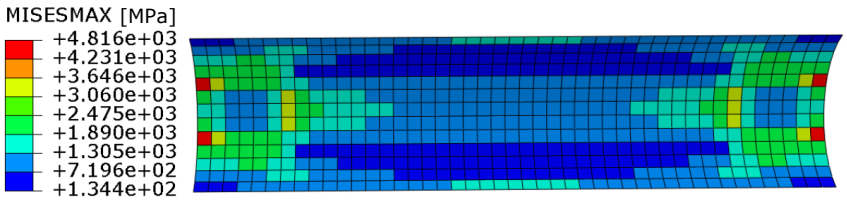

(a)

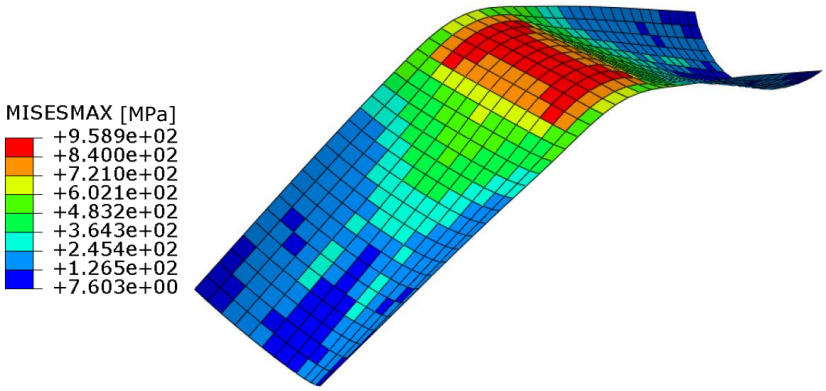

(b)

Figure 2.15: Maximum Mises stress distribution on a tape spring with boundary conditions shown in Fig. 2.14 and analyzed with (a) linear FEM, (b) geometrically nonlinear FEM.

configuration. The results are shown in Fig. 2.16 and are summarized in Table 2.2.

Table 2.2: Topology optimization of a thin folding tape spring: summary of results

	ATOM	Our Algorithm
Strain Energy [N m]	2.56	3.65
Volume Fraction	0.500	0.500
Maximum Stress [MPa]	1948	387.6
Run-Time 6 CPUs [s]	83	9120

To plot the maximum Mises stress field in deformed configuration, the elements with lowest density values ($\rho_e \leq 0.125$) were removed. In fact, the presence of low density elements causes computational problems, such as nonconvergence of the solution, particularly in structures that exhibit geometrical nonlinearities. This problem is discussed by Bruns and Tortorelli (2003), who implement element

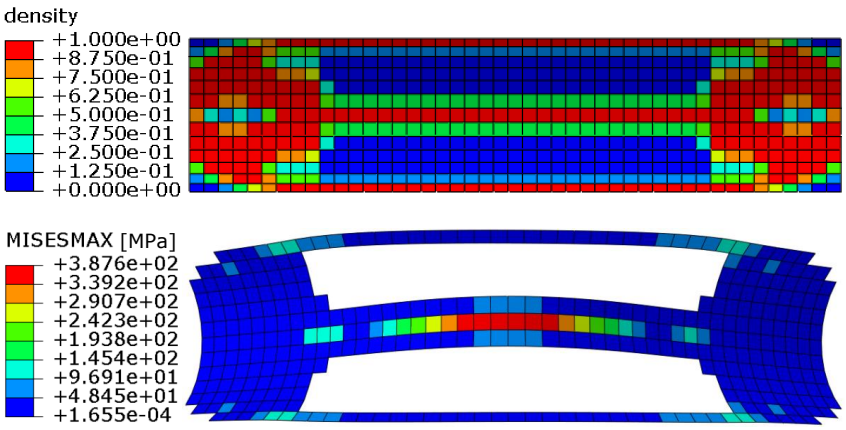

(a)

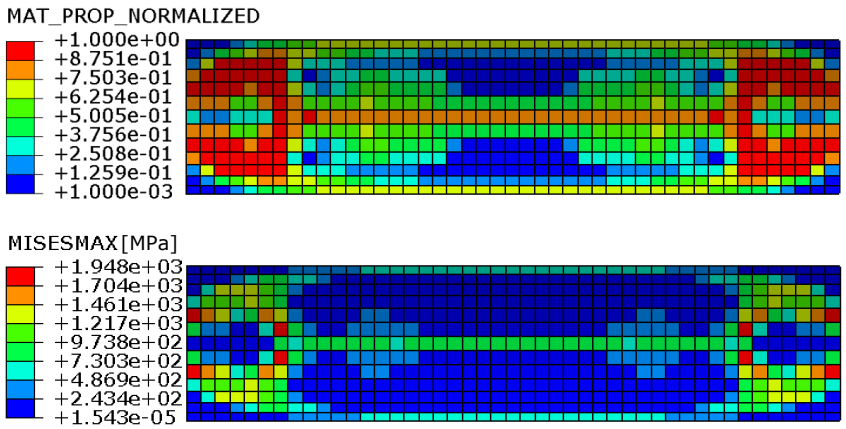

(b)

Figure 2.16: A solution to the folding tape spring problem with volume and stress constraints. (a) Algorithm presented here with constraints in deformed configuration. Elements with lowest density values ($\rho_e \leq 0.125$) were removed to plot the maximum Mises stress field. (b) ATOM 2017-HF5 software with constraints in initial configuration.

removal and reintroduction techniques to be able to run geometrically nonlinear topology optimization algorithms, and by F. Wang et al. (2014), who model the strain energy of low stiffness regions using small displacement theory and then use interpolation schemes to connect the strain energy in these regions with the one calculated in rest of the structure.

One advantage of the algorithm presented here is that a geometrically nonlinear finite element analysis is only performed once, for the solid structure, to calculate the maximum Mises stress field in deformed configuration. Afterwards, the algorithm performs linear simulations, as discussed in section 2.4.2. This approach ensures

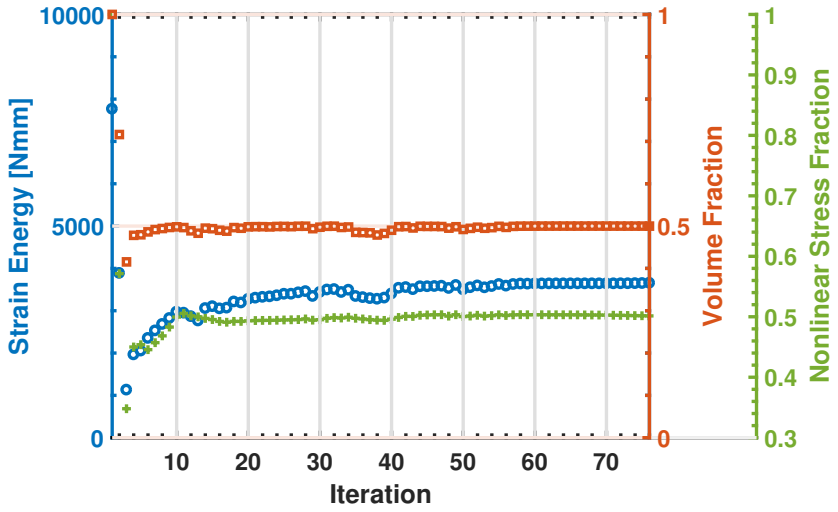

Figure 2.17: Convergence plot for folding tape spring with volume and nonlinear stress constraints. Values of objective function (strain energy) and constraints (volume fraction and stress fraction in deformed configuration) are plotted at each iteration of the algorithm presented in this study.

convergence of the finite element simulation at each iteration of the optimization loop.

Figure 2.17 shows the values of objective function (strain energy), volume fraction, $V(\boldsymbol{\rho})/V_0$, and nonlinear stress fraction, $\sigma_{PN}(\boldsymbol{\rho}, \mathbf{u})/\sigma^0_{PN}$, calculated in deformed configuration, for each iteration of the algorithm. The optimization study reaches convergence after 76 iterations and both volume and stress constraints are satisfied.

2.8 Conclusion

This chapter presented a study on the effects of volume and stress constraints imposed in a deformed configuration of thin shell structures using density-based topology optimization and proposed a new algorithm capable of applying these constraints. The advantage of density-based algorithms is that no assumptions on the position or the shape of the cutouts in the structure are necessary.

In particular, solutions for a thin plate in bending and a tape spring were provided. Three challenging aspects were considered: first, geometrical nonlinearities, second, a global stress constraint, and third, decoupling of topology optimization and the corresponding computational mechanics method, such as a finite element method. An algorithm for topology optimization, using a density-based method, was developed. Decoupling the finite element analysis of a structure at each optimization loop allowed to use Abaqus commercial software.

A simplified sensitivity analysis of the stress constraint was found. This allowed to run the geometrically nonlinear finite element simulation only once for the initial guess and avoid well-known problems, such as nonconvergence of solutions due to large element distortions. The results show that the assumption made to simplify the sensitivity analysis did not prevent the proposed algorithm from finding new topologies that satisfy the stress constraint.

First, a solution to a reference problem, the Messerschmidt-Bölkow-Blohm (MBB) Beam problem, was used to compare results from the algorithm developed through the present work and solutions provided in literature. A second case study was a thin plate in bending subject to volume, global stress, and combined volume and global stress constraints. The results obtained using linear FEM were examined against a commercial tool for topology optimization, ATOM 2017-HF5. Finally, solutions for a thin folding tape spring with volume and stress constraints in both initial and deformed configuration were provided. The solution obtained using the algorithm developed here shows a 30% increase in strain energy (hence deployed stiffness) compared to the solution obtained using ATOM 2017-HF5. Most importantly, this solution significantly reduced the maximum stress in deformed configuration.

The algorithm developed here can be used and adjusted to generate a wide range of solutions, but there are improvements that could be made. First, it could be generalized to study more complex materials, such as fiber reinforced composites, which are more interesting for deployable space structures. Second, since an approximation was made for the derivative of the global stress measure in the deformed configuration, additional studies can be performed to determine whether more optimal solutions can be found with different approximations, or without making this approximation. Finally, the algorithm can be written to interact more efficiently with the commercial finite element solver used here (Abaqus 2017), which would result in shorter run-times.

Chapter 3

TOPOLOGY AND SHAPE OPTIMIZATION OF COMPOSITE SELF-DEPLOYABLE THIN SHELLS

3.1 Introduction

The optimization method presented in chapter 2 has the advantage of not needing any assumptions on the initial position or shape of the cutouts. In theory, this makes the method generally applicable to any structural problem. In practice, a limitation of the method is having a large number of design variables, equal to the number of elements in a finite element discretization of the structure. Hence, it becomes computationally expensive for larger structures or more complex shapes, which require many elements. Recent studies have proposed solutions to increase the computational efficiency of a density-based approach to topology optimization (Aage et al., 2017). This field of research is beyond the scope of the studies presented here.

This chapter proposes two optimization methods applicable to self-deployable, thin shells forming a 90° corner and made entirely of fiber reinforced composite material.

The first method uses level-set functions to place cutouts on the shells, so that they can be folded without being damaged, while also maximizing the deployed stiffness. Although the type of functions used were of a specific kind, thus restricting the design space, this approach provides unique solutions to the concurrent optimization problem of composite, thin-shell structures with complex shapes and geometrical nonlinearities.

The second method uses a spline representation of the contour of a single cutout on the shell, thus performing a shape optimization of the cutout (Haftka and Grandhi, 1986). The cutout is placed in a convenient location on the shell, based on prior knowledge of its deformed shape. This approach is often used for fine tuning of solutions obtained using topology optimization methods (Maute and Ramm, 1997).

3.2 Background and Layout of the Chapter

Self-deployable structures made of composite materials have several advantages over traditional deployable structures with mechanical joints. Distinctive benefits are their lightweight, lower cost due to a smaller number of components, and friction-

insensitive behavior. Mechanical hinges can be replaced with lighter, smaller, and cheaper continuous elements made from thin composites.

Concepts for lightweight joints were previously proposed. Two examples are tape-spring rolamite (TSR) hinges (Watt and Pellegrino, 2002) and compliant hinges (Footdale, Banik, and T. Murphey, 2010). Hinges incorporating elastic memory composites have also been shown to be a viable approach for lightweight, cost-effective mechanisms, providing controlled, low-shock deployment and structural efficiency (Francis et al., 2003; Barrett et al., 2006). While concepts using tape spring hinges have been incorporated within straight tubes (Mobrem and Adams, 2009b; Mallikarachchi and Pellegrino, 2011), thin shells forming a corner that exploit cutouts to achieve foldability have not been studied before. Some examples of foldable thin shells are shown in Fig. 3.1. This chapter presents two methods to position cutouts on this type of shells and optimize their shape.

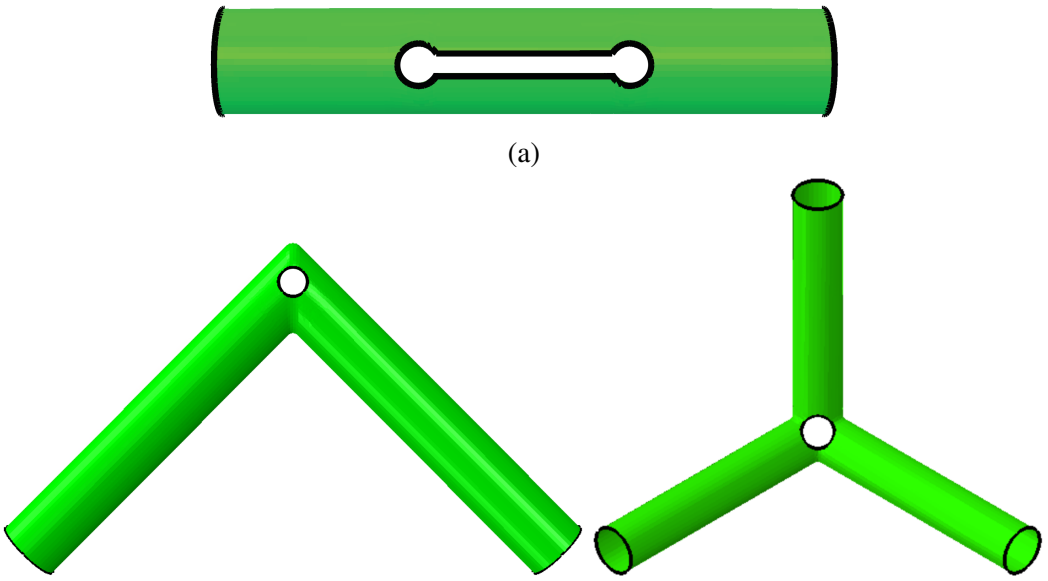

Figure 3.1: Examples of foldable thin shells with cutouts (a) tape spring hinge in straight tube (Mallikarachchi and Pellegrino, 2010), (b) concept of shells forming a corner, (c) concept of shells forming a three-way miter joint.

Shape optimization is chosen when a structural design solution already exists and studies are performed to explore the sensitivity of the existing solution to design variables, with the objective of improving the current solution. Some examples of shape optimization of composite, ultra-thin shells with geometrical nonlinearities are provided by Tan and Pellegrino (2006) and Mallikarachchi and Pellegrino (2010).

Like the work shown here, these studies also aim to maximize the deployed stiffness of the structure subject to a maximum stress limit in the packaged configuration. The design variables for the optimization problem are a few geometrical features of the structure under consideration. For example, Tan and Pellegrino (2006) optimize the angle and width of stiffeners and the angle of slits within thin-shell, deployable reflectors; while Mallikarachchi and Pellegrino (2010) optimize length, width, and diameter of slots for composite tape-spring hinges. Shape optimization requires a deep understanding of the mechanics of deformation of the structure and good engineering intuition to choose the parameters to be considered in the optimization.

Topology optimization makes no assumptions on the layout of the structure (Bendsøe and Sigmund, 2013; Andreassen, Clausen, et al., 2011). A review of different methodologies that use this approach was completed by Sigmund and Maute (2013). Level-set methods play an important role amongst these techniques (M. Y. Wang, X. Wang, and Guo, 2003). Different studies have tackled various challenges for topology optimization. First, geometrical nonlinearities were taken into account by Buhl, Pedersen, and Sigmund (2000), Pedersen, Buhl, and Sigmund (2001), Bruns and Tortorelli (2003), Cho and Jung (2003), and F. Wang et al. (2014).

The challenge of performing topology optimization using shell elements was addressed by Pedersen, Bose, et al. (2017) and Ye et al. (2019). For example, Pedersen, Bose, et al. (2017) uses a commercial software, Abaqus 2017, to optimize a car bumper, modeled with shell finite elements, by creating a structure with variable thickness. Since the thickness is not allowed to become zero, cutouts cannot be formed in the structure. Nevertheless, interesting results are shown for nonlinear sizing of shell thicknesses using adjoint sensitivities and including the simultaneous modeling of three nonlinearities: large deformations, plasticity, and contact.

A different study by Ye et al. (2019) uses a level-set method, which allows for formation of cutouts, to optimize shell structures, but without including geometrical or material nonlinearities. Level-set topology optimization methods were also used by Maute, Tkachuk, et al. (2015) to optimize 3D printed composites, and by Geiss et al. (2019), for shell structures undergoing large deformations. Finally, topology optimization problems including composite materials were analyzed by Sigmund and Torquato (1996) and Sigmund (2000) using numerical homogenization. This technique is also used to compute composite materials' properties (Andreassen and Andreasen, 2014).

This chapter presents topology and shape optimization studies on composite, thin

shells forming a corner that can fold and self-deploy. First, a design with no cutouts is presented and the choices of a particular material and laminate are discussed. Then, techniques to analyze the shell are introduced: specifically, we present a geometrically nonlinear finite element analysis, to study the folding behaviour of the shell, and a failure criterion, which will be discussed in greater detail in chapter 4. The criterion is used to extend finite element simulations and predict the onset of failure in folded shells.

The problem of finding the number, location, and shape of cutouts to place in a shell so that it can be folded without being damaged, while maximizing their deployed stiffness, is studied. First, preliminary design choices based on physical intuition are shown. Second, an optimization approach that uses level-set functions is proposed. Third, shape optimization of a single cutout is implemented. Finally, thin shells forming a corner, with cutouts derived from the optimization studies, are built and tested.

3.3 Design of Self-Deployable Thin Shells Forming a Corner

Self-deployable thin shells forming a structural element with a 90° corner were chosen as a case study. The structure is composed of two thin-walled tubes intersecting at 90°, Fig. 3.2. This shape, although quite simple, introduces the geometrical complication of non-zero Gaussian curvature at the intersection of the two tubes. The structure must fold, with the two tubes rotating towards each other, and the total folding angle is the sum of the folding angles of the two tubes. The total folding angle, geometry of the shell, and composite material were chosen as follows:

- Total folding angle is 45°.
- Diameter of each thin-walled tube is 32 mm and length is 200 mm.
- Thickness of the shell ranges between 90 and 390 μm depending on layup.
- Material is plain-weave 525 Astroquartz® II fabric (quartz fiber), from JPS Composite Materials (JPS, 2017), pre-impregnated with PMT-F6 cyanate ester resin, from PATZ Materials & Technologies (PATZ, 2019).

The folding angle was chosen based on convergence of geometrically nonlinear finite element simulations, described later in this chapter, to allow fast numerical simulations needed to perform optimization studies. Nonconvergence of iterative

finite element solvers is an issue when implementing large displacement simulations of composite, thin shells. Many authors have addressed this issue by running explicit simulations with very small increments, to obtain accurate results (Soykasap, 2009; Banik and T. Murphey, 2010; Mallikarachchi and Pellegrino, 2011; Stabile and Laurenzi, 2014).

Benchmark problems have been used to compare implicit and explicit solver of Sierra Solid Mechanics code (Peterson and Mobrem, 2017; Mobrem, Peterson, et al., 2017). Generally, the drawback of choosing an explicit solver is longer simulation times, which is not a viable option when running optimization studies. Therefore, an implicit solver is adopted in this study, and the largest folding angle is restricted to 45°. Resolving nonconvergence issues for larger folding angles is beyond the scope of this study.

A plain-weave, quartz fiber composite was chosen because of its higher ultimate strain (2.6% measured in tensile tests of $[0_{pw}]_2$ and $[0_{pw}]_4$ samples) compared to carbon fiber (0.95% from technical data sheet by NTPT (2018)), which is useful to fold the shell. More details on material characterization are provided in chapter 4. Considering that the 0° direction of the fibers corresponds to the axial direction of each tube, the layup is composed of four regions of two, three, four and six plies respectively, as shown in Fig. 3.2. The plies are oriented as follows: two-ply regions $[45_{pw}]_2$, three-ply regions $[45_{pw}/0_{pw}/45_{pw}]$, four-ply regions $[45_{pw}]_4$, and six-ply regions $[45_{pw}/45_{pw}/0_{pw}]_s$, where 0_{pw} and 45_{pw} indicate plain-weave laminae consisting of fibers oriented respectively at $0/90°$ and $+45/-45°$. A single ply is 90 μm thick.

This layup was chosen based on preliminary folding experiments. A two-ply region with fibers oriented at 45° was placed at the corner. This thinner region makes the shell more compliant and therefore easier to fold. Because the shell must also be stiff when deployed, an additional ply oriented at 0° was added to each tube, thus forming a three-ply region. Finally, four-ply and six-ply regions exist because of manufacturing capabilities, described in Appendix A, used to build thin shells forming a corner.

3.4 Analysis Techniques

Two techniques were adopted to study these thin shells. First, a finite element model was used to analyze the folding behavior and to locate the areas where stress concentrations occur when the shells are folded. This analysis allowed us to identify

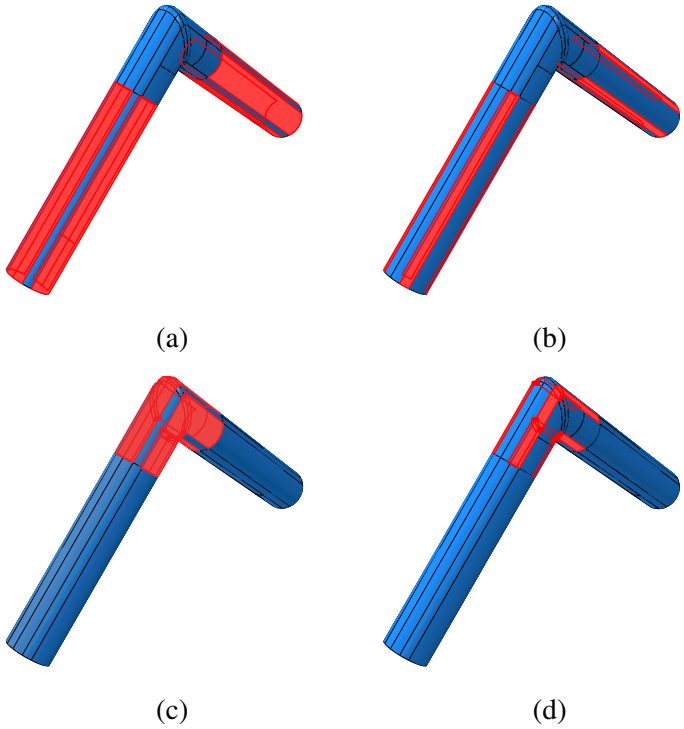

Figure 3.2: Regions of shell forming a corner, with different laminates (a) 3 plies, (b) 6 plies, (c) 2 plies, (d) 4 plies.

where to place the cutouts. Second, a failure criterion for thin, plain-weave, FRP laminates was implemented to numerically detect the onset of failure.

Geometrically nonlinear finite element simulations were carried out using the commercial software Abaqus 2017. Different types of shell elements (S3, S4, and S4R) were tested and S4R shell elements were chosen to run the simulations because the results obtained using S4R shell elements produced a better match with the experimental results shown in section 3.7.3.

The four different layups described before were defined in the model, using a feature provided in Abaqus and called "general section properties", which allows to manually input the ABD stiffness matrix of a composite material. The provided ABD matrix was tuned to match the bending stiffness matrix, D, of each layup.

The full ABD matrix was calculated using Soykasap's micromechanical models (Soykasap, 2006), which extend classical lamination theory to woven composites. Additionally, a correction to the D matrix was applied to match the results of 4-point bending experiments. The experiments measured the terms $D_{11} = D_{22}$ and found that the micromechanical models over-predict these terms for ultra-thin composites.

Using the experimental results, correction factors were calculated for each layup and applied to every term of the D matrix, while the matrices A and B were left unchanged. Chapter 4 shows the experimental results and a summary of correction factors for each layup, in Table 4.4.

Figure 3.3 shows the boundary conditions applied to the finite element model. Three massless reference points, RP_{center}, RP_{left}, and RP_{right}, were defined. Two rectangular patches, shown in red, were coupled to the left and right reference points such that the in-plane rotations of the patches, θ_x, match the rotations imposed to the reference points. The rotations of the three points were coupled so that the sum of the rotations of the left and right reference points equals the rotation of the center one, which was set at 45°. This technique was implemented to keep the reaction moments equal at both ends of the shell, to simulate the boundary conditions applied in the experimental characterization of the shell, section 3.7.3. Finally, two nodes at the bottom of the shell, shown by red dots in Fig. 3.3, were constrained to remain in the y-z plane and all the translations of the node at the top were set to zero.

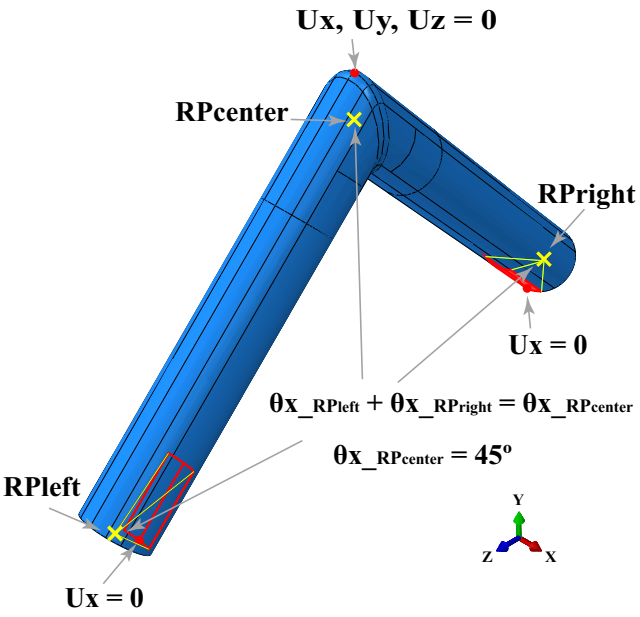

Figure 3.3: Finite element model and boundary conditions.

The simulations were carried out with an implicit solver, where after each increment the analysis starts Newton-Raphson iterations to enforce equilibrium of the internal forces with the external loads. Convergence settings based on "half-increment residual tolerance" were used. This tolerance represents the equilibrium residual error (out-of-balance forces) halfway through a time increment. If the half-increment

residual is small, it indicates that the accuracy of the solution is high and that the time step can be increased; conversely, if the half-increment residual is large, the time step used in the solution should be reduced. The Abaqus default half-increment residual tolerance was used, which is set at 1000 times the time average force and moment values, for applications without contact. A result from the finite element model simulations is shown in Fig. 3.4.

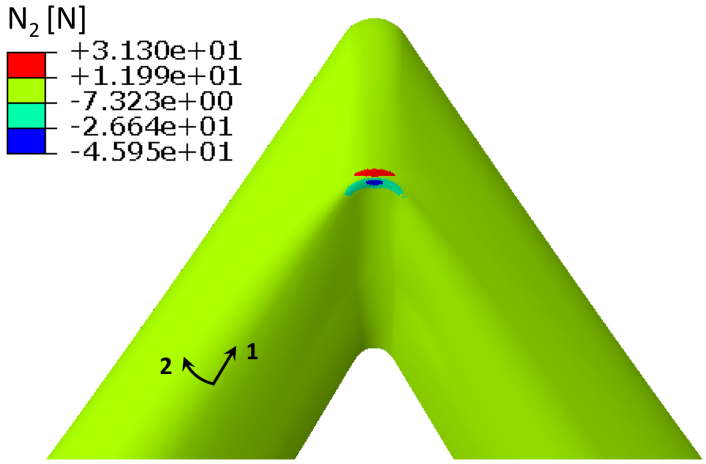

Figure 3.4: Contour plot of stress resultants in shell without cutouts folded 45°.

The laminate failure criterion by Mallikarachchi and Pellegrino (2013), described in detail in chapter 4, is used to predict the onset of failure in folded shells. The criterion applies to layups with same orientation plies. Therefore, only regions with two and four plies can be analyzed, since all the plies are oriented at ± 45°. This limitation is acceptable because the numerical result in Fig. 3.4 shows localized stress resultants where the region with two plies is located.

The three failure indices in Eq. 4.16-4.18 were calculated at each step of the simulations and contour plots were obtained. For all cases examined in this study, the largest values of the failure indices are reached in the two-ply regions and the first failure index FI_1 is the most critical. Therefore, the rest of this study will only examine FI_1 in the two-ply regions.

As an example, a shell with a circular cutout was analyzed and is shown in Fig. 3.5. According to the failure criterion, any failure index exceeding the value of 1 predicts the onset of failure on the shell. Black areas plotted in Fig. 3.5 are regions where the first failure index is smaller than 1. White areas are regions corresponding to cutouts or parts of the shell that were excluded from the failure analysis. Finally, all

the elements plotted with a color other than white or black have reached a failure index greater than 1.

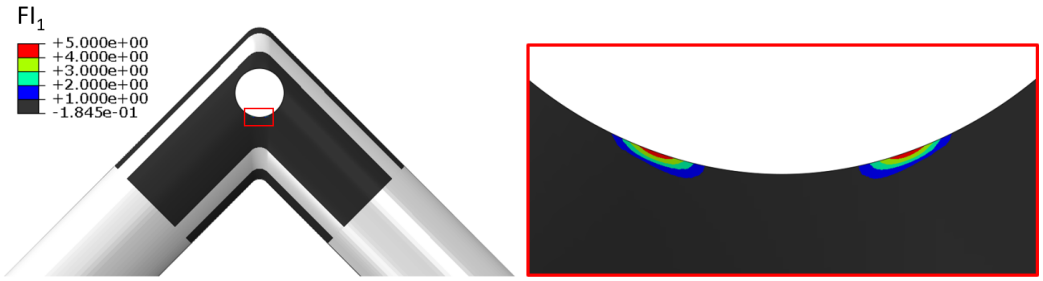

(a) (b)

Figure 3.5: Contour plots of in-plane failure index FI_1 corresponding to a shell folded 45°. FI_1 has been mapped onto a deployed shell.

3.5 Preliminary Designs Based on Physical Intuition

An initial attempt to place cutouts was guided by the results from the finite element analyses. A contour plot of the circumferential curvature change k_c in each of the tubes is shown in Fig. 3.6a. An intuitive design approach to reduce the stress peaks is to simply place cutouts where the highest localized curvature changes are reached. A first design was obtained by placing circular cutouts with 14 mm diameter and centered on the region of highest localized curvature change, Fig. 3.6a.

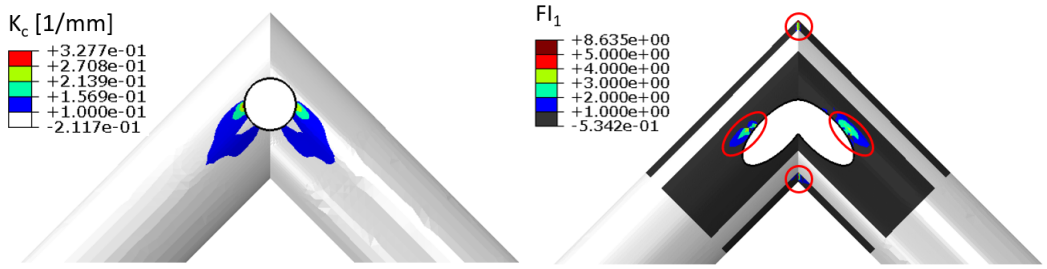

(a) (b)

Figure 3.6: Shells with sharp corners folded 45° (a) contour plot of circumferential curvature change, K_c, on shell with circular cutout, (b) contour plot of FI_1 on shell with cutout made of intersecting ellipses. Both K_c and FI_1 have been mapped onto deployed shells.

A second class of cutout shapes, Fig. 3.6b, was obtained by intersecting two ellipses and symmetrically varying the major and minor axes of each ellipse. Elliptical cutouts were chosen to eliminate wider areas of the shell, following the contour plot in Fig. 3.6a . The areas on the shell with $FI_1 > 1$ are circled in red in Fig. 3.6b and show that the elliptical cutouts do not prevent the shell from being damaged.

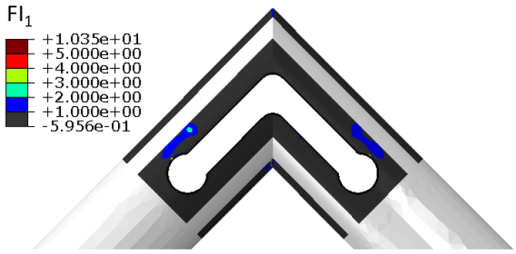

Figure 3.7: Contour plot of FI_1 on shell folded 45° with cutout inspired by cylindrical booms with slotted hinges (Mobrem and Adams, 2009b; Mallikarachchi and Pellegrino, 2010). FI_1 has been mapped onto a deployed shell.

The cutout shape in Fig. 3.7 was inspired by designs previously developed for thin-shell, cylindrical booms with slotted hinges (Mobrem and Adams, 2009b; Mallikarachchi and Pellegrino, 2010) and shown in Fig. 3.1a. A contour plot of the first failure index shows that this kind of shape does not prevent damage of the shell. Therefore, larger cutouts were explored. A successful design, shown in Fig. 3.8, was found by partially removing the two-ply region. Figure 3.8b shows that localized fold lines form near the edges of the cutout, thus allowing the shell to fold 45° while $FI_1 < 1$. Partially removing the two-ply region of the shell resolved the issue of material damage, but also greatly reduced the stiffness of the shell in comparison to other cutout shapes. The bending stiffness and the maximum value of the first failure index for the cutouts considered in this section are summarized at the end of the chapter, in Table 3.1 and Fig. 3.18.

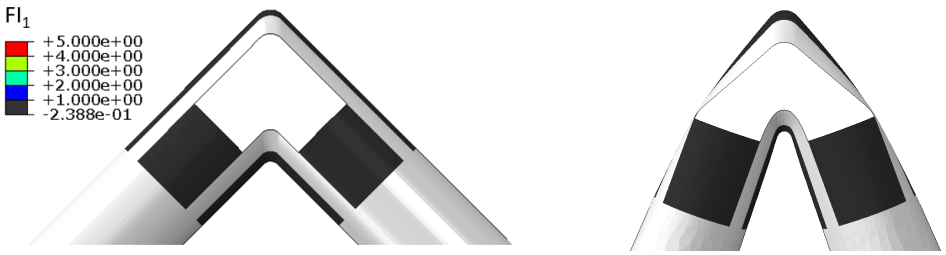

(a) (b)

Figure 3.8: Successful shape with smooth corners and partially removed two-ply region. (a) Contour plot of FI_1 on deployed shell, (b) contour plot of FI_1 on shell folded 45°.

3.6 Optimization Problem Formulation

The problem of finding a better shape, number, and position of cutouts to fulfill the stiffness requirements and failure constraints of a self-deployable shell forming

a corner was studied by a numerical optimization. The minimization problem is defined as follows:

$$\begin{aligned} \min_{x_1 \ldots x_n} \quad & : -K_B \\ \text{subject to} : \; & \alpha_i < x_i < \beta_i, \qquad i = 1, 2, 3, \ldots, n \\ & : \max\left(FI_1\right) < 1 \end{aligned} \tag{3.1}$$

where n is the number of design variables. The objective function in Eq. (3.1) is the bending stiffness of the shell in the deployed configuration. Successful cutouts, generated via optimization techniques that will be discussed in the next two sections, must satisfy two constraints. First, they must remain within specified boundaries, α and β, defined by the geometry of the shell. Second, they must prevent damage of the shell, thus constraining the maximum value of the first failure index in the folded configuration to be less than one. Two optimization approaches are presented. The first approach uses level-set functions for topology optimization of the shell, and the second approach applies a shape optimization technique (Haftka and Grandhi, 1986).

3.7 Topology Optimization using Level-Set Functions

Level-sets were introduced in chapter 2. Here, a topology optimization approach using level-set functions was studied. This method has the advantage of reducing the number of design variables when compared to a density-based approach (Bendsøe and Sigmund, 2013) discussed in chapter 2. It also allows for a broad exploration of shapes, number and position of cutouts. First, the algorithm assigns values to the design variables, then generates new shapes of cutouts based on those values. Once these shapes are created, a Python script generates an input file for the finite element software, Abaqus 2017, which runs a finite element analysis and returns the values of the first failure index and the overall bending stiffness of the structure.

3.7.1 Method Description

A 3-D basis function, $z = f(x_p, y_p)$, is defined on a projection plane tangent to the side of the shell. The basis function is chosen such that it vanishes at the boundaries of its domain. Hence, the geometrical constraints of the optimization problem in Eq. (3.1) are automatically satisfied. A cutting plane, parallel to the $x_p - y_p$ plane, is then introduced such that contour shapes are formed. The z-coordinate of the plane directly influences the contour shapes that are generated through the intersection of

the plane and the chosen basis function.

The method is divided into four steps, shown in Fig. 3.9. The first step, Fig. 3.9a-3.9b, consists in finding a mapping between a convenient domain, on which the basis function is described (in this case a square), and the domain on which the contours of the cutouts are generated. The latter was chosen as an L-shaped, smooth domain that represents a portion of the side view of the shell. The second step, Fig. 3.9c, involves choosing a basis function and applying the mapping to it. Two basis functions were investigated, a series of cosines squared:

$$z = \sum_{h=1}^{N_h} \sum_{l=1}^{N_l} a_n \left[\cos\left(2h+1\right)\frac{\pi x_p}{2} \times \cos\left(2l+1\right)\frac{\pi y_p}{2} \right]^2, n = 1, 2, 3, ..., N_h N_l \quad (3.2)$$

and a series of cosines and sines squared:

$$z = \sum_{h=1}^{N_h} \sum_{l=1}^{N_l} a_n \left[\left(\cos\left(2h+1\right)\frac{\pi x_p}{2} + \sin\left(h\pi x_p\right) \right) \left(\cos\left(2l+1\right)\frac{\pi y_p}{2} + \sin\left(l\pi y_p\right) \right) \right]^2, \qquad n = 1, 2, 3, ..., N_h N_l \quad (3.3)$$

These functions were chosen because they vanish at the boundaries of their domain, which is a square bounded between -1 and 1 along x_p and y_p, and because they form a different number of peaks by changing the numbers of terms in the series. The third step, Fig. 3.9d, consists in intersecting the chosen basis function with a plane parallel to the $x_p - y_p$ plane. Once the basis function is chosen, the only design variables used to define the problem and carry out the optimization analysis are the z-coordinate at which the cutting plane is set, $z = c$, and the numbers of terms in the series, N_h and N_l, which define how many peaks the function will have, thus defining the number of separate cutouts.

Because there are three design variables, no particular optimization algorithm was chosen. Instead, the entire design space was evaluated. In this study, the coefficients of the series, a_n, where chosen equal to 1 for simplicity. Additionally, the inclination angles between the cutting plane and the $x_p - y_p$ plane were set at 0° (parallel planes), but could also be chosen as design variables to generate a wider range of shapes.

Examples of shapes of cutouts that can be obtained by intersecting a mapped basis function with different planes, $z = c_1$ and $z = c_2$, are shown in Fig. 3.10.

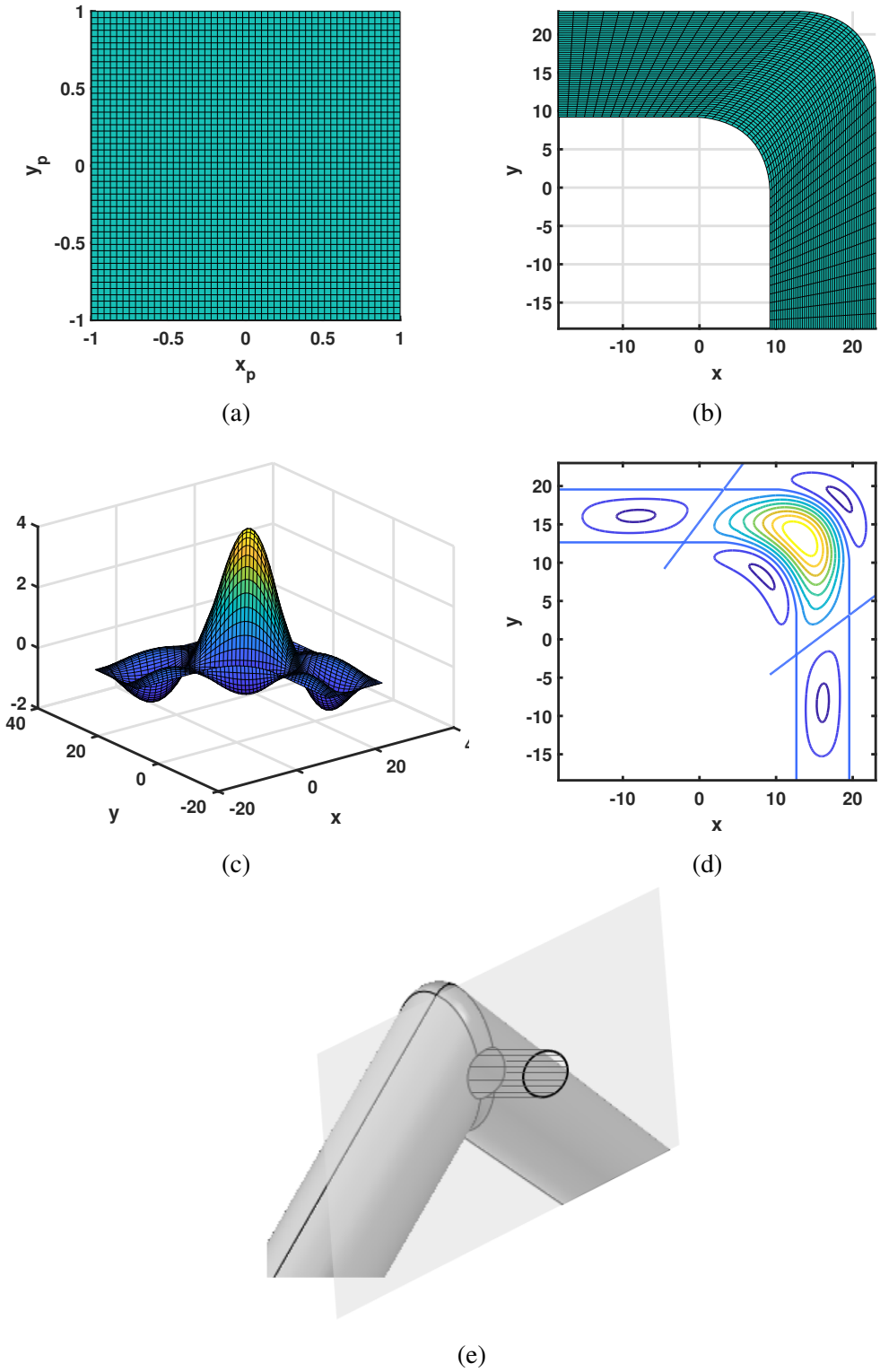

Figure 3.9: Steps of topology optimization method using level-set functions: (a) choose a convenient domain to generate a basis function, (b) define a mapping, (c) choose basis function and apply mapping, (d) cut function at z = constant, and (e) project cutout onto the shell.

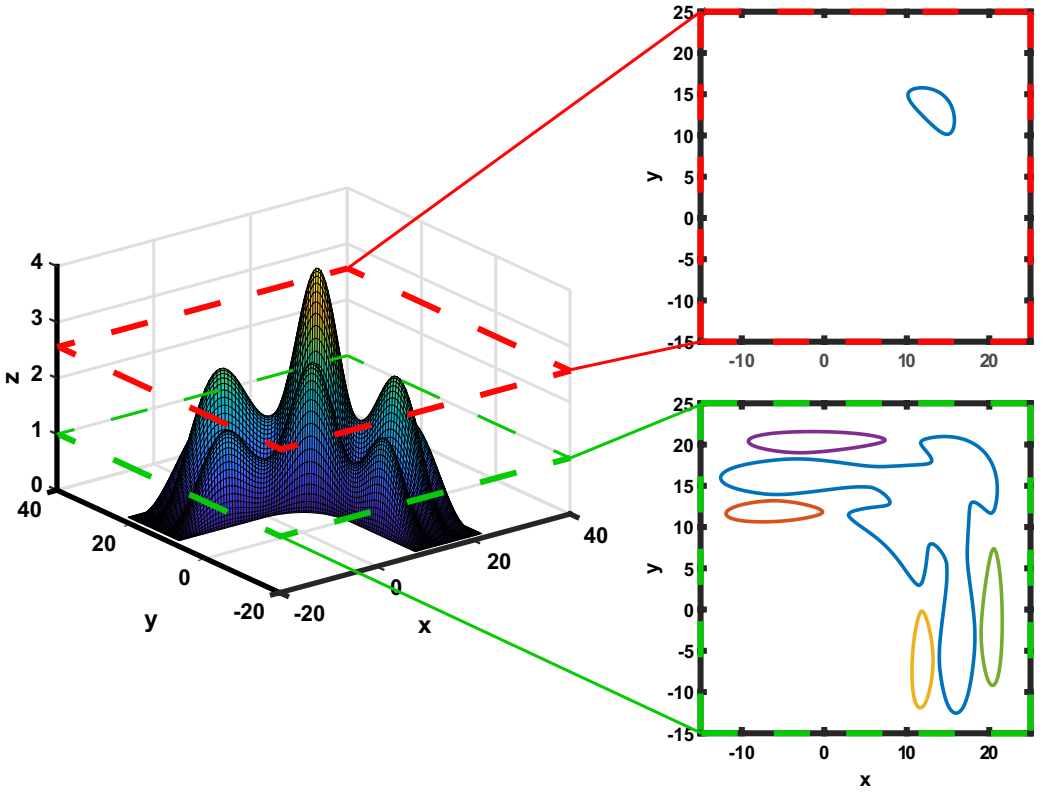

Figure 3.10: Examples of cutout shapes obtained by intersecting a chosen basis function, Eq. 3.2, with planes $z = 1$ and $z = 2.6$.

3.7.2 Results from Level-Set Method

Three examples of shell designs generated using the level-set optimization approach are shown in Figs. 3.11a - 3.11c. The first design, Fig. 3.11a, was obtained using Eq. (3.2) and hence, the shapes of the cutouts are symmetric. This design produced the highest bending stiffness, while satisfying the constraint placed on the maximum value of the first failure index, and was obtained for the choice $N_h = 0$ and $N_l = 2$. The boomerang-shaped cutouts leave strips of material connecting the right and left parts of the shell, thus providing additional bending stiffness.

The second design, Fig. 3.11b, was again obtained using a series of cosines squared, but choosing $N_h = 1$ and $N_l = 2$. The cutout at the center removes areas of localized stresses, while thin slits on the sides help releasing stress when the shell is folded.

Finally, the third design, Fig. 3.11c , was obtained using Eq. (3.3), and this results in a non-symmetric cutout. The shape in Fig. 3.11c was obtained by choosing $N_h = 2$ and $N_l = 0$. Despite being the best result obtained using a non-symmetric basis function, the cutout is larger, therefore the shell has a lower bending stiffness when

compared to shells with symmetric cutouts. A summary of the bending stiffness and the maximum value of the first failure index for these three designs is provided in Table 3.1 and in Fig. 3.18.

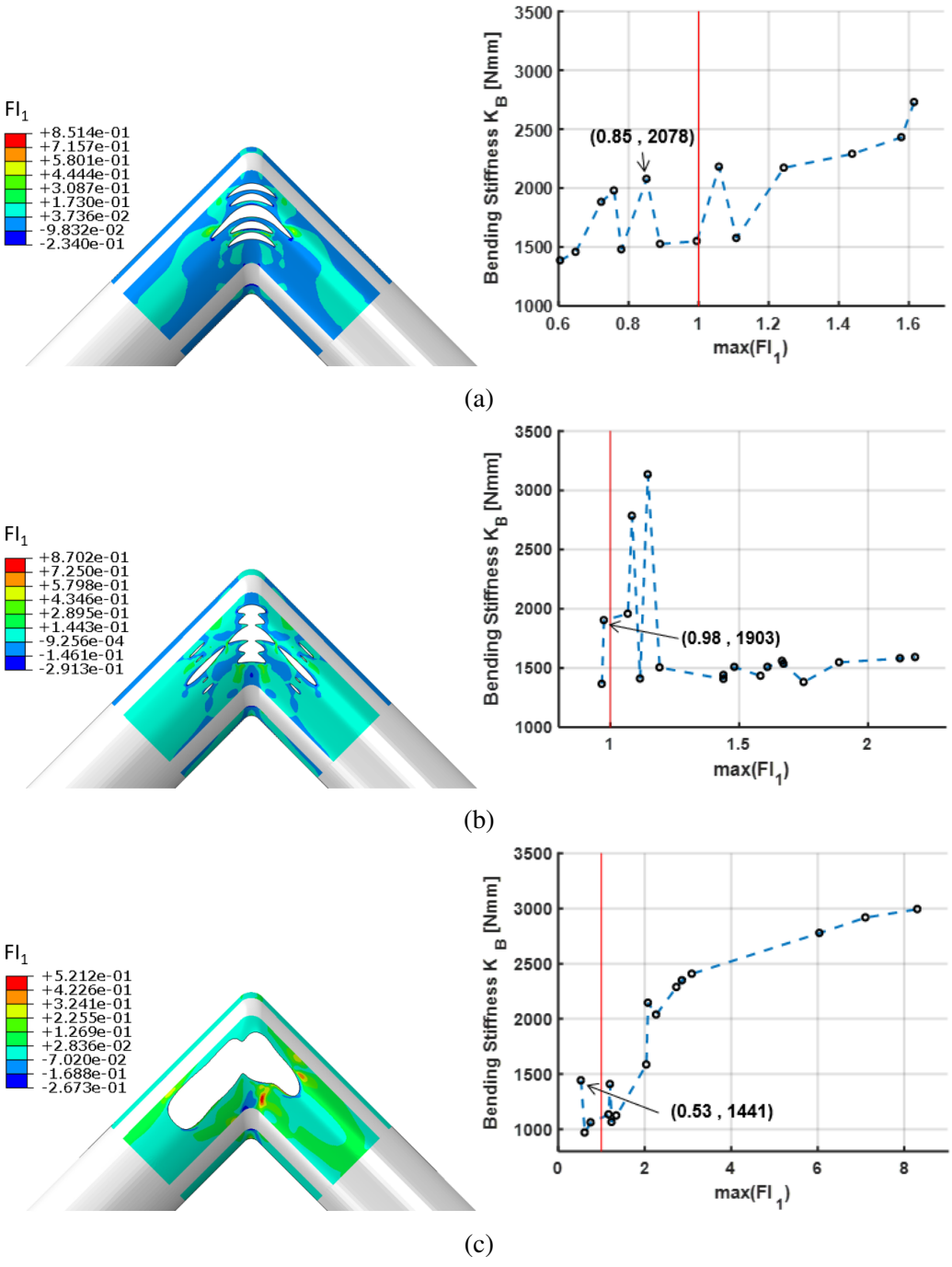

Figure 3.11: Results from level-set method, obtained using (a) Eq. (3.2) and $\mathbf{N_h}$=0, $\mathbf{N_l}$=2, (b) Eq. (3.2) and $\mathbf{N_h}$=1, $\mathbf{N_l}$=2, (c) Eq. (3.3) and $\mathbf{N_h}$=2, $\mathbf{N_l}$=0.

3.7.3 Experimental Verification of Level-Set Method Results

To experimentally verify the results from the level-set optimization method, a self-deployable shell was built using the silicon molding manufacturing technique described in Appendix A. The cutouts in Fig. 3.11a were laser-cut onto the shell.

A quasi-static folding experiment was conducted using the setup shown in Fig. 3.12a. Two 35 mm × 15 mm curved clamps that conformed to the curvature of the cylindrical tubes were used. The clamps constrained a small region at the end of each tube, thus leaving the end cross-sections free to ovalize. The same boundary conditions were applied in the numerical simulations. The clamps also connected the tubes to brackets that were initially aligned at 45°, to mount the shell in a stress free configuration.

The experiment was rotation controlled, to match the numerical simulations, and the rotations were imposed manually, through two gear boxes. One of the brackets was mounted on ball bearings and it was free to slide towards the other. The brackets were mounted on gearboxes, connected to strain gauges and a data acquisition system. Once the sliding bracket had been rotated by a small angle (1-3°), the reaction moment from the tube connected to that bracket was recorded. The second, fixed bracket was then rotated until the reaction moment recorded on the attached tube equaled the one recorded on the other tube. This process was repeated until the shell was folded to 45°.

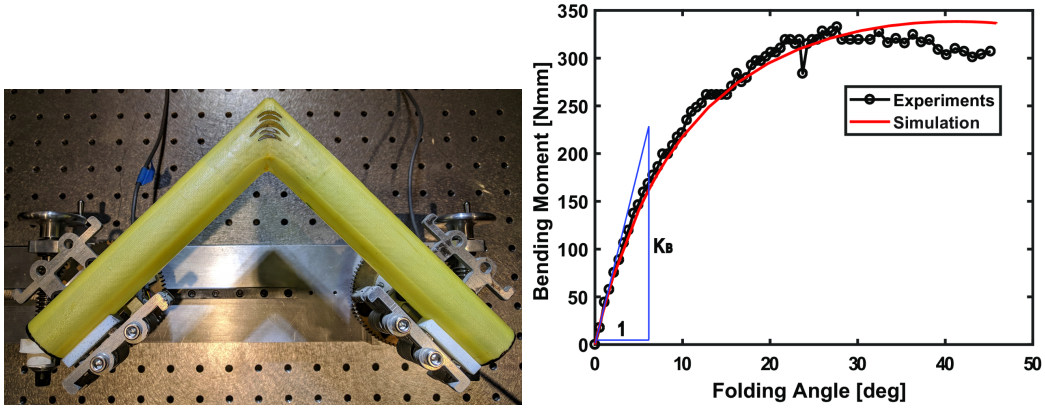

(a) (b)

Figure 3.12: Folding experiment (a) setup, (b) test data and comparison to simulation results. The graph shows the reaction bending moments plotted against the folding angle; a folding angle of 0° corresponds to a fully deployed shell.

At the end of the test, the moment-rotation profile was obtained by plotting the folding angle and the corresponding moment at each step, Fig. 3.12b. The moment-

rotation profile resulting from numerical simulations was then superposed to the experimental results. The two curves show good agreement for the first 30° of folding, but deviate from each other for the last 15°, possibly due to manufacturing imperfections of the physical shell and to the fact that the simulation was built using a linear material model.

Two results stand out from this experiment. First, the bending stiffness of the deployed shell predicted by the simulation matches the bending stiffness of the shell in the deployed configuration, defined by the tangent at the origin of the moment-rotation curve as follows:

$$K_B = \frac{\Delta M_0}{\Delta \theta_0} \tag{3.4}$$

where ΔM_0 is the linear increment in bending moment measured on the tangent to the moment-rotation curve at the initial point ($M = 0$, $\theta = 0$), and $\Delta \theta_0$ is the linear increment in folding angle, measured in radians, on the same tangent. Second, no damage was observed after folding the shell 3 times and the deployed bending stiffness, experimentally measured via moment-rotation curve, did not change before and after the shell had been folded.

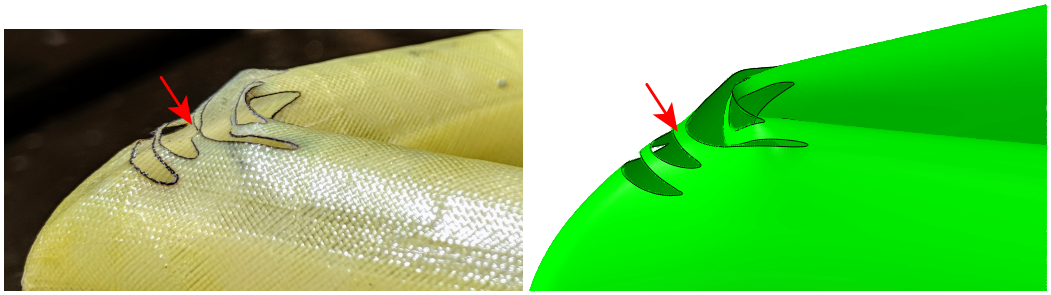

(a) (b)

Figure 3.13: Deformed shape of the shell near the cutout (a) experiment, (b) simulation.

Figure 3.13 shows the deformed shape of the shell near the cutout. While the actual deformed shape and the finite element simulation are quite similar, thus further validating the numerical simulation, some differences can be noted. For example, the strips of material between the cutouts develop an inward buckled shape in the experiment, while in the simulation they bend uniformly. This is most visible in the center strip, as pointed by red arrows in Fig. 3.13a-3.13b, and it occurs because

of a slight shape imperfection of the mold used to build the shell, which creates a localized, concave bend at corner.

3.8 Shape Optimization of Single Cutout

Finite element simulations, discussed in section 3.4, showed that stress tends to concentrate at the corner of the thin shell. Using this information we can reduce the problem to studying the shape of a single cutout. A contour was defined on a projection plane, tangent to the side of the shell, using control points and a spline fit between all the points. The projection plane provides a convenient Cartesian coordinate system to describe the control points. The contour was then projected onto the shell. The coordinates of each control point, x_i, on the projection plane were chosen as design variables of the minimization problem. A visualization of the design space is provided in Fig. 3.14.

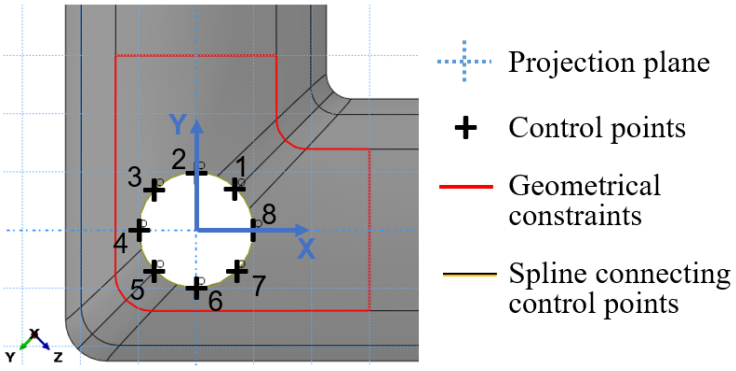

Figure 3.14: Description of design space for shape optimization of a single cutout.

The geometrical constraints in Eq. (3.1) were initially defined so that the control points remain within the red contour, Fig. 3.14, corresponding to the cutout in Fig. 3.8, which allowed the shell to fold without any damage. Constraining the control points to fit within this contour not only ensures that the cutout will remain within the physical boundaries of the shell, but it also limits the design space to shapes that have a smaller area than the one found in Fig. 3.8, thus improving the possibility of finding solutions with higher bending stiffness in the deployed configuration.

Since the control points can be placed anywhere within the red contour, and the position of each point is independent of the others, two issues emerge when imposing geometrical constraints. First, the red contour is non-convex, hence the spline connecting the control points can escape the contour, while the points remain inside. For example, if control points 1 and 8 in Fig. 3.14 were positioned respectively at the top-right and middle-right corners of the contour, the spline connecting those two

points would not follow the L-shape, thus remaining within the contour, but would cut across the L-shape and fall outside the contour. To prevent this, the control points were originally defined on a square domain, Fig. 3.15a, with Cartesian coordinates x_p and y_p, and then transformed to an L-shaped domain, Fig. 3.15b, via a mapping, with Cartesian coordinates x and y.

Another issue was preventing the spline from intersecting itself. The issue was resolved by constraining each control point to remain within its own sub-domain of the square domain, displayed with dotted lines in Fig. 3.15a. This approach limits the design space but does not prevent the chosen algorithm from finding a solution to the optimization problem, as described in section 3.8.2.

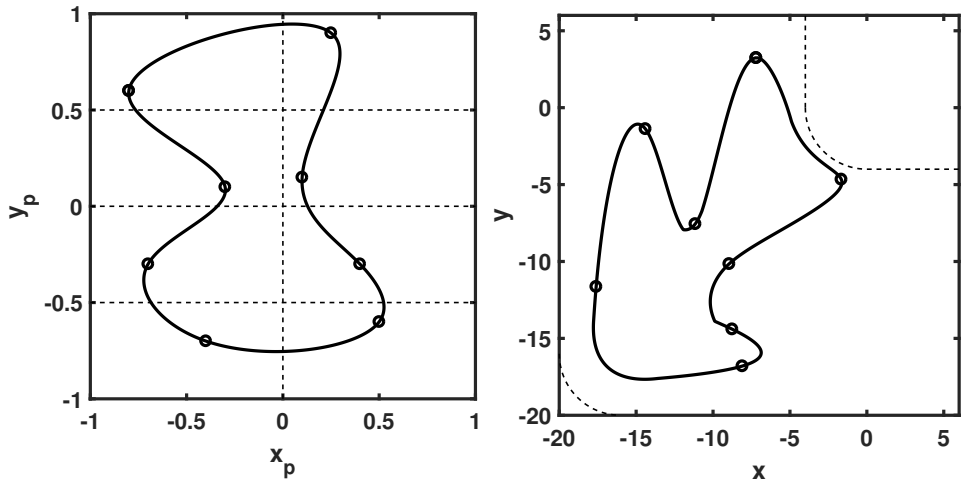

(a) (b)

Figure 3.15: Geometrical constraints for shape optimization problem (a) control points and spline defined on a square domain, (b) control points and spline mapped to and L-shaped domain.

3.8.1 Mesh Convergence Studies

The objective function in Eq. (3.1) and the associated constraint on the maximum failure index were studied using different mesh sizes for the finite element formulation. The resulting trends are shown in Fig. 3.16. Starting from the initial guess in Fig. 3.16a, a circular cutout whose contour is described by 8 control points, connected by a spline, one coordinate of a single control point was modified incrementally to achieve the final configuration in Fig. 3.16b. This corresponds to varying only one design variable x_i of the minimization problem in Eq. (3.1), while the other variables are kept constant. The results from this study are plotted in Figs. 3.16c and 3.16d for four mesh sizes. Each data point was obtained by running a

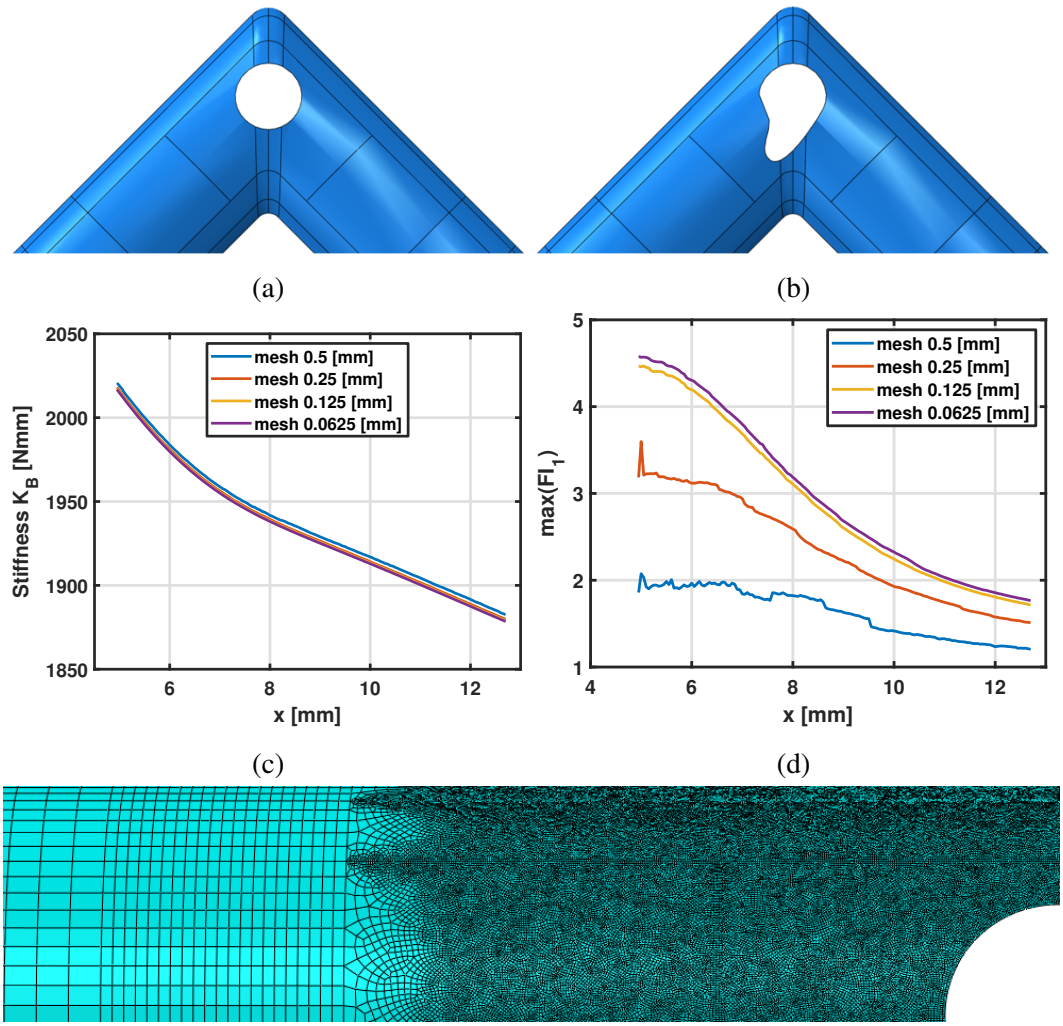

Figure 3.16: Mesh convergence studies (a) initial guess, (b) final shape of cutout after modifying one coordinate of a single control point (one design variable, here named x), (c) objective function plotted against the design variable x for different mesh sizes, (d) maximum value of the first failure index plotted against the design variable x for different mesh sizes, and (e) an example of S4R shell elements mesh distribution.

geometrically nonlinear finite element simulation of the folding process.

An example mesh size of 0.125 mm is shown in Fig. 3.16e. The mesh size near the cutout has been decreased by adding extra nodes. The size of the elements far away from the cutout is determined by the largest distance allowed between consecutive nodes such that a smooth transition region between larger and smaller elements can be generated. Finally, the aspect ratio of each element was set to be no larger than 3. The trend studies show that the bending stiffness is almost completely insensitive to

mesh size variations, for a mesh size smaller that 0.5 mm near a cutout, indicating mesh convergence; while the maximum value of the first failure index reaches mesh convergence only for a mesh size of 0.125 mm near a cutout, displayed by yellow and purple curves in Fig. 3.16d.

After completing these initial studies, a minimization was performed with Constrained Optimization BY Linear Approximation (COBYLA) (Powell, 1994), an optimization algorithm for constrained problems that does not utilize gradient information. During an iteration, a linear approximation of the objective function is solved to obtain a candidate for the optimal solution. The candidate solution is evaluated using the original objective and constraint functions, yielding a new data point in the optimization space. This information is used to improve the linear approximation for the next iteration of the algorithm. When the solution cannot be improved anymore, the step size is reduced, refining the search. When the step size becomes sufficiently small, the algorithm stops.

The COBYLA algorithm is publicly available in Python libraries (Perez, Jansen, and Martins, 2012) and it was incorporated within the shape optimization method described here. A Python script generates an input file for Abaqus 2017, with a chosen cutout shape for the shell, defined by a set of specific values for the design variables. A finite element analysis of the prescribed shell design is then carried out with Abaqus and the values of first failure index and overall bending stiffness are returned. The Python script evaluates the objective function and calls the COBYLA algorithm to update the design variables. Each set of design variables defines a new cutout shape, and therefore a new shell design. The optimization iteration is run until the convergence criterion is satisfied:

$$|K_B^i - K_B^{i-1}| \leq 10^{-6} \tag{3.5}$$

where K_B is the objective function in Eq. 3.1, corresponding to the bending stiffness of the shell in the deployed configuration, and i is the current iteration counter.

3.8.2 Results from Shape Optimization

The optimized shape of the cutout and the bending stiffness at each iteration of the optimization study are shown in Fig. 3.17. The contour plot of the first failure index in Fig. 3.17a shows that the cutout generated with shape optimization successfully prevents the shell from being damaged. In fact, every element of the finite element discretization of the shell has a value of the first failure index less than 1.

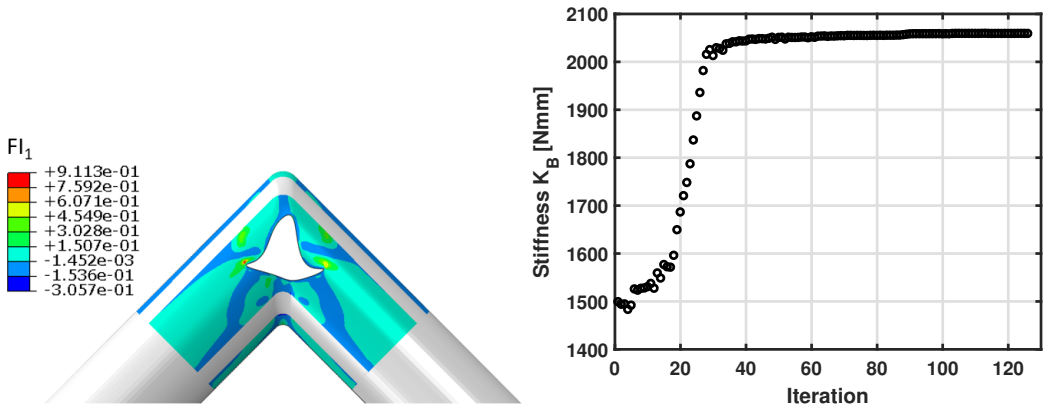

(a) (b)

Figure 3.17: Shape optimization of a single cutout (a) contour plot of FI_1 on shell folded 45°. FI_1 has been mapped onto a deployed shell, (b) objective function plotted at each iteration of the optimization study.

A particular drawback of this method is that it can require a significant number of design variables; in this case, 8 control points and therefore 16 design variables. If two cutouts were considered, instead of one, the number of design variables would be more than doubled (considering the position of the two cutouts as additional degrees of freedom for the optimization problem). Hence, if the number of cutouts under consideration increases, the optimization problem becomes computationally more expensive.

3.9 Summary and Comparison of Results

Different designs for thin shells with cutouts have been obtained via physical intuition, topology optimization using level-set functions, and shape optimization. A comparison of the deployed bending stiffness of the shells and the maximum value of the first failure index for all the designs discussed in this chapter is provided in Table 3.1 and shown in Fig. 3.18. The shaded region in the plot marks the region of design with a safe value of the failure index. The most desirable design would lie near the upper left corner of the plot, thus providing high bending stiffness and preventing damage of the shell. Unfortunately, when the bending stiffness of the deployed shell increases, the shell is also more likely to be damaged when folded and vice versa.

The bending stiffness and the maximum failure index for a shell without cutouts, A_1, are provided as baseline. Placing circular cutouts in areas of localized stress, A_2, might appear to be a suitable, intuitive solution, instead it decreases the bending

Table 3.1: Summary of the deployed bending stiffness and the maximum value of the first failure index for shell designs studied in the chapter. The corresponding shell designs are shown in Fig. 3.18.

	Name	max(FI_1)	Stiffness [Nm]
Intuitive	A_1	7.06	5.33
	A_2	4.47	2.02
	A_3	8.64	1.79
	A_4	10.35	1.53
	A_5	0.99	1.05
Optimized	B_1	0.95	2.06
	B_2	0.85	2.08
	B_3	0.98	1.90
	B_4	0.53	1.44

stiffness to less than half the initial value without preventing damage of the shell. Two results obtained using physical intuition, A_3 and A_4, have bending stiffness lower than 2000 Nmm and maximum first failure index higher than 8. This is partially due to the fact that these designs have sharp corners, which lead to higher stress concentrations. The first successful, intuitive design, A_5, adopts smooth corners and much larger cutouts. This solution satisfies the failure constraint but suffers a substantial penalty in bending stiffness.

Shape optimization studies produced a new design, B_1, which concurrently satisfies the failure constraint and maximizes the overall bending stiffness of the deployed shell, using only one cutout on each side of the shell. Finally, three resulting designs from topology optimization using level-set functions are also plotted. Amongst these, B_2 is the most promising, since it provides the highest bending stiffness while keeping the maximum failure index below 1. In fact, a physical shell with this design was tested (section 3.7.3) and showed no signs of damage.

3.10 Conclusion

This chapter presented methods to place cutouts on thin shells forming a 90° corner and made entirely of fiber reinforced composite material, so that they can fold without being damaged, while also maximizing the deployed stiffness.

Designs obtained using physical intuition were shown and a first shape of cutout that satisfies the failure constraint was found. Since the cutout removed a large area of the shell, the deployed bending stiffness was greatly reduced. Hence, optimization

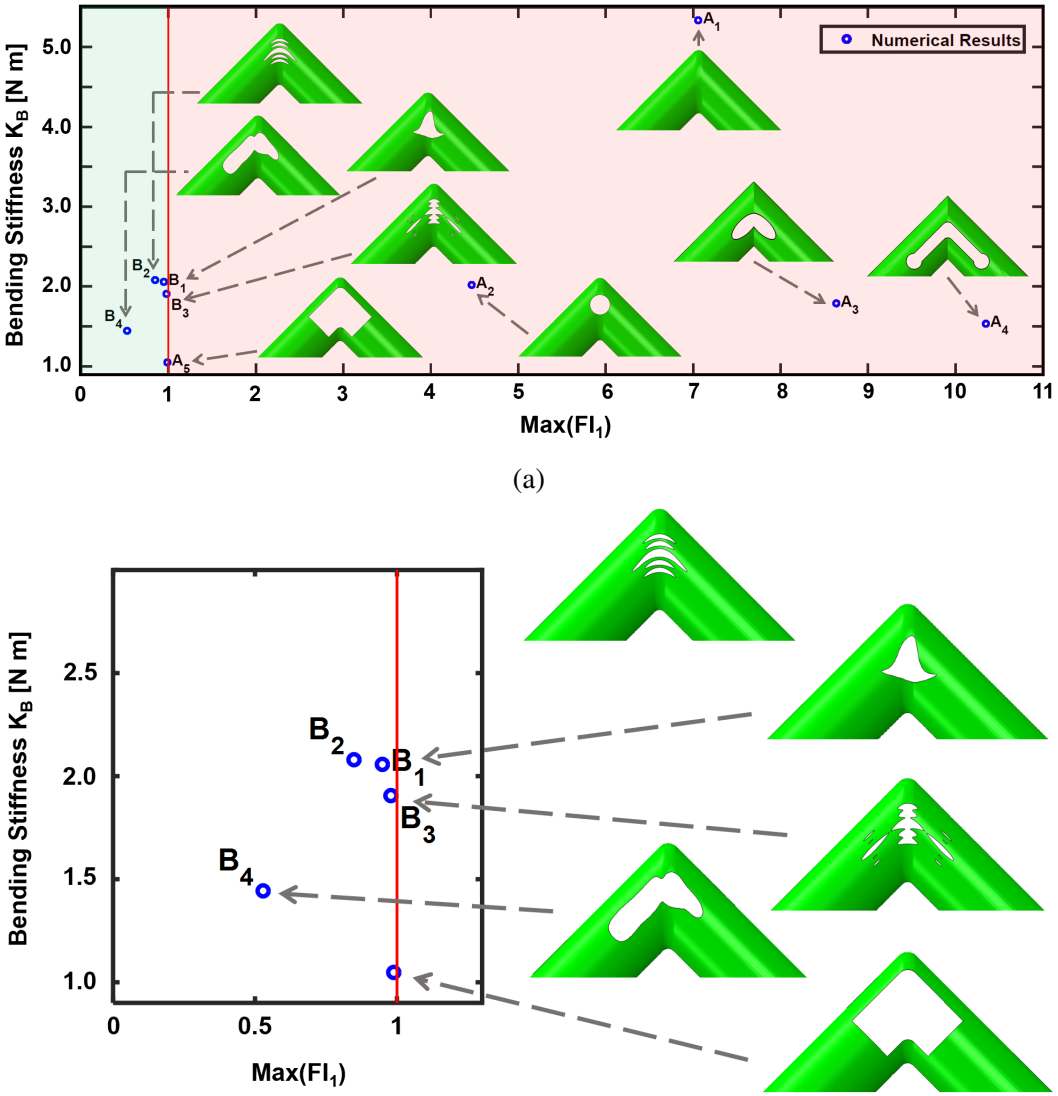

(a)

(b)

Figure 3.18: Deployed bending stiffness plotted against max (FI_1) for shell designs studied in the chapter (a) all shell designs, (b) only shell designs that satisfy failure criterion.

studies to improve this result were carried out.

First, a novel topology optimization method that uses level-set functions was proposed. The only assumptions made are on the type of functions to be used. Although these assumptions restricted the design space, the results of this study show unique solutions to the concurrent optimization problem of composite, thin-shell structures with complex shapes and geometrical nonlinearities. A considerable advantage of the level-set method presented here is a reduction in the number of design variables

for a broad design space (e.g. multiple cutouts), if compared to the density-based approach discussed in chapter 2.

Second, a shape optimization method that uses a spline representation of the contour of a single cutout was presented. This method relied on prior knowledge of the mechanics of deformation of the shell, thus starting from an initial guess with a cutout placed in a convenient location to remove areas with stress concentration. The scope of the method was not to find an optimal number or location of cutouts on the shell, but to optimize the shape of a single cutout.

Finally, thin shells forming a corner were built and tested, and the experiments achieved good agreement with the numerical prediction.

Having demonstrated the design capabilities of both optimization methods, a few aspects could be addressed in future work. First, a perfect geometry of the shell was used to carry out numerical simulations. This assumption neglects randomly distributed manufacturing imperfections, thus resulting in minor deviations of numerical prediction from experimental results.

Second, only shells in bending were considered and therefore the cutouts obtained are optimized for specific load conditions. Perhaps, different load conditions, such as twisting or combined bending and twisting, could be considered to obtain different cutouts.

Finally, further studies are needed to understand whether localized damage occurs on the shell during experiments. Some results from this study show cutouts positioned very close to each other, thus forming this strips of material. These may behave differently than the rest of the shell, due to size effects. Chapter 4 investigates size-scaling effects of thin, plain weave composites applied to self-deployable shells, as well as localized damage detection in the experiments.

Chapter 4

SIZE-SCALING EFFECTS ON SOFTENING AND FAILURE OF PLAIN-WEAVE ASTROQUARTZ ® LAMINATES AND LOCALIZED DAMAGE MEASUREMENT

4.1 Introduction

The results from the optimization studies on thin shells forming a corner, discussed in chapter 3, provided successful designs of thin shells that can fold 45° without being damaged, while maximizing the deployed bending stiffness. The design with highest stiffness is shown again in Fig. 4.1. The cutouts are positioned very close to each other leaving thin strips of plain-weave composite material. Since stress concentrates near the cutouts when the shell is folded, the structural behavior of these thin strips was studied.

This chapter presents results on size-scaling effects on stiffness and strength of thin, plain-weave Astroquartz ® laminates. While a wealth of literature exists on size-scaling effects on brittle materials, including unidirectional fiber reinforced composites, there is no experimental data on thin, plain-weave composite material. The laminates studied here, discussed in chapter 3, are: two-ply $[45_{pw}]_2$, three-ply $[45_{pw}/0_{pw}/45_{pw}]$, four-ply $[45_{pw}]_4$, and six-ply $[45_{pw}/45_{pw}/0_{pw}]_s$.

The experiments focused on thin samples with widths ranging from 15 mm to 1 mm. Studies on unidirectional composites, discussed in the next section, focus on size effects on larger scales. Hence, the results presented in this chapter provide the first collection of experimental data on size-scaling effects on thin and small plain-weave samples. Additionally, results showing measurement of localized damage in experiments are presented.

4.2 Background and Layout of the Chapter

The effect of structural size on stiffness and strength has been the scaling problem of main interest in solid mechanics since the 1500s (Bažant and Chen, 1999). More recently, composite materials have led to advancements in military, commercial, and space applications because of their high specific strength and stiffness, combined with light weight, increasing the importance of understanding size-scaling effects on different types of composite materials. Both a statistical approach based on Weibull

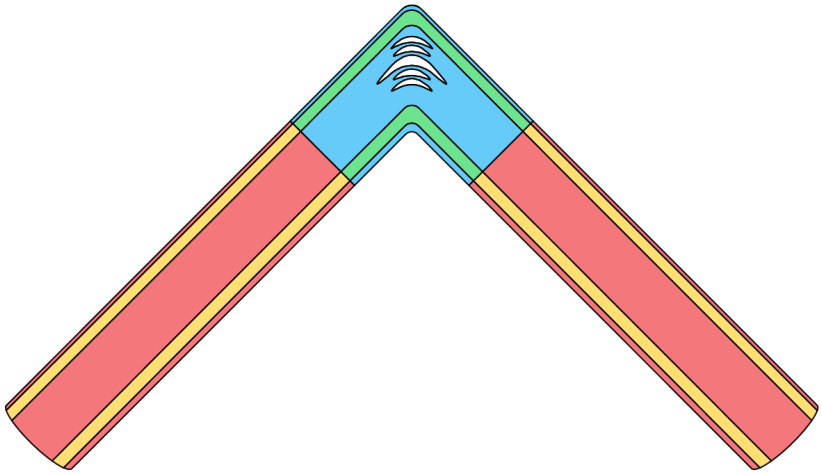

Figure 4.1: Thin shell forming a corner with optimized shape of cutouts and different layups: blue, 2 plies; red, 3 plies; green, 4 plies; yellow, 6 plies.

distributions (Weibull, 1939; Bullock, 1974; A. S. D. Wang, Tung, and Sanders, 1980; Zweben, 1981; Wisnom, 1991) and a fracture mechanics model (Atkins and Caddell, 1974; Carpinteri and Bocca, 1987; Bažant, J. J. H. Kim, et al., 1999) have been used to analyze scale effects on the strength of fiber-reinforced composite materials. A comprehensive review of both statistical and deterministic size effects is provided by Bažant and J. L. Le (2017).

The application of the statistical approach for modeling size-scaling effects on the strength of brittle materials is based on the probabilistic assumption that larger specimens will inherently exhibit a higher number of imperfections, causing a reduction in nominal strength. A concise formulation of this theory was proposed by Bullock (1974):

$$\frac{\sigma_m^c}{\sigma_p^c} = \left(\frac{V_p}{V_m}\right)^{\frac{1}{\beta}} \tag{4.1}$$

where the subscripts m and p refer to "model", as in laboratory scale, and "prototype", as in full-scale, respectively; σ^c is the ultimate stress; V is the volume of the sample; β is a parameter that provides a measure of the scatter in the strength data.

A simple fracture mechanics model provided by Atkins and Caddell (1974) describes the size-strength relationship for notched, brittle, and isotropic materials:

$$\sigma_p^c = \frac{\sigma_m^c}{\sqrt{\lambda}} \tag{4.2}$$

where λ is a geometric scaling parameter, defined as the ratio of the model length to the prototype length.

Jackson, Kellas, and Morton (1992) compare the statistical approach and the fracture mechanics model to experimental results obtained from testing different graphite-epoxy laminates in both tension and flexure. A plot from Jackson, Kellas, and Morton (1992) is shown in Fig. 4.2. The laminates used in the experiments were manufactured from unidirectional plies, in different stacking sequences, chosen to highlight individual and interacting failure modes. For example, Fig. 4.2 shows experimental results from cross-ply laminates, $[+45_n/-45_n/+45_n/-45_n]_s$, where the subscript n indicates the number of plies used in one orientation, tested under flexural loading. The smallest samples were 12.7 mm wide and made of 8 plies (n = 1) of AS4/3502 graphite-epoxy.

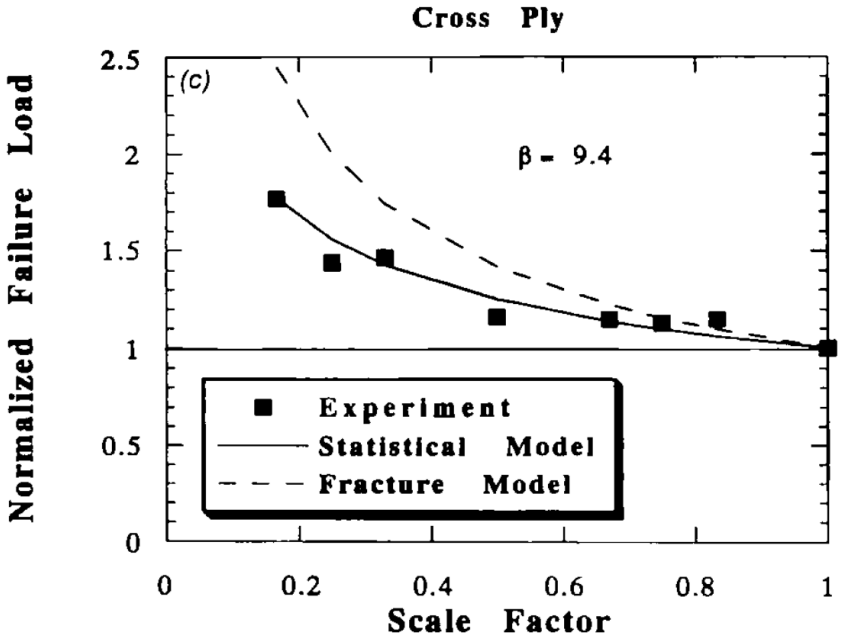

Figure 4.2: Plot from Jackson, Kellas, and Morton (1992) showing a comparison of normalized failure load versus scale factor with statistical and fracture mechanics based analytical models for graphite-epoxy, cross-ply samples from 50.8 mm wide and 32 plies (Scale Factor = 1) to 12.7 mm wide and 8 plies (Scale factor = 0.19), tested under flexural loading.

Generally, both theoretical and experimental studies on size-scaling effects on strength of brittle materials, including fiber-reinforced composites (Weibull, 1939; Bullock, 1974; Jackson, Kellas, and Morton, 1992; Bažant and Chen, 1999), predict an increase in strength for smaller scales. Another example is shown in Fig. 4.3

from Bažant (2019), which plots the evolution of structural strength probability distribution with increasing structure size, D.

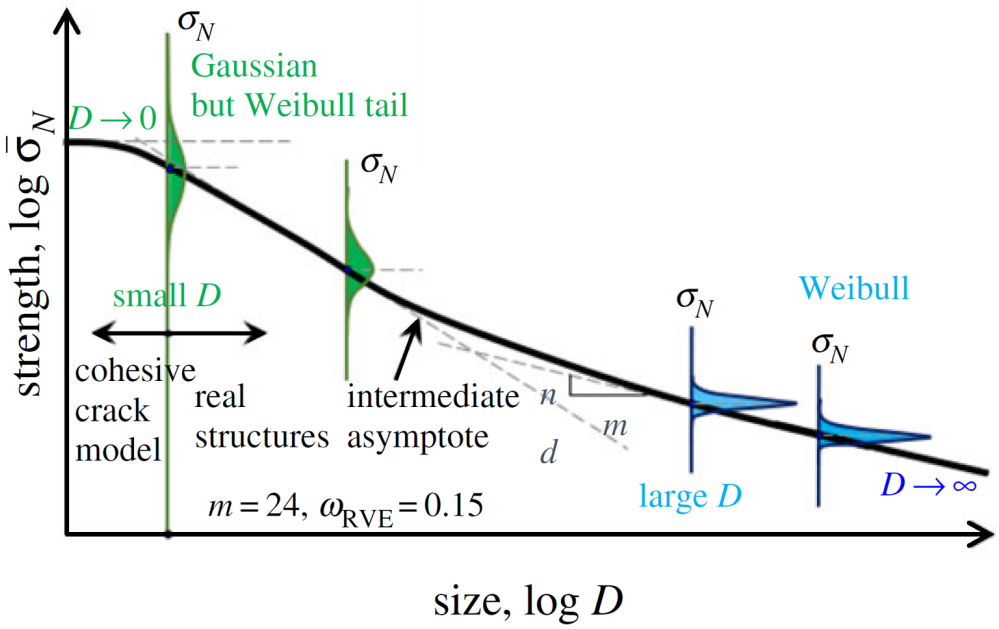

Figure 4.3: Plot from Bažant (2019) showing size-scaling effects on structural strength of quasibrittle structures.

While experimental data provided in the literature focuses on larger scales, as seen in Fig 4.2, thin samples at smaller scale are of interest because cutouts are often placed on thin, composite structures to fulfill different purposes. Amongst those are tape-spring hinges, traditionally incorporated within straight tubes (Mobrem and Adams, 2009b; Mallikarachchi and Pellegrino, 2011). When there are multiple cutouts next to each other, small regions of material can form. Often, these regions must withstand high localized strain.

Figure 4.4 shows a contour plot of the in-plane strain component ϵ_{11}, on a thin shell folded 45°. When folding a high-strain, composite structure, strain can localize in very small regions around the hinges (Mallikarachchi and Pellegrino, 2010), thus causing the material to fail and cracks to form and propagate. Similarly, the shell forming a corner studied in chapter 3 shows localized high strain along the small strips of material separated by cutouts. The width of these strips of material ranges from 3 mm to 1 mm. The part with highest strain, red contour in Fig. 4.4, concentrates in an area measuring less than 0.2 mm^2.

The following sections provide details on the numerical and experimental character-

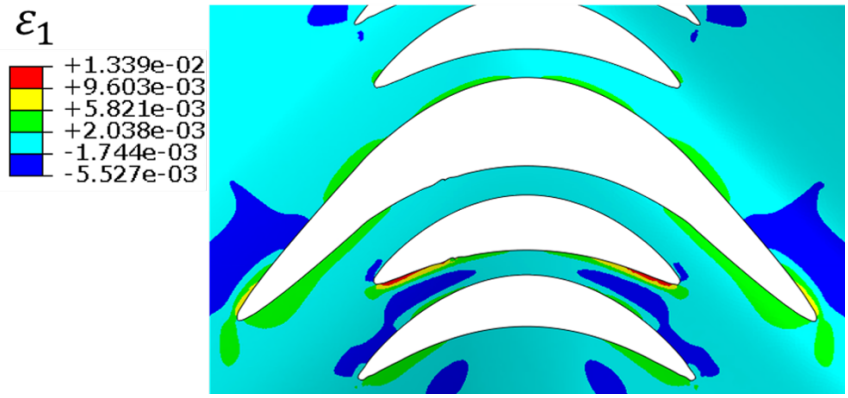

Figure 4.4: Contour plot of in-plane, axial strain ϵ_1 on a shell folded 45°. ϵ_1 has been mapped onto a deployed shell. The strain is localized in small areas near the cutouts.

ization of the stiffness and strength of ultra-thin, plain-weave laminates at different scales. First, laminate stiffness and strength will be measured at macro-scale. Experiments on samples that are either 12.7 mm or 15 mm wide will be discussed. Second, size-scaling effects will be addressed and the results from experiments conducted on samples that are less than 15 mm wide will be presented. Third, a self-deployable shell forming a corner will be used to demonstrate how size-scaling effects, introduced in numerical simulations, influence the results of failure analysis. Finally, localized damage on the shell will be experimentally measured via computed tomography scans and digital volume correlation techniques. A study of measurement noise from computed tomography and digital volume correlation will also be presented and procedures to reduce the baseline noise will be addressed.

4.3 Laminate Stiffness and Strength Parameters at Macro-Scale

A linear elastic model of plain-weave, Astroquartz ® laminates was built using Classical Lamination Theory (CLT) (Daniel and Ishai, 1994), micromechanical models for bending behavior of woven composites (Soykasap, 2006), and experimental results. CLT assumes material linearity and is used to predict the mid-plane strains and out-of-plane curvature changes of a laminate under load. Given a laminate consisting of n plies, the 6×6 $\boldsymbol{ABD}$ stiffness matrix relates the stress resultants, forces and moments $\boldsymbol{N}$ and $\boldsymbol{M}$, to the mid-plane strains and out-of-plane curvatures, $\boldsymbol{\epsilon}$ and $\boldsymbol{\kappa}$, respectively,

$$\begin{bmatrix} N \\ M \end{bmatrix} = \begin{bmatrix} A & B \\ B & D \end{bmatrix} \begin{bmatrix} \epsilon \\ \kappa \end{bmatrix} \tag{4.3}$$

Since all the laminates under study ($[45_{pw}]_2$, $[45_{pw}/0_{pw}/45_{pw}]$, $[45_{pw}]_4$, and $[45_{pw}/45_{pw}/0_{pw}]_s$) are symmetric, the $\boldsymbol{B}$ matrix is null. The material used is plain-weave 525 Astroquartz ® II fabric (quartz fiber), from JPS Composite Materials (JPS, 2017), pre-impregnated with PMT-F6 cyanate ester resin, from PATZ Materials & Technologies (PATZ, 2019). Its material properties collected from technical data sheets (JPS, 2017; PATZ, 2019) are listed in Table 4.1.

Table 4.1: Astroquartz ® fiber and cyanate ester matrix properties collected from technical data sheets.

Fiber	
V_f	0.62
$E_{1f} = E_{2f}$	72 (GPa)
ν_{12f}	0.16
G_{12f}	31 (GPa)
$thickness_f$	80 (μm)
Matrix	
E_m	3.64 (GPa)
ν_m	0.35
G_m	1.35 (GPa)

Both the in-plane shear modulus of plain-weave fibers, G_{12f}, and the shear modulus of cyanate ester matrix, G_m, are calculated using the isotropic relation:

$$G = \frac{E}{2(1+\nu)} \tag{4.4}$$

Following the procedure described in Soykasap (2006), the longitudinal modulus and major Poisson's ratio of each yarn are calculated using the rule of mixtures (Daniel and Ishai, 1994):

$$E_1^y = V_f E_{1f} + (1 - V_f) E_m \tag{4.5}$$

$$\nu_{12}^y = V_f \nu_{12f} + (1 - V_f) \nu_m \tag{4.6}$$

The transverse modulus and the in-plane shear modulus are obtained from the Halpin-Tsai semiempirical relations (Haplin and Tsai, 1969) as follows:

$$E_2^y = \frac{E_m(1 + \xi\eta_E V_f)}{1 - \eta_E V_f} \tag{4.7}$$

$$G_{12}^y = \frac{G_m(1 + \xi\eta_G V_f)}{1 - \eta_G V_f} \tag{4.8}$$

with:

$$\eta_E = \frac{E_{2f} - E_m}{E_{2f} + \xi E_m} \tag{4.9}$$

$$\eta_G = \frac{G_{12f} - G_m}{G_{12f} + \xi G_m} \tag{4.10}$$

The parameter ξ is a curve-fitting parameter, which experimentally falls within the values $1 < \xi < 2$. This study assumes a value of $\xi = 1$, usually used for laminates with high fiber volume ratios. Finally, the minor Poisson's ratio of the yarn is calculated from reciprocity relationship:

$$\nu_{21}^y = \nu_{12}^y \frac{E_2^y}{E_1^y} \tag{4.11}$$

The thickness of each yarn is assumed to be half the thickness of a single plain-weave lamina. Hence, to estimate the homogenized material properties of a woven lamina one can simply use the rule of mixtures, assuming that half the fibers are in the longitudinal direction while the other half are in the transverse direction. For example, the longitudinal modulus of a lamina is calculated as:

$$E_1 = E_2 = 0.5V_f E_{1f} + (1 - V_f)E_m \tag{4.12}$$

Table 4.2 lists the measured thickness of each pre-impregnated laminate, cured in autoclave on a flat mandrel.

Using the material properties described above, the mosaic model (Soykasap, 2006) provides an accurate estimate of the $\boldsymbol{A}$ matrix for each of the four laminates. For example, the results obtained for the thinnest laminate, $[45_{pw}]_2$, are shown in Eq. 4.13.

Table 4.2: Thickness of pre-impregnated laminates, cured in autoclave on a flat mandrel.

Laminates Thickness in μm	
1 ply	90
2 plies	160
3 plies	230
4 plies	280
6 plies	390

$$\boldsymbol{A}_{[45_{pw}]_2} = \begin{bmatrix} 3403.2 & 1872.0 & 0 \\ 1872.0 & 3403.2 & 0 \\ 0 & 0 & 2150.3 \end{bmatrix} (N/mm) \tag{4.13}$$

A correction to the bending stiffness matrix, $\boldsymbol{D}$, was applied as a result of four-point bending experiments, shown in Fig. 4.5. The experiments measured the terms $D_{11} = D_{22}$ and found that the micromechanical models over-predict these terms for ultra-thin composites. The samples tested are 12.7 mm wide and loaded with a four-point bending fixture. The distance between the loading noses, namely the load span, is one half of the support span, as per ASTM Standard (Standard D6272-02, 2008). Results from the experiments are summarized in Table 4.3.

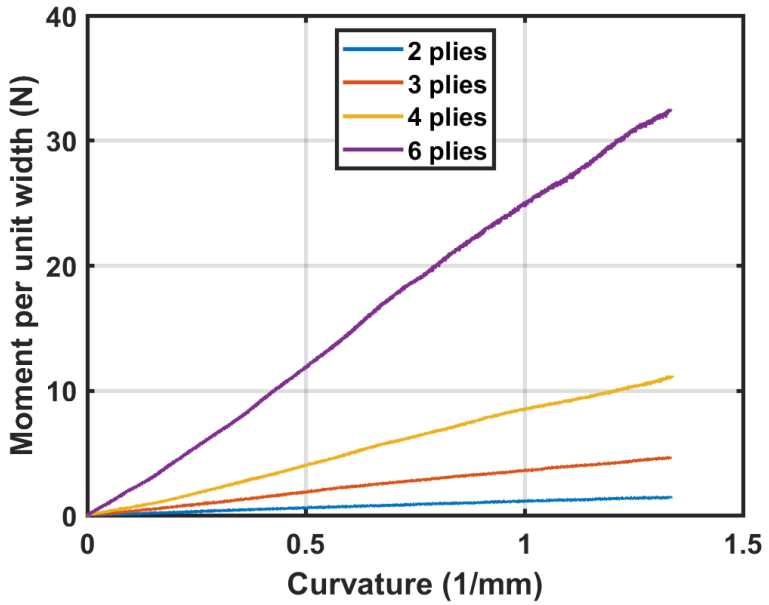

Figure 4.5: Typical bending response from four-point bending experiments.

Table 4.3: D_{11} component of matrix **D** in Nmm.

Laminate Layup	Average Value	Samples Tested	Population SD
$[45_{pw}]_2$	3.1	3	0.26
$[45_{pw}/0_{pw}/45_{pw}]$	10.0	5	0.34
$[45_{pw}]_4$	23.0	5	1.10
$[45_{pw}/45_{pw}/0_{pw}]_s$	69.8	5	1.30

Using the experimental results, correction factors were calculated for each layup, from Eq. (4.14), and applied to every term of the $\boldsymbol{D}$ matrix, while matrices $\boldsymbol{A}$ and $\boldsymbol{B}$ were left unchanged. Table 4.4 shows the correction factors for each layup. As expected, the gap between the prediction made with micromechanical models and experimental results decreases as the number of plies, and thus the thickness of the layup, increases. It must be clarified that this correction has no relation with size-scaling effects. In fact, it is mostly due to a mismatch between the geometry assumed by the mosaic model (Soykasap, 2006), which neglects the undulation in the yarns and introduces discontinuities in the fibers, and the real, three-dimensional geometry of plain-weave laminates.

$$Correction\,Factor\,(C.F.) = \frac{D_{11_{calculated}}}{D_{11_{measured}}} \tag{4.14}$$

Table 4.4: Correction factors for matrix $\boldsymbol{D}$ of thin, plain-weave laminates.

Laminate	$C.F.$
$[45_{pw}]_2$	2.34
$[45_{pw}/0_{pw}/45_{pw}]$	2.19
$[45_{pw}]_4$	1.69
$[45_{pw}/45_{pw}/0_{pw}]_s$	1.53

Finally, new $\boldsymbol{D}$ matrices were calculated for the laminates under study. An example of $\boldsymbol{D}$ matrix for the two-ply laminate, $[45_{pw}]_2$, is:

$$\boldsymbol{D}_{[\boldsymbol{45_{pw}}]_2} = \begin{bmatrix} 3.10 & 1.71 & 0 \\ 1.71 & 3.10 & 0 \\ 0 & 0 & 1.96 \end{bmatrix} (Nmm) \tag{4.15}$$

Failure predictions for a folded shell forming a corner were made using a laminate failure criterion (Mallikarachchi and Pellegrino, 2013) for ultra-thin, plain-weave composites. The criterion applies to layups with same orientation plies and uses three non-dimensional failure indices to capture in-plane, bending, and coupled in-plane and bending failure, defined as follows:

$$FI_1 = f_1(N_x + N_y) + f_{11}(N_x^2 + N_y^2) + f_{12}N_xN_y + f_{33}N_{xy}^2 < 1 \tag{4.16}$$

$$FI_2 = f_{44} \times max(M_x^2, M_y^2) + f_{66}M_{xy}^2 < 1 \tag{4.17}$$

$$FI_3 = max\left(\frac{N_x}{F_x}, \frac{N_y}{F_y}\right) + \frac{max(|M_x|, |M_y|)}{F_4} < 1 \tag{4.18}$$

The failure coefficients, f_i and f_{ij}, are a combination of physical strength parameters that must be measured or calculated. Tables 4.5 and 4.6 show the resulting strength parameters for two-ply and four-ply laminates.

Table 4.5: Material strength parameters for two-ply laminates of Astroquartz ® fiber and cyanate ester resin.

Strength Parameter	Average Value	Samples Tested	Population SD
$F_{1t} = F_{2t}$ [N/m]	76.16	5	2.83
$F_{1c} = F_{2c}$ [N/mm]	34.50	-	-
F_3 [N/mm]	14.55	5	0.12
F_4 [N]	3.26	4	0.28
F_6 [N]	1.10	4	0.06

For both tensile and compressive strengths the subscripts 1 and 2 refer to the directions parallel and perpendicular to the fibers respectively. Hence, for plain-weave material $F_{1t} = F_{2t}$ and $F_{1c} = F_{2c}$. The tensile strength was measured as the smallest failure value obtained from tensile tests of plain-weave $[0_{pw}]_2$ and $[0_{pw}]_4$ laminates. 15 mm wide test samples were pulled under tension at a rate of 2 mm/min until failure, according to ASTM Standard (Standard D3039/D3039M, 2009). The compressive strength was calculated using elasto-plastic fiber microbuckling theory by Fleck and Budiansky (1991), where γ_y is derived from shear strength experiments. The equations used are the following:

Table 4.6: Material strength parameters for four-ply laminates of Astroquartz ® fiber and cyanate ester resin.

Strength Parameter	Average Value	Samples Tested	Population SD
$F_{1t} = F_{2t}$ [N/mm]	150.00	4	1.47
$F_{1c} = F_{2c}$ [N/mm]	65.69	-	-
F_3 [N/mm]	30.88	5	0.21
F_4 [N]	8.78	4	1.28
F_6 [N]	3.65	4	0.10

$$F1_c = \frac{G}{1 + \frac{\phi_0}{\gamma_y}} \tag{4.19}$$

$$\gamma_y = \frac{\tau_y}{G} \tag{4.20}$$

$$G = \frac{G_m(G_{12f} + G_m + V_f(G_{12f} - G_m))}{G_{12f+G_m-V_f(G_{12f}-G_m)}} \tag{4.21}$$

where G is the shear modulus of the composite laminate, ϕ_0 is the fiber misalignment angle, and γ_y and τ_y are in-plane yield shear strain and stress respectively. The fiber misalignment angle was measured from micrographs of samples with one, two, and four plain-weave plies, shown in Fig. 4.6.

The in-plane shear strength, F_3, was measured as the smallest failure value obtained from tensile tests of plain-weave $[45_{pw}]_2$ and $[45_{pw}]_4$ laminates, divided by 2 because:

$$N_{xy} = \cos\alpha \sin\alpha N_{x'} = \frac{1}{2} N_{x'} \tag{4.22}$$

where where x' and y' are loading directions, x and y are fiber directions, and $\alpha = 45°$ is the fiber orientation angle. The test samples are 15 mm wide and were pulled under tension at a rate of 2 mm/min until failure, according to ASTM Standard (Standard D3518/D3518M, 2007).

A typical shear response, obtained by applying the transformation in Eq. 4.22 to the measurements obtained from the experiments, is shown in Fig. 4.7. The plot shows a first region where the shear stress increases with strain with a higher slope.

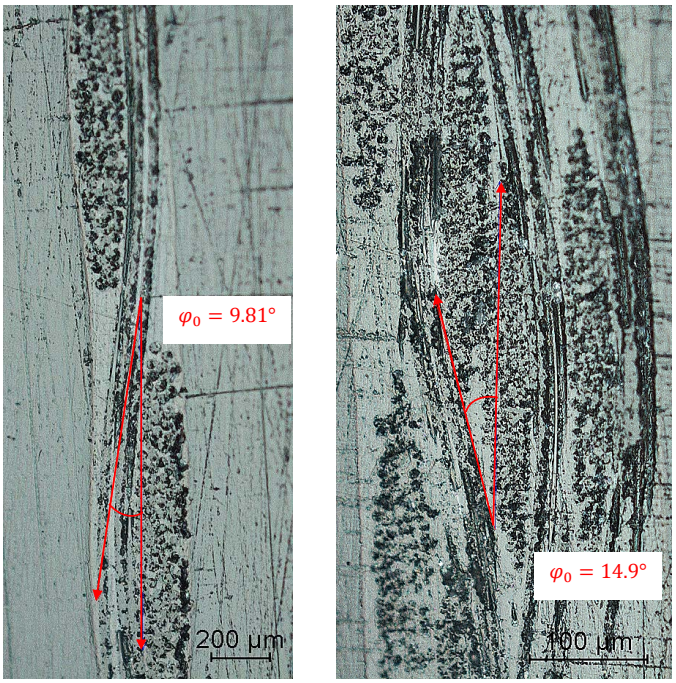

Figure 4.6: Micrographs of one and four-ply laminates showing measurements of fiber misalignment angle, ϕ_0.

Then, there is a second region with a much lower slope. Finally, the slope increases again until failure. This behaviour is characteristic of a toughened interface system (Nguyen et al., 2019). The lower slope in the second region is associated with matrix shear cracks between fibers and the length of this region depends on the evolution of macro-cracking, finally reaching a saturated state.

Usually, an untoughened composite should exhibit stiffness degradation due to micro-crack accumulation, leading to failure due to delamination. Hence, the composite under study behaves as a toughened interface system, which exhibits intralaminar micro-cracking and macro-cracking, thus delaying the onset of delamination and prolonging the ultimate failure. This behavior could be explained by the three-dimensional pattern of the plain-weave, which acts as the particles that are dispersed within resin rich regions of toughened interface systems.

The bending strength, F_4, was measured as the smallest failure value obtained from platen bending tests (Mallikarachchi and Pellegrino, 2013; Yee and Pellegrino, 2005; T. W. Murphey et al., 2015) of plain-weave $[0_{pw}]_2$ and $[0_{pw}]_4$ laminates. Finally, the twisting strength, F_6, was measured as the smallest failure value obtained from platen bending tests of plain-weave $[45_{pw}]_2$ and $[45_{pw}]_4$ laminates, divided by 2 because:

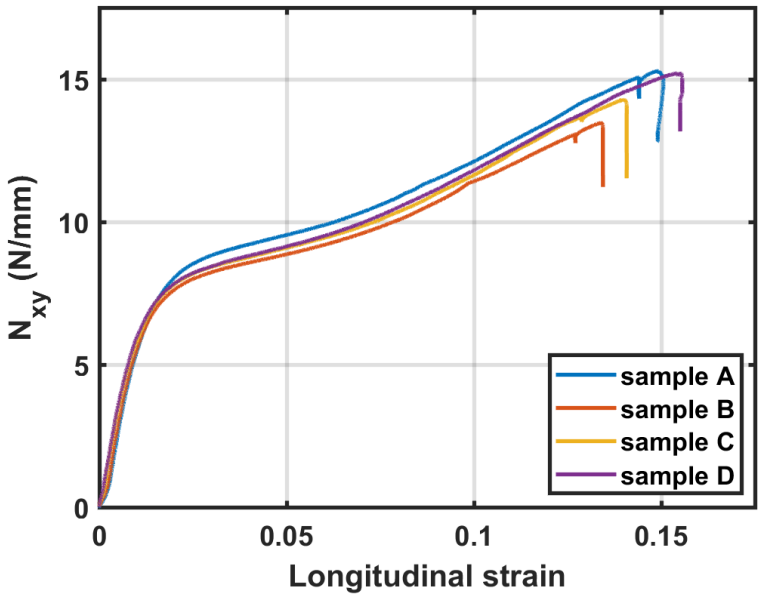

Figure 4.7: Typical shear response.

$$M_{xy} = \cos\alpha \sin\alpha M_{x'} = \frac{1}{2} M_{x'} \tag{4.23}$$

The failure criterion is used to predict the onset of failure on a self-deployable shell forming a corner, as discussed in chapter 3. A contour plot of the in-plane failure index, FI_1, on the two-ply region of a self-deployable shell optimized in chapter 3 is shown in Fig. 3.11a. Here, strength parameters measured at macro-scale were used to implement the failure criterion. The contour plot shows that the shell was not damaged when folded.

4.4 Size-Scaling Effects on Laminate Stiffness and Strength

The dominating effects in the experiments on thin and small plain-weave samples performed in this study are:

1. Edge effects due to dry spots in the laminate. These are common types of imperfections in pre-impregnated composites with high fiber volume ratio. When the edge of the sample cuts through a dry spot, the void between consecutive weaves of fibers is exposed, thus creating a notch on the edge.

2. Fiber pull-out due to short fibers in the laminate. Since the experiments were performed on $[45_{pw}]_2$ samples, the laminates are essentially made of short

fibers, which are pulled out of the surrounding matrix as a tension load is applied.

Figures 4.8 and 4.9 show two images of a 3 mm wide Astroquartz ® and cyanate ester sample, $[45_{pw}]_2$, taken with a manual, nosepiece type microscope (Nikon Eclipse LV150N). The objective lens used to take the images is a Nikon TU Plan Fluor 5X/0.15, with a magnification of 5X and a numerical aperture of 0.15. The exposure time that was used is 7.9 ms. The edges of the thin strip of composite material were laser cut. The two figures show the edge of the same sample in two different locations. While the image in Fig. 4.8 was taken at a location without visible imperfections near the edge, Fig. 4.9 shows many imperfections. They are mostly caused by dry spots forming while the composite is curing. This kind of imperfection is common in the material under study, because of its high fiber volume ratio, $V_f = 0.62$.

Circled in red in Fig 4.9 is a notch visible on the edge of the laminate. This type of defect appears frequently at the edges, whenever the laser cuts through a dry spot, thus exposing the void between consecutive weaves of fibers. While these edge defects measure only tens of microns, they can propagate and cause premature failure of the sample under tension. These effects are particularly important when testing samples only a few millimetres wide.

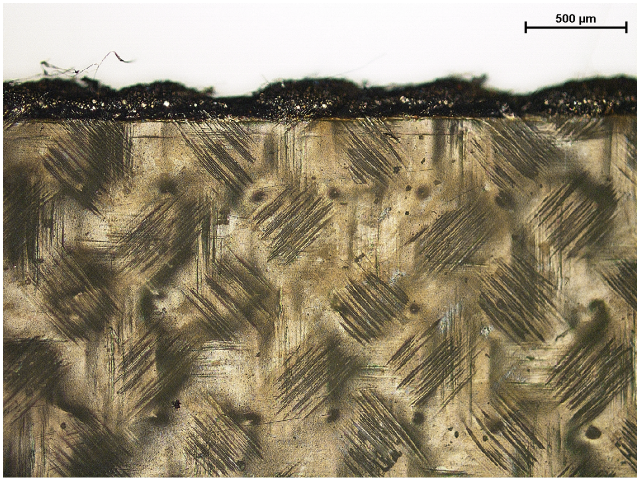

Figure 4.8: Edge of 3 mm wide, laser cut laminate, made of Astroquartz ® and cyanate ester resin, without visible defects.

Another effect to take into account is fiber pull-out. Fibers oriented at ±45°, in samples that are 3 mm wide or less, can only be as long as 4.25 mm. There are no

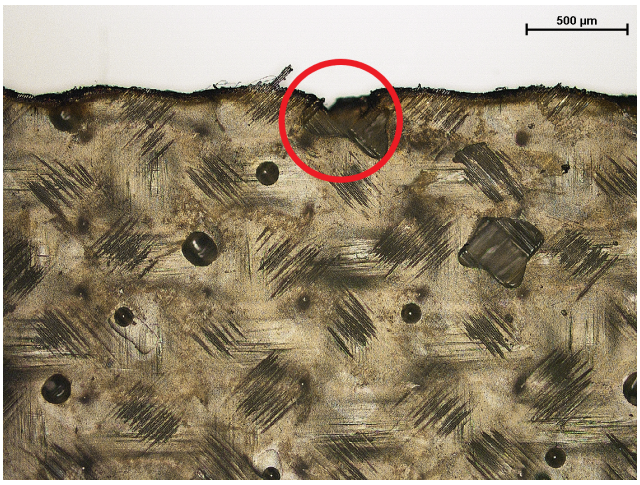

Figure 4.9: Edge of 3 mm wide, laser cut laminate, made of Astroquartz ® and cyanate ester resin, with defects, mostly due to dry spots.

fibers running through the entire length of the sample, as it would happen if fibers were oriented at 0°. Hence, when these samples are loaded in tension, bundles of fibers can pull out of the surrounding matrix, thus causing failure of the sample. Figure 4.10 shows a sketch that captures this process.

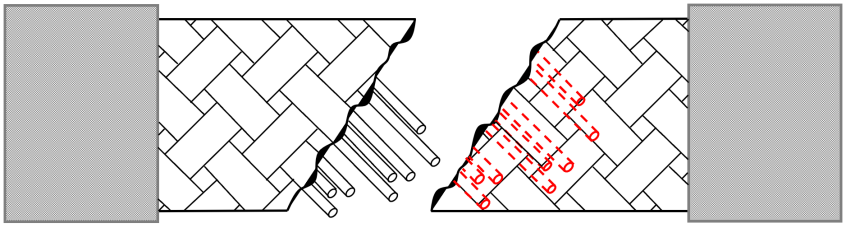

Figure 4.10: Illustration of fiber pull-out due to short fibers in the samples under study.

Seven different values of samples width, 25 mm, 20 mm, 15 mm, 3 mm, 2 mm, 1.5 mm, and 1 mm, were considered. Five to ten samples of each width were tested. The samples were laser cut, to replicate the manufacturing procedure used to place cutouts on the self-deployable shell. Tension tests were performed to measure the in-plane shear strength, F_3, following the procedure described in section 4.3. The dimensions of each sample were scaled according to ASTM Standards (Standard D3518/D3518M, 2007; Standard D3039/D3039M, 2009). The samples have constant, rectangular cross-section and a minimum length defined by the sum of gripping length (2×10 mm), two times the width of the sample, and gage length (11 mm). The width tolerance is ±1%. Figure 4.11 shows the typical test setup.

Failure must occur within the gauge length for a test to be considered successful, as shown for the 1.5 mm wide sample in Fig. 4.11.

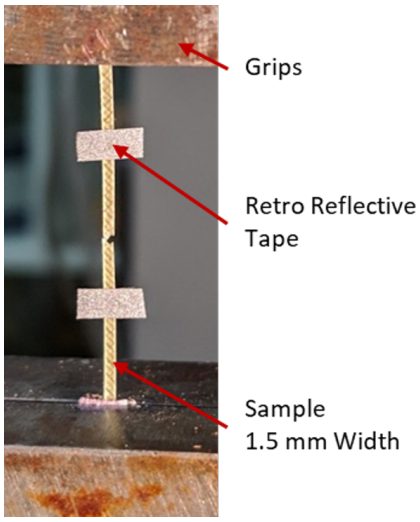

Figure 4.11: Tensile test setup.

Average shear stress curves for two-ply samples, plotted against the longitudinal strain, are shown in Fig. 4.12. Size-scaling effects in the shear strength are noticeable when decreasing the width of the samples tested. The shear strength of 1 mm wide samples is approximately one third of the shear strength of the 15 mm wide samples. Shear strength results are presented in Fig. 4.13. The results show that the shear strength of 1 mm wide samples is even lower than the typical shear strength of toughened cyanate ester resin. This result is coherent with the assumption that edge effects, which mostly appear while cutting through dry spots of composite material, trigger premature failure. Whereas, degassed, pure resin samples have less imperfections due to voids that can cause failure.

Figure 4.13 displays two different effects due to size-scaling. For larger samples, 25−15 mm, the data shows an increase in strength at smaller scales as predicted by theoretical and experimental studies on size-scaling effects on strength of brittle materials (Weibull, 1939; Bullock, 1974; Jackson, Kellas, and Morton, 1992; Bažant and Chen, 1999; Bažant, 2019). For smaller samples, 15−1 mm, the trend changes and the shear strength decreases with the size of the samples.

By focusing on the initial section of the shear response, Fig. 4.14, size-scaling effects on the slope of the curves are also visible. A linear approximation to the curves was chosen to estimate their slopes. This behavior was treated as a reduction in shear stiffness of the material, when cut in narrow strips. Hence, stiffness scaling

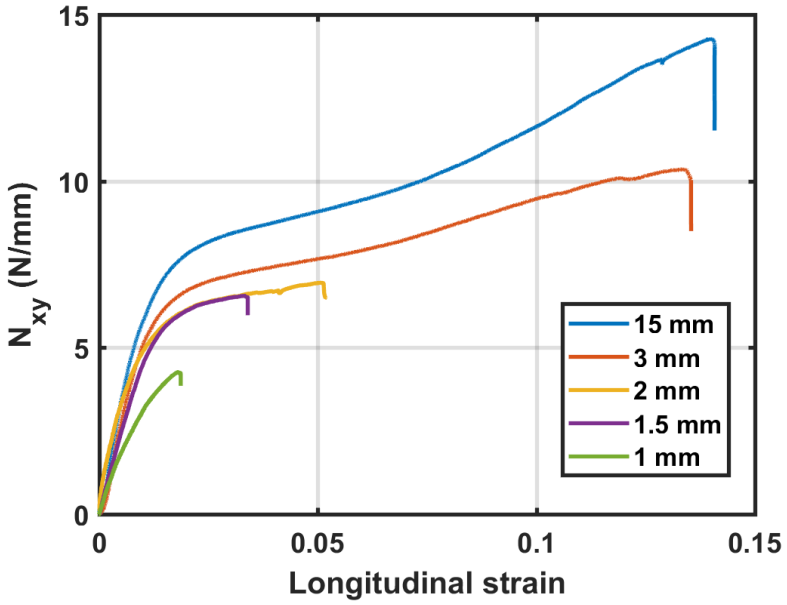

Figure 4.12: Average shear stress curves for $[45_{pw}]_2$ laminates at different scales, plotted against the longitudinal strain.

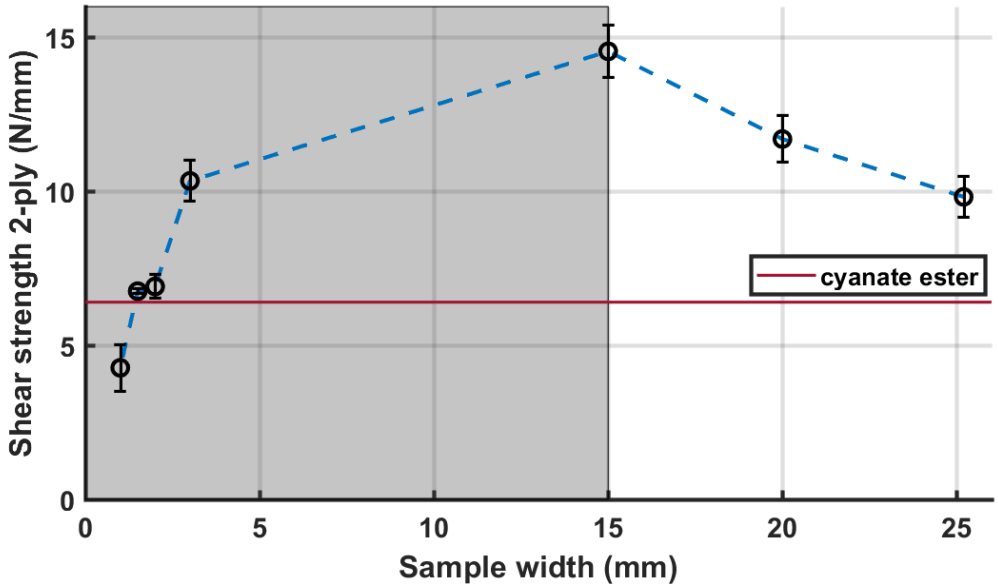

Figure 4.13: Shear strength of $[45_{pw}]_2$ laminates at different scales. Pure cyanate ester resin strength plotted as reference.

factors, sf_i, were derived and are summarized in Table 4.7. The shear coefficient, A_{66}, of the $\boldsymbol{A}$ matrix of the material was scaled according to the results found. A stiffness scaling factor is applied to the shear coefficient, depending on the average size of the sample, as follows:

$$\begin{bmatrix} A_{11} & A_{12} & 0 \\ A_{12} & A_{22} & 0 \\ 0 & 0 & A_{66}^{new} \end{bmatrix} = \begin{bmatrix} A_{11} & A_{12} & 0 \\ A_{12} & A_{22} & 0 \\ 0 & 0 & sf_i \times A_{66} \end{bmatrix} \tag{4.24}$$

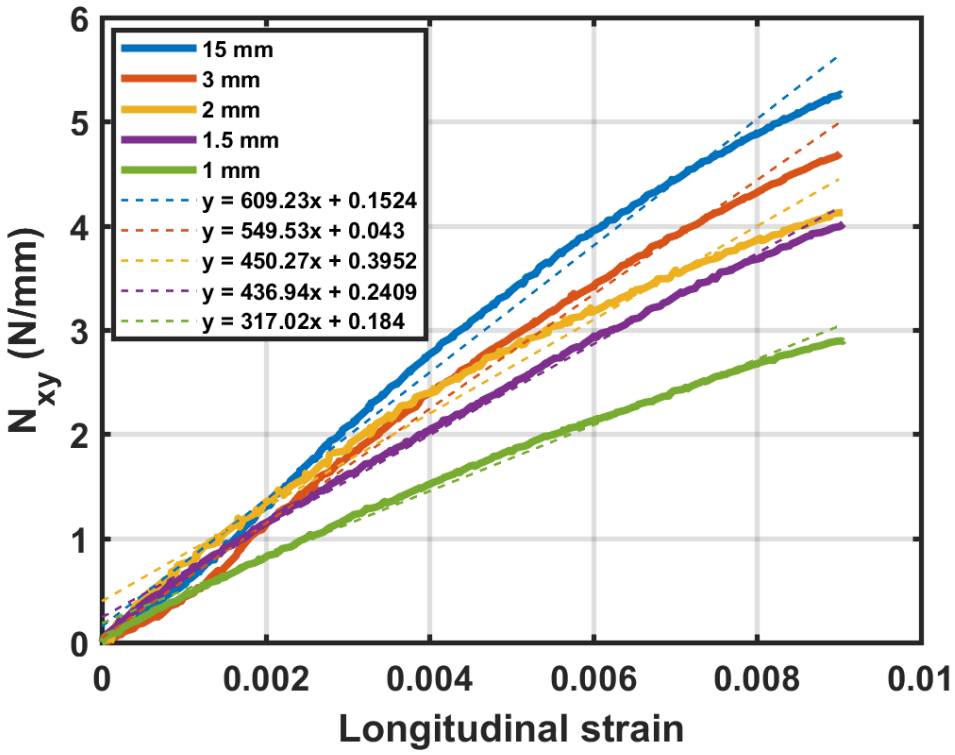

Figure 4.14: Initial part of shear stress curves and their linear trendlines.

The experimental results provided here show that both the shear strength and the stiffness of Astroquartz ® and cyanate ester resin laminates decrease with the size of the samples tested. Yet, another scaling effect must be considered. Equations 4.19-4.21 relate the compressive strength of the material to the yield shear stress. Therefore, we will assume that the same shear stiffness reduction can be assumed in scaling of compressive strength prediction, $F1_c$. The results are summarized in Table 4.7.

4.5 Introducing Size-Scaling Effects in Numerical Analysis of Shells Forming a Corner

Geometrically nonlinear simulations of a thin shell forming a corner were carried out using the commercial finite element software Abaqus 2017. A finite element model was built in Abaqus 2017 with S4R shell elements, as discussed in chapter

Table 4.7: Size-scaling on shear strength, compressive strength, and softening of ultra-thin, plain-weave Astroquartz ® laminates.

Sample Width [mm]	Shear Strength F_3 [N/mm]	Compressive Strength F_{1c} [N/mm]	Stiffness Scaling Factor, sf_i
15	14.55	34.50	1
3	10.34	29.07	0.902
2	6.91	25.94	0.739
1.5	6.76	25.70	0.717
1	4.27	19.37	0.520

3. Size-scaling effects in stiffness and strength of the material were defined in the model dividing into different sections the two-ply region of the shell, Fig. 4.15. A feature provided in Abaqus and called "general section properties" allowed to manually input the ***ABD*** stiffness matrix of each material section. The ***A*** matrix of laminates of different sizes was calculated according to Eq. 4.24.

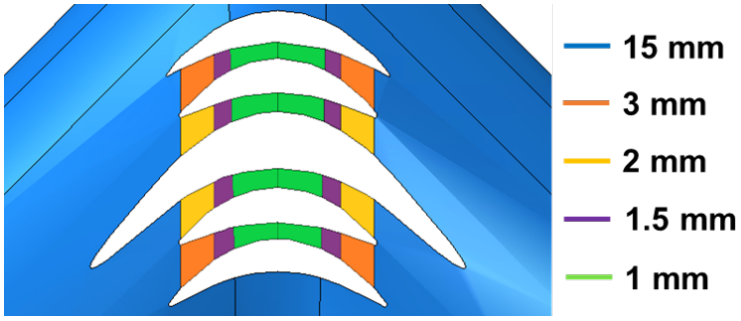

Figure 4.15: Sections of two-ply region simulated at different stiffness and strength scales.

The failure criterion described in section 4.3 was introduced in the simulations and size-scaling effects on strength parameters were considered, as listed in Table 4.7. A new contour plot of the in-plane failure index, FI_1, on the two-ply region of the shell was produced and it is shown in Fig. 4.16. Black areas plotted in Fig. 4.16 are regions where the first failure index is smaller than 1. White areas are regions corresponding to cutouts or parts of the shell that were excluded from the failure analysis. Finally, all the elements plotted with a color other than white or black have reached a failure index greater than 1.

While the analysis carried out without considering size-scaling effects, Fig. 3.11a, showed no signs of damage on the folded shell, this new analysis shows that a

few, localized elements fail on one of the thin strips of material that separate the cutouts. Each localized area of failed elements measures approximately 0.2 mm^2. This result is consistent with the contour plot of axial strain on the two-ply region of the self-deployable shell, Fig. 4.4, which shows a concentration of higher strain on the same area.

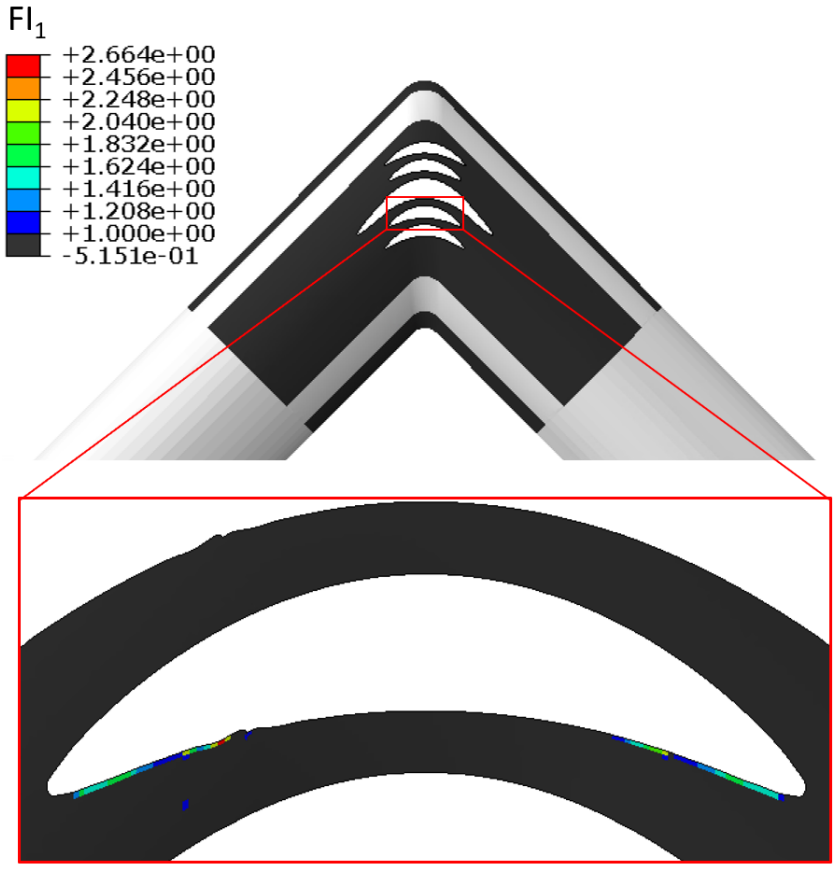

Figure 4.16: New contour plot of in-plane failure index, $\mathbf{FI_1}$, on two-ply region of self-deployable shell. Size-scaling effects were included in this analysis.

4.6 Experimental Analysis of Deployed Stiffness of Shells and Localized Damage

The stiffness reduction due to size-scaling effects raises concerns on whether the overall bending stiffness of the self-deployable shell is also reduced. Additionally, predictions of localized damage, obtained by introducing size-scaling effects on stiffness and strength of materials in numerical simulations, have highlighted the importance of being able to experimentally measure localized damage. Both these issues were addressed.

4.6.1 Overall Bending Stiffness of Shells Measured via Folding Tests

From the quasi-static folding experiments described in chapter 3, a moment-rotation profile was obtained by plotting the folding angle and the corresponding moment at each step, Fig. 4.17. Moment-rotation profiles resulting from numerical simulations were then superposed to the experimental one to validate the results.

The curves obtained from numerical simulations are perfectly overlapped, thus showing as a single curve in the plot. The blue curve, hidden behind the green one, was obtained by simulating a folding shell with stiffness and strength from results at macro-scale. Conversely, the green curve was obtained by introducing the size-scaling effects shown in Fig. 4.15. Although size-scaling effects on the strength of the material change the results from the failure criterion, as seen in Fig. 3.11a and 4.16, the effects on stiffness do not modify the overall bending stiffness of the shell, calculated from the moment-rotation curves using Eq. 3.4.

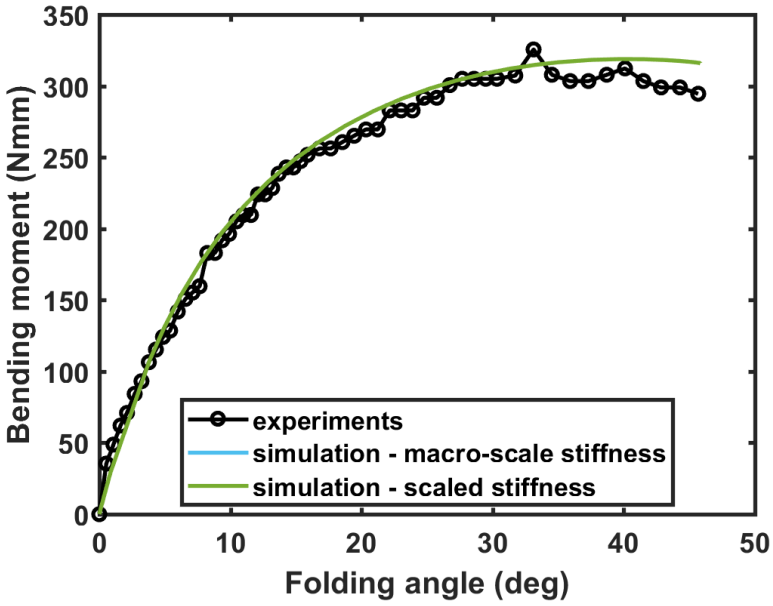

Figure 4.17: Test data compared to simulation results. The plot shows the reaction bending moments plotted against the folding angle; 0° corresponds to a fully deployed shell and the angle grows as the two tubes rotate towards each other.

4.7 Measurement of Localized Damage Near Cutouts

X-ray computed tomography (CT) allows to image structures in three dimensions with high spatial resolution (Stock, 2008; Bale et al., 2013), by combining X-ray measurements of a specific area of a scanned sample, taken from different angles, to produce cross-sectional images, called "slices". Using commercially available

software, the slices are then combined to produce a three-dimensional (3D) image. An example of a scan done on a self-deployable shell is shown in Fig. 4.18. The CT scanner is a ZEISS Xradia VersaXRM-510. The settings for the scan are: optical magnification 4X, exposure time 1 s, voltage 80 kV, power 7 W, and number of projections 3001. The area of interest is the same one showing elements with $FI_1 > 1$ in Fig. 4.16. The slices were reconstructed in a 3D rendering using Dragonfly software. The resolution chosen to scan the sample is:

$$1\,voxel = 4.38 \times 4.38 \times 4.38\,(\mu m^3) \tag{4.25}$$

where a voxel is a 3D generalization of a pixel. Since each fiber measures approximately 9 μm in diameter (JPS, 2017), the chosen resolution only allows for 2 pixels per fiber. Hence, a single fiber cannot be fully resolved. The advantage of this choice is a larger field of view in a single scan, which allows to inspect an area of approximately $4.5 \times 4.5\ mm^2$.

Strain components are measured via digital volume correlation (DVC) techniques (Xu, 2018). DVC is the three-dimensional extension of digital image correlation (DIC), which allows to obtain quantitative measurements of internal 3D material displacement fields (Bay, 2008). Two tomographic images, a reference image and a target image, are used to estimate the displacement field by finding a unique correspondence between features in the two images. A correlation between intensity patterns within interrogation windows allows to find the displacement vector at each measurement point, from which the strain components can then be calculated. To solve the correlation problem uniquely, the object volume must exhibit certain properties (Sutton, Orteu, and Schreier, 2009), such as: texture with no preferred orientation, non-periodic structures, and information for pattern matching available everywhere within the volume. These requirements usually lead to the use of random speckle patterns applied to the object volume.

Since the two-ply laminate used in this study is very thin, see Table 4.2, artificial speckles could both compromise the integrity of the test samples and cause complications in the manufacturing process. Hence, the weave pattern from the laminate itself was used, although it did not provide ideal conditions for correlation and caused measurement noise, discussed later in this chapter.

DVC begins by selecting a region of interest, populated by points where the displacement components are sought. Hence, tomographic images must be cropped

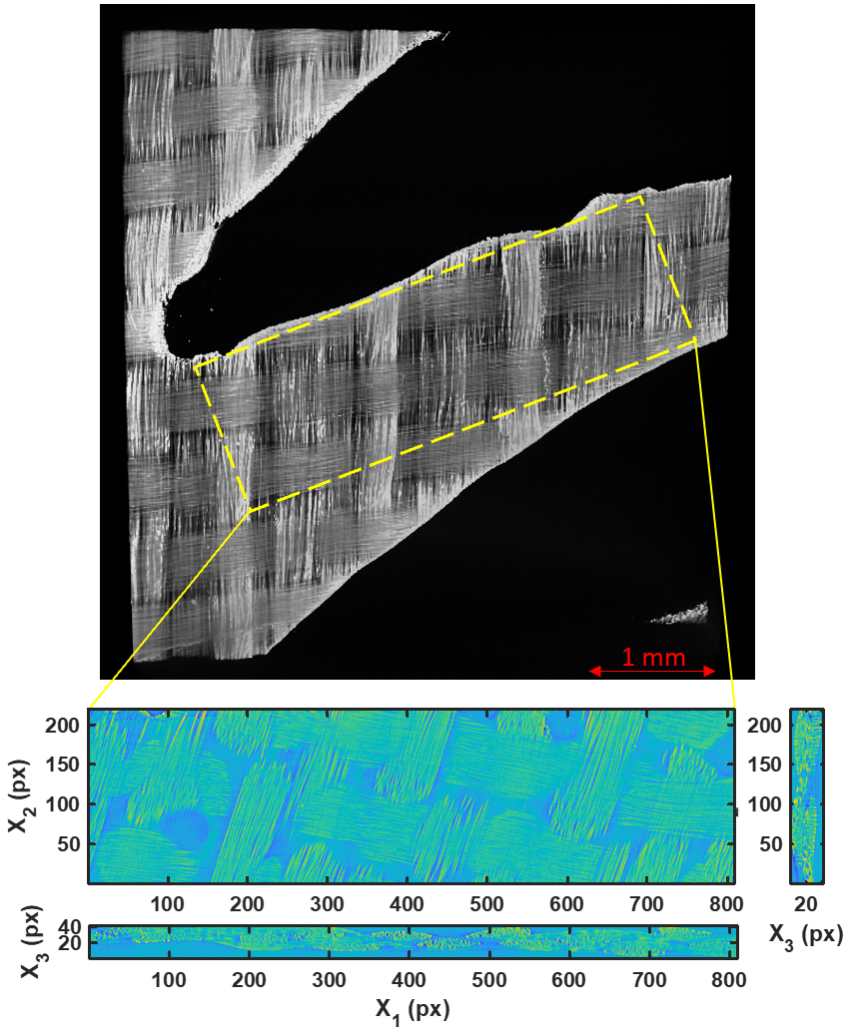

Figure 4.18: Computed tomography scan of two-ply, plain-weave laminate, focused on a region near one of the cutouts of the self-deployable shell, and portion of the tomographic image converted into a 3 rd order tensor.

accordingly, not to include voids, such as cutouts, within the region of interest, since voids do not carry any information for pattern matching. Subsequently, tomographic images must be converted into 3rd order tensors that store intensity values of each voxel.

Figure 4.18 shows the mid-planes of a portion of a tomographic image, centered on a thin strip of material between cutouts of a self-deployable shell, converted into a 3rd order tensor. A publicly available MATLAB based software for fast iterative digital volume correlation (FIDVC) (Bar-Kochba et al., 2015) was used to calculate the residual strains on the folded shell. This open source software was chosen because it allows for 3D full-field measurement of large-deformation internal

displacement fields. Once the displacements are known, the Lagrange strain tensor can be calculated as follows (Bower, 2011):

$$\boldsymbol{E} = \frac{1}{2}(\boldsymbol{C} - \boldsymbol{I}) \tag{4.26}$$

$$\boldsymbol{C} = \boldsymbol{F}^{\boldsymbol{T}} \cdot \boldsymbol{F} \tag{4.27}$$

$$\boldsymbol{F} = \boldsymbol{I} + \boldsymbol{u} \otimes \nabla \tag{4.28}$$

where $\boldsymbol{C}$ is the right Cauchy-Green deformation tensor, $\boldsymbol{I}$ is the identity matrix, $\boldsymbol{F}$ is the deformation gradient tensor, and $\boldsymbol{u}$ is the displacement field.

4.7.1 Measurement Noise and Calibration of Digital Volume Correlation Algorithm

A threshold for measurement noise was estimated by correlating a reference tomographic image and a target image of a flat sample. Both the scan region and the measurement are shown in Fig. 4.19. The sample has the same layup, $[45_{pw}]_2$, as the region of the shell forming a corner that was investigated. A first, reference image was taken by scanning an area of the sample, red box in Fig. 4.19, at the same spatial resolution used to scan the shell. A second, target image was taken after removing the sample from the CT scanner and replacing it inside the chamber without applying any strain to it. Hence, the sample scanned has nominally zero residual strain. A coarse alignment within the chamber was sufficient to scan approximately the same area.

The in-plane $\mathbf{E_{11}}$ component of the residual strains, calculated on the mid-plane, is shown in Fig. 4.19. The contour plot shows fictitious residual strain as high as 0.43%. Measurement noise is expected in this kind of tomographic images and it is mostly due to inconsistent speckle patterns (Liu and Morgan, 2007) and periodicity of the image, due to the pattern formed by the plain-weave, which can lead to misregistration problems (Sutton, Orteu, and Schreier, 2009) as previously mentioned.

When calibrating the FIDVC algorithm for the 3D images used in this study, the fictitious residual strain was initially in the 15% range. Several steps were taken to reduce the baseline noise, finally achieving the value of 0.43% mentioned above. There are four key steps, which can be summarized as follows:

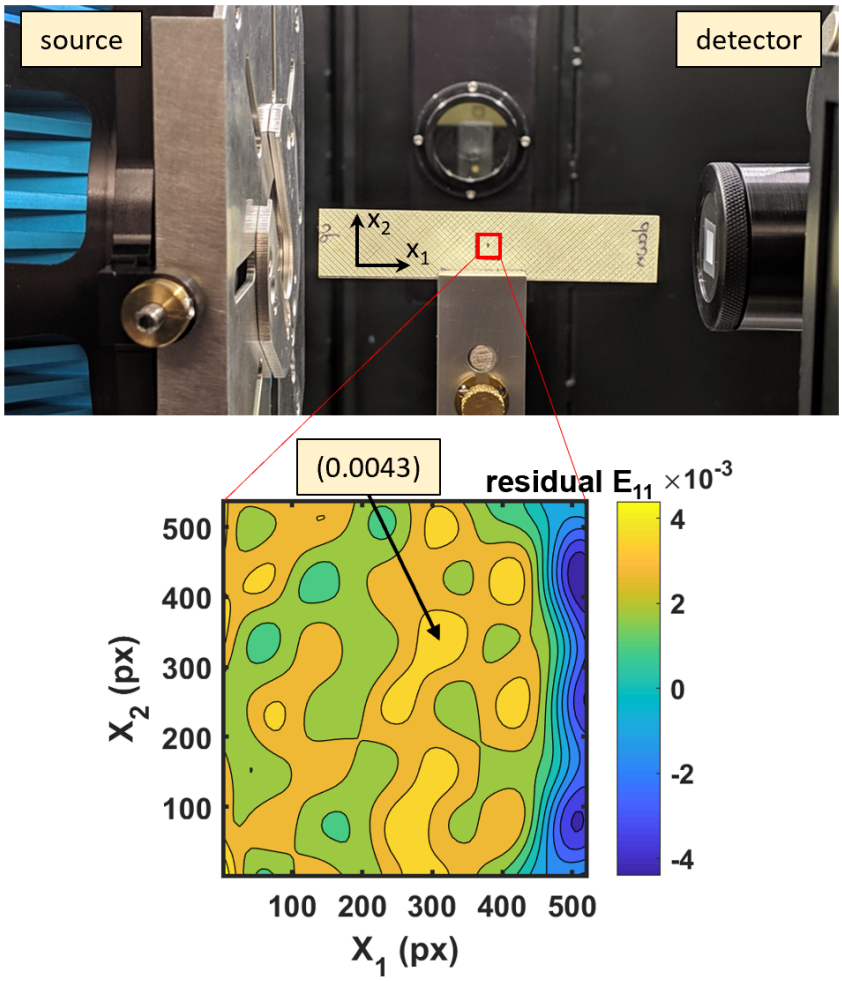

Figure 4.19: Measurement noise on tomographic images of a flat, unstrained sample, correlated via FIDVC. The contour plot shows the first, in-plane component of the Lagrange strain, $\mathbf{E_{11}}$.

- **Step 1.** Find correct size of interrogation window and mesh grid spacing on numerically strained images (no experimental measurement noise).
- **Step 2.** Measure baseline noise from numerical rigid body motion and estimate admissible rigid body displacements.
- **Step 3.** Reduce noise from rigid body motion using registration of images by decreasing rigid body offset to an admissible range.
- **Step 4.** Reduce residual noise from experimental measurement using a low-pass Gaussian filter.

Here we will discuss in detail how the four steps were implemented. Each tomo-

graphic image is a spatial domain discretized in units of volume, i.e. voxels. The region of interest is defined within the global voxel domain and meshed using standard meshing tools. The nodes of the mesh become the displacement measurement points. Hence, the spacing of the mesh grid is one variable that must be tuned. Subsequently, the displacement vector at each measurement point is estimated via a correlation algorithm, which subdivides the region of interest into interrogation windows of specified overlap ratios, i.e. voxel subvolumes. The size of the interrogation window is another variable that must be adjusted.

Step 1 of the calibration procedure for the chosen FIDVC algorithm aims to find the appropriate values for these two variables. To do so, no experimental measurement noise is introduced in the tomographic images, and the correlation pair is simply obtained by applying a numerical strain to a reference image. Figure 4.20 shows the example of a 15% strain applied to a reference tomographic image, although only one slice of the image is displayed for clarity. In this case, an affine transformation was applied to the reference image, using the *imwarp* function provided in MATLAB. The image was subjected to uniform strain in the $\mathbf{X_1}$ direction.

The range of strain that is interesting for this study is within 2%, as shown in Fig. 4.4. Both reference and strained images were processed using the FIDVC software and the results are shown in Fig. 4.21. Contour plots of the displacement field, particularly the $\mathbf{u_1}$ component, were generated for different values of the interrogation window size and the mesh grid spacing.

The first image, 4.21a, shows results for a window size of $32 \times 32 \times 32$ voxels and a mesh grid spacing of 4 voxels. The displacement field is visibly noisy and does not uniformly increase along the $\mathbf{X_1}$ direction, as expected. Some of the noise, corresponding to the blue contours in Fig. 4.21a, localizes in regions of the image that do not show any speckles, because of voids between consecutive weaves of fiber.

The second image, 4.21b, was obtained using a window size of $64 \times 64 \times 32$ voxels and a mesh grid spacing of 4 voxels. The window size was increased in the $\mathbf{X_1}$ and $\mathbf{X_2}$ directions, but left unchanged in the $\mathbf{X_3}$ direction, which runs through the thickness of the material. Since the samples scanned are very thin, there are on average only 40 pixels in the $\mathbf{X_3}$ direction for each image. While a uniformly increasing displacement field starts emerging from the data, the contour plot is still noisy.

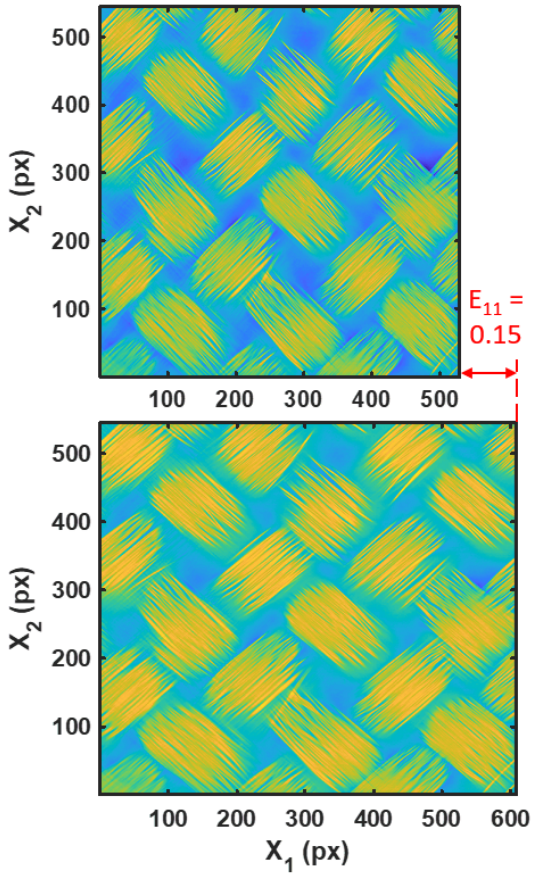

Figure 4.20: Example of numerical strain of 15% in $\mathbf{X_1}$ direction, applied to one slice of a tomographic image.

The third image, 4.21c, shows the results for a window size of 128 × 128 × 32 voxels and a mesh grid spacing of 4 voxels. The displacement field is less noisy, especially in the regions $0 < \mathbf{X_2} < 100$ and $450 < \mathbf{X_2} < 550$. Finally, the last image, 4.21d, was obtained using a window size of 128 × 128 × 32 voxels and a mesh grid spacing of 8 voxels. The data is greatly improved and shows a uniform increase of the displacement component $\mathbf{u_1}$ along the $\mathbf{X_1}$ direction. This displacement field was used to calculate the Lagrange strain tensor, using Eq. 4.26-4.28. Figure 4.22 shows the resulting contour plot of the in-plane $\mathbf{E_{11}}$ component of the Lagrange strain. An average 2% strain is recovered from the correlation, thus indicating that a correct choice had been made for the values of the interrogation window size and the mesh grid spacing.

Two factors must be taken into account when analyzing the results presented here. First, optimal values of interrogation window size and mesh grid spacing change depending on the global voxel domain of a tomographic image. Hence, if the size

of the image changes, for example because void regions must be cropped out, the optimal values also change. Second, the FIDVC algorithm produces the largest errors near the edges of the image. Hence, the in-plane contour plots shown here do not include values near the edges. The size of the region near an edge, in the $\mathbf{X_1}$-$\mathbf{X_2}$ plane, on which data is discarded equals the interrogation window size. The same rationale cannot be applied to through-thickness data, since there aren't enough pixels in the $\mathbf{X_3}$ direction. Hence, results for out-of-plane components of the Lagrange strain are not presented here because they are not accurate enough.

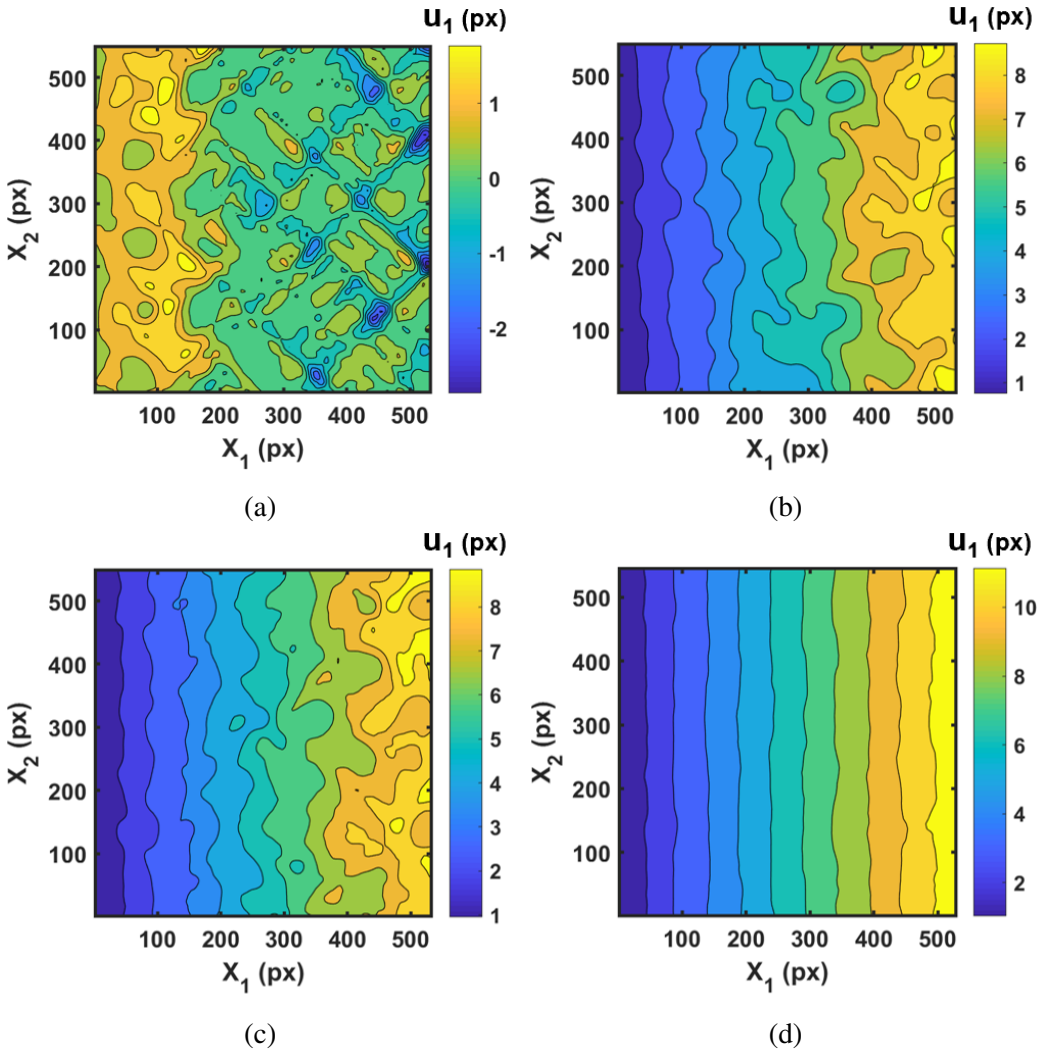

Figure 4.21: Contours of $\mathbf{u_1}$ component of the displacement field plotted on mid-thickness slice. Interrogation window size, $sSize$, and mesh grid spacing, dm used to correlate reference and target tomographic images are as follows: (a) $sSize = [32 \times 32 \times 32]$, $dm = 4$; (b) $sSize = [64 \times 64 \times 32]$, $dm = 4$; (c) $sSize = [128 \times 128 \times 32]$, $dm = 4$; (d) $sSize = [128 \times 128 \times 32]$, $dm = 8$.

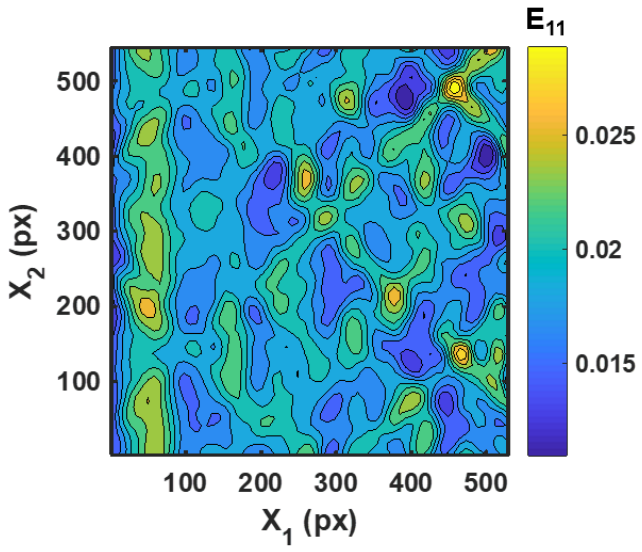

Figure 4.22: Contour plot of $\mathbf{E_{11}}$ component of Lagrange strain resulting from cross-correlation for numerically applied $\mathbf{E_{11}}$ strain of 2%.

Rigid registration pre-processing is not performed by the FIDVC algorithm. Hence, reference and target tomographic images are not aligned prior to their cross-correlation. Since the images processed in this study produce a periodic speckle pattern, rigid body motion can cause misregistration problems. Hence, in calibrating the FIDVC algorithm, studies were performed to measure the baseline noise produced by pure rigid body motion of the image, without any experimental measurement noise. Two cases were studied. First, a numerical translation of the image, with absolute value smaller than the interrogation window size, Fig. 4.23. Second, a numerical translation with absolute value larger than the interrogation window size, Fig 4.25.

For the first case, an in-plane translation of 50 pixels in the $-\mathbf{X_1}$ direction was applied to the reference image. A contour plot of the $\mathbf{u_1}$ component of the displacement field is shown in Fig. 4.24a. The ideal result would be a uniform distribution of $\mathbf{u_1} = -50$ pixels. In reality, an error up to 5 pixels occurs. The $\mathbf{E_{11}}$ component of the Lagrange strain was calculated from the displacement field and the results are plotted in Fig. 4.24b. Since no numerical strain was applied to the reference image, every component of the Lagrange strain calculated from DVC data should be null. Nevertheless, fictitious strain values reach peaks of 15%, as shown in Fig. 4.24b.

The second case of numerical rigid body motion that was analyzed is a translation of 200 pixels in both $-\mathbf{X_1}$ and $-\mathbf{X_2}$ directions, as shown in Fig. 4.25. Since this motion

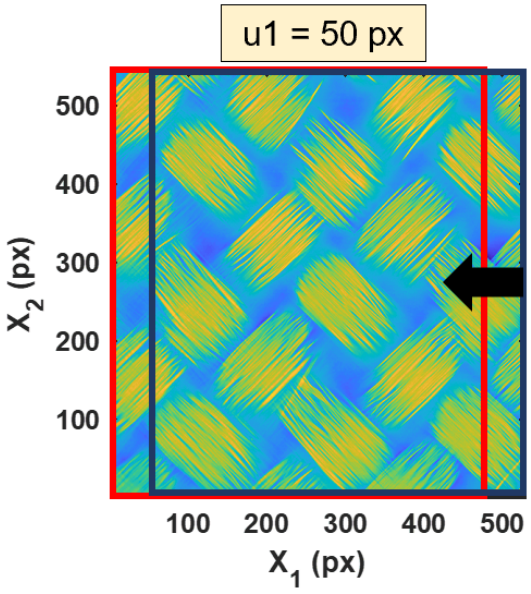

Figure 4.23: Example of numerical translation of an image where the applied displacement, $\mathbf{u_1}$ = 50 pixels, is smaller than the interrogation window size, $sSize = [128 \times 128 \times 32]$.

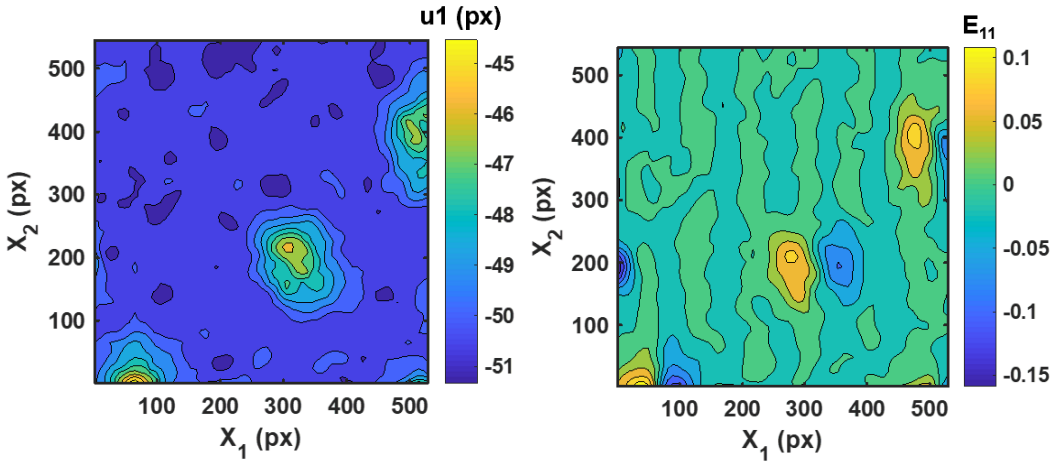

(a) (b)

Figure 4.24: Contour plots of (a) $\mathbf{u_1}$ component of displacement field and (b) $\mathbf{E_{11}}$ component of Lagrange strain resulting from cross-correlation for numerically applied displacement $\mathbf{u_1}$ = 50 pixels and nominally zero strain.

is larger than the interrogation window size, inaccurate results were expected. Figure 4.26 shows the $\mathbf{u_1}$ component of the displacement field, which is visibly incorrect. The Lagrange strain tensor was also calculated form this displacement field and showed peak strain values of 100%. This study shows that the effects of rigid body motions on the reference images of interest are not negligible.

Inaccurate measurement of displacement field when the absolute value of the imposed translation is larger than the interrogation window size was expected. Nevertheless, it was shown that large, fictitious strain values are also measured when the absolute value of the imposed translation is smaller than the interrogation window size, which is not an intuitive result. Hence, the need for a rigid registration pre-processing was clearly established. A preregistration of the reference and target images was performed. The process consisted of aligning the markers in the reference and target volumes. This helped greatly in reducing rigid body motion between the two tomographic images to an admissible range of less than 10 pixels.

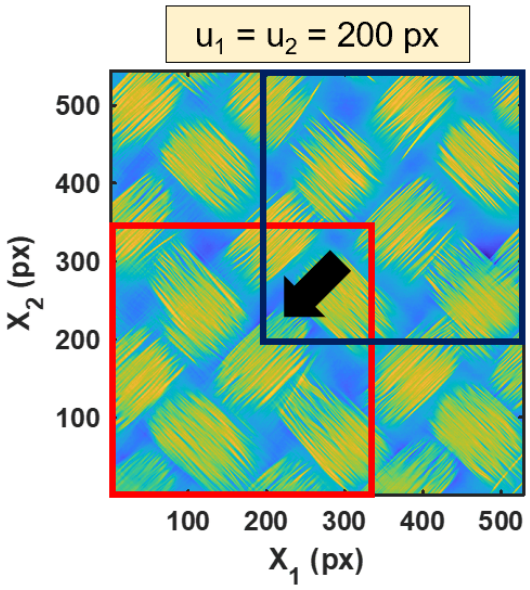

Figure 4.25: Example of numerical translation of an image where the applied displacements, $\mathbf{u_1} = \mathbf{u_2} = 200$ pixels, are larger than the interrogation window size, $sSize = [128 \times 128 \times 32]$.

The calibration efforts described so far did not include any noise from experimental measurements. The process of acquiring two different tomographic images by scanning the same sample twice introduces noise. Part of the noise comes from temperature fluctuation within the CT scanner chamber. The most common source of noise from an image acquisition system can be modeled as Gaussian random noise. Numerous image denoising models have been introduced in the past few decades. Conventional filters such as averaging filter, median filter, and Gaussian filter are efficient in smoothing the noise (Jain, 1989). Therefore, after feeding the two images to the FIDVC algorithm and calculating residual strain, an additional spatial filter is applied to the strain values. The purpose of the filter is to eliminate

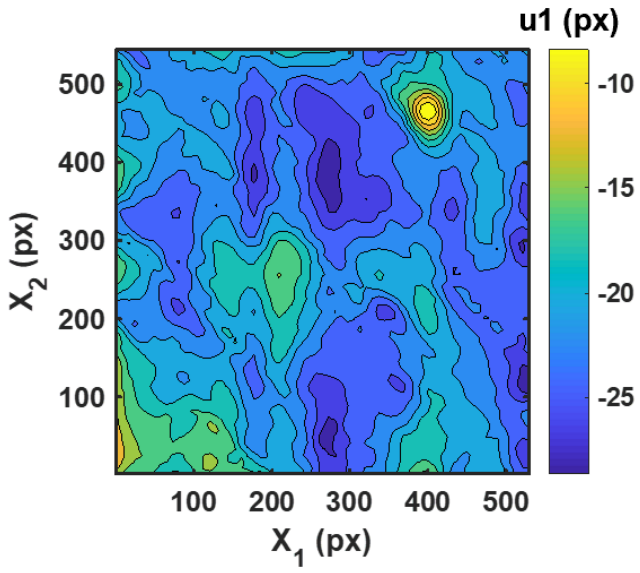

Figure 4.26: Contour plot of $\mathbf{u_1}$ component of displacement field resulting from cross-correlation for numerically applied displacements $\mathbf{u_1} = \mathbf{u_2} = 200$ pixels.

high spatial frequency features, using the repeating wavelength of the weave, λ_c, shown in Fig. 4.27, as cutoff value. A low-pass Gaussian filter was implemented as follows:

$$G_{LP}(u, v) = 1 - e^{\frac{-(u^2+v^2)}{2\sigma_c^2}} \tag{4.29}$$

$$\sigma_c = \frac{1}{\lambda_c}\left(\frac{1}{\mu m}\right) \tag{4.30}$$

where u, v are the spatial frequencies in the $\mathbf{X_1}$ and $\mathbf{X_2}$ directions, respectively; σ_c is the "floor frequency" defining the width of the Gaussian function and therefore the range of frequencies to be filtered. To show the effects of the Gaussian filter, two consecutive scans of the same sample were taken. The sample was not removed from the chamber between scans, thus eliminating errors resulting from rigid body motions. The two scans targeted exactly the same volume, and hence no preregistration of the tomographic images was needed.

Figures 4.28a and 4.28b show contour plots of the $\mathbf{E_{11}}$ component of the Lagrange strain measured before and after applying a low-pass Gaussian filter. The noise from experimental measurement was reduced by an order of magnitude.

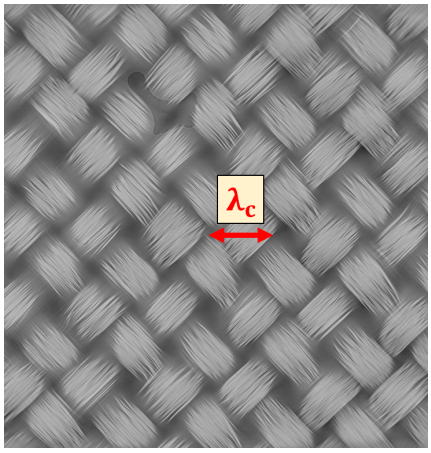

Figure 4.27: Repeating wavelength of plain-weave pattern used for DVC.

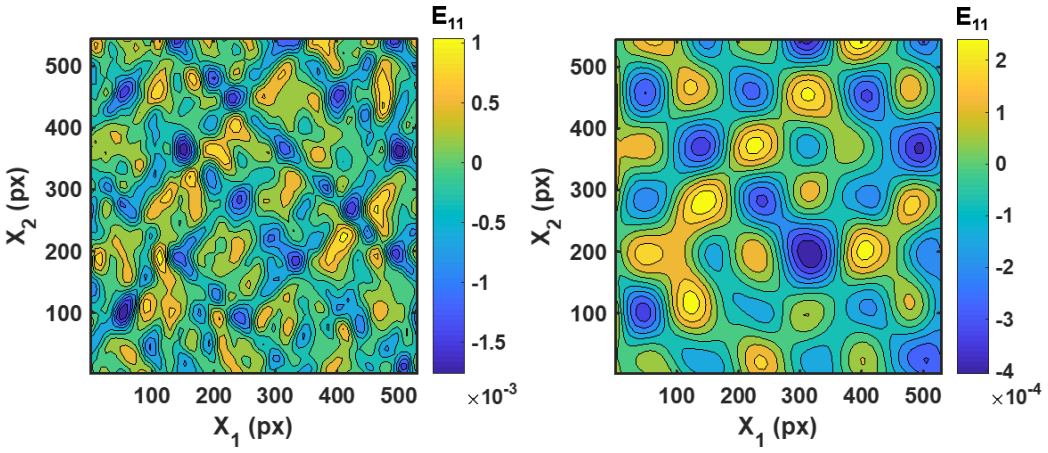

(a) (b)

Figure 4.28: Contour plots resulting from cross-correlation of tomographic images of two consecutive scans of the same sample. No rigid body motion or strain was applied, hence only experimental measurement noise is present. (a) $\mathbf{E_{11}}$ component of Lagrange strain, (b) $\mathbf{E_{11}}$ component of Lagrange strain with a low-pass Gaussian filter applied to the results.

By applying steps 1-4 of the calibration procedure, the measurement noise was reduced to the example shown in Fig. 4.19. The baseline noise is related to the speckle pattern in the tomographic images. Since the fiber weave itself was used, without any artificial speckles added to the images, the spatial resolution at which the images are acquired can change the noise level. Particularly, the images used for calibration have the same spatial resolution as the images taken from scans of a self-deployable shell, Eq. 4.32, to keep the calibration consistent. But, as mentioned before, this resolution does not allow to fully resolve a single

fiber. Hence, another study was conducted to clarify whether increasing the spatial resolution of a tomographic image, with the same weave pattern, would reduce the level of noise.

Figure 4.29 shows a CT scan of a two-ply, plain-weave, flat laminate and its conversion into a 3rd order tensor. The spatial resolution used to conduct the scan is as follows:

$$1\,voxel = 0.7 \times 0.7 \times 0.7\,(\mu m^3) \tag{4.31}$$

While each fiber is well resolved, as can be seen from the tomographic reconstruction of the scanned volume, the field of view is reduced to less than 1 mm. Consequently, each slice of the tomographic image lacks the presence of speckles in large areas of the slice. This is visible in the mid-thickness slice shown in Fig. 4.29. Since a crucial property of the object volume for DVC is to carry information for pattern matching everywhere within the volume, inaccurate results can be expected when correlating these kind of images.

Two consecutive scans at high resolution of the same flat sample were taken. The calibration procedure described before was applied, except for manual registration, which was not needed since the sample was not removed from the chamber between scans. Figure 4.30 shows a contour plot of the $\mathbf{E_{11}}$ component of the Lagrange strain measured via FIDVC. Fictitious residual strain reaches values of 3.5%, much higher than the peak baseline noise of 0.43% obtained when correlating images at lower spatial resolution. Hence, lack of information for pattern matching in tomographic images of plain-weave samples with high spatial resolution produces greater errors than poorly resolved fibers in images at lower spatial resolution.

4.7.2 Digital Volume Correlation Algorithm Applied to Tomographic Images of a Self-Deployable Shell

Scans of selected areas of the self-deployable shell forming a corner were taken before and after folding the shell. The reference tomographic images, from scans taken before folding the shell, were then correlated to deformed images, from scans of the same areas on the shell but taken after folding it. Results obtained on two regions of interest (ROI) are presented here.

Figure 4.31 shows a contour plot of the first failure index on the two-ply region of the shell, where a minimum value of $FI_1 = 0.1$ was set for the color bar. Two regions

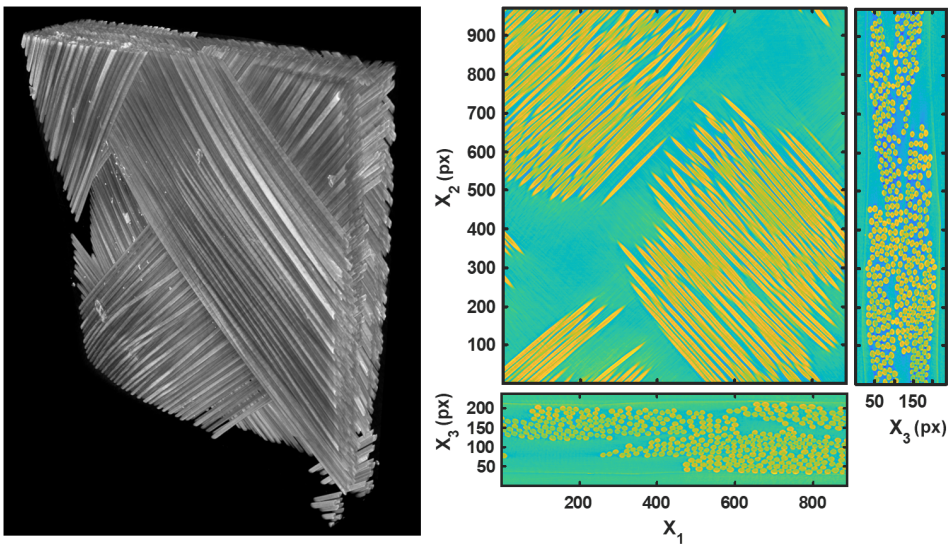

Figure 4.29: Tomographic reconstruction of CT scan of a two-ply, plain-weave, flat laminate acquired with a spatial resolution of 0.7 μm and its conversion into a 3rd order tensor.

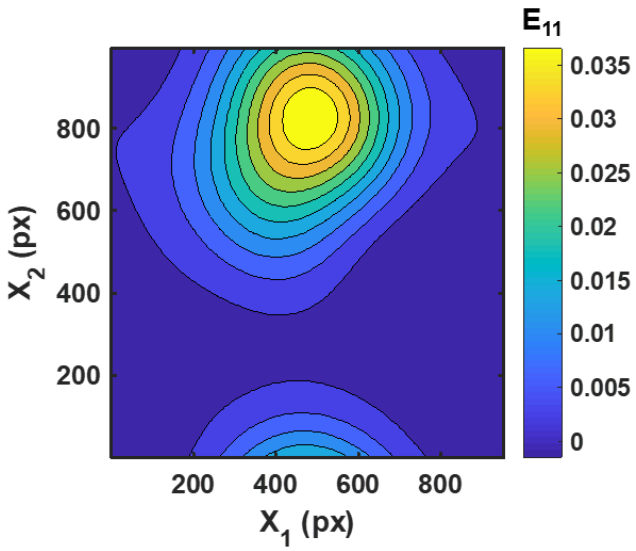

Figure 4.30: Contour plot of $\mathbf{E_{11}}$ component of Lagrange strain resulting from cross-correlation of tomographic images of two consecutive scans at high resolution of the same sample. Although a calibration procedure was applied to the images, fictitious residual strain reaches values of 3.5% because of lack of information for pattern matching in tomographic images.

of interest, ROI 1 and ROI 2, are marked with a red box. The onset of failure was numerically predicted for ROI 1, see Fig. 4.16. Note that ROI 1 lies in a thin strip of material between two cutouts of the self-deployable shell. The same area of interest is shown in Fig. 4.18.

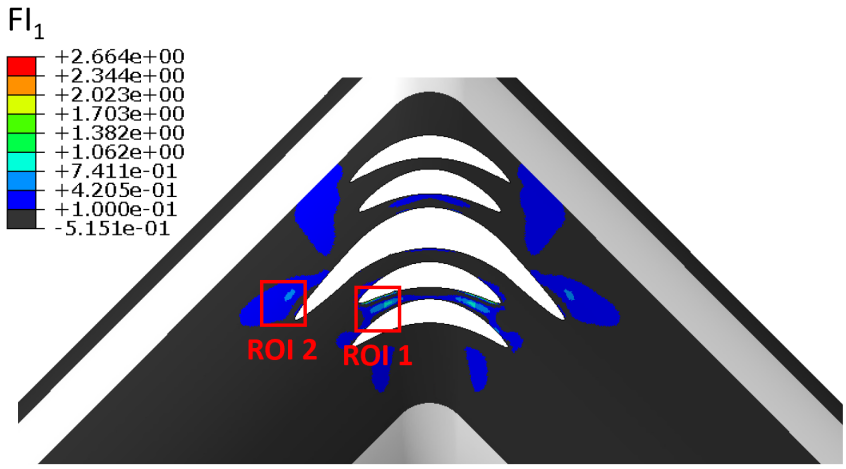

Figure 4.31: Contour plot of first failure index on two-ply region of self-deployable shell. A minimum value of $\mathbf{FI_1} = 0.1$ was set for the color bar. Two regions of interest (ROI) are identified.

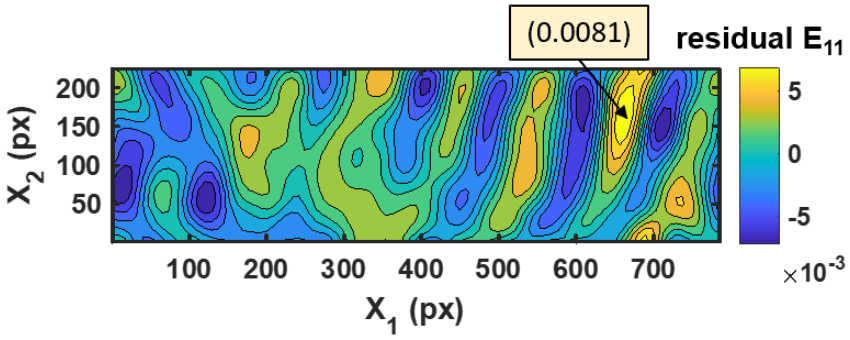

Figure 4.32: Contour plot of $\mathbf{E_{11}}$ component of Lagrange strain resulting from cross-correlation of tomographic images from ROI 1, obtained before and after folding a self-deployable shell. Localized damage was detected.

Figure 4.32 shows the residual strain measured on ROI 1. The contour plot of the in-plane component of the Lagrange strain, $\mathbf{E_{11}}$, calculated on the mid-plane, shows a residual strain as high as 0.81%. This value of the residual strain is higher than the measurement noise value, of 0.43%, thus indicating that localized damage occurred on this region of the shell. This experimental finding is in agreement with numerical predictions, Fig. 4.16, of localized damage in the same thin strip between cutouts. Additionally, the size of the areas affected by numerically predicted damage and experimentally measured damage are comparable.

Numerically predicted damage is localized near the edge of the thin strip, in areas measuring approximately 0.2 mm^2, and defined with a spatial resolution equal to the average element size near the cutouts of 125 μm. The highest residual strain,

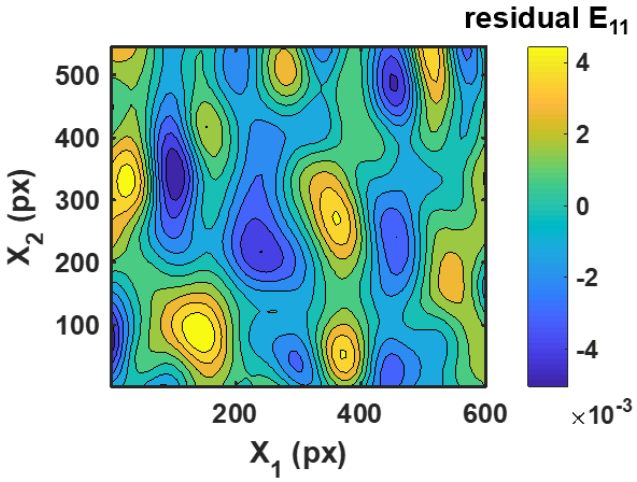

Figure 4.33: Contour plot of $\mathbf{E_{11}}$ component of Lagrange strain resulting from cross-correlation of tomographic images from ROI 2, obtained before and after folding a self-deployable shell.

measured experimentally, is also localized near the edge of the thin strip in an area measuring approximately 0.04 mm^2, with a spatial resolution of 35 μm. The spatial resolution for the results obtained via DVC is calculated as the product between the spatial resolution of the tomographic images (voxel size) and the mesh grid spacing (Xu, 2018) chosen to run the FIDVC algorithm. Since a voxel measures the same length in all three directions, $\mathbf{X_1}$, $\mathbf{X_2}$, and $\mathbf{X_3}$, and the mesh grid spacing is also the same, the spatial resolution resulting from DVC can be written as:

$$r = px \times dm = 4.38\,(\mu m) \times 8 = 35\,(\mu m) \tag{4.32}$$

where px is the size of the pixel in the tomographic images and dm is the chosen mesh grid spacing for the FIDVC algorithm.

Figure 4.33 shows the residual strain measured on ROI 2. The contour plot of the $\mathbf{E_{11}}$ component of the Lagrange strain shows that the magnitude of the residual strain field is comparable to the measurement noise value, of 0.43%. Hence, it is not possible to establish whether localized damage occurred in this region.

4.8 Conclusion

Previously published experimental studies have provided evidence of size-scaling effects in unidirectional composite material with length ranging between 50.8 mm and 12.7 mm, but no studies were found that investigate size-scaling effects on thin, plain-weave composite material with smaller length.

The results presented in this chapter confirm literature studies on size-scaling effects on strength of brittle materials, which predict an increase in strength at smaller scales. Additionally, they provide evidence of size-scaling effects in small plain-weave samples, with length ranging between 15 mm and 1 mm. Two dominating effects in experiments on these kind of samples have been identified. First, edge effects due to dry spots in pre-impregnated composites with high fiber volume ratio. Second, fiber pullout due to the short length of the fibers oriented at ± 45° with respect to the loading direction. A reduction in shear strength was observed. Similarly, a softening behavior was measured when loading the samples in tension. These effects are summarized in Table 4.7.

A case study of a self-deployable shell was used to demonstrate how size-scaling, introduced in numerical simulations, influences the results of failure analysis. The scope of this case study was to show the results of two concurrent effects on thin strips of material that form of foldable structures because of cutouts: first, strain localization, and second, a reduction in strength and stiffness of the strips because of size-scaling. It was demonstrated that if size-scaling is not taken into account then the failure analysis can be inaccurate and lead to non conservative predictions.

Finally, methods for measuring localized damage were discussed. Although acceptable in many situations, because of the negligible area of the small region it affects, localized damage is measurable in high-strain composite structures with thin strips of material. The work presented here showed the existence of localized damage, which occurs as a consequence of size-scaling effects studied on plain-weave laminates, in both numerical and experimental results. A laminate failure criterion, suitable for ultra-thin, plain-weave composites, was used to predict damage of a folded shell. A localized area of elements with $FI_1 > 1$, measuring approximately 0.2 mm^2, was calculated on a thin strip of material between cutouts, once the size-scaling effects had been introduced in the numerical simulations. Additionally, residual strains of 0.81% were measured on the same strip of material using computed tomography scans and digital volume correlation techniques. The magnitude of the residual strains exceeded the baseline measurement noise, thus indicating that localized damage had taken place.

Chapter 5

CONCLUSIONS AND FUTURE WORK

5.1 Summary and Contributions

This research has presented the first extensive study on topology optimization of deployable, composite thin shells using a geometrically nonlinear model and imposing stress constraints in the deformed configuration. The objective was to find non intuitive shapes of thin shells that can fold without being damaged, while also maximizing the deployed stiffness. The work has demonstrated that size-scaling effects in thin, plain-weave composites at small length scales produce a reduction in stiffness and strength of this type of material, thus affecting predictions of the onset of failure on deployable shell structures.

5.1.1 Density-Based Approach to Topology Optimization of Bending Dominated Shells with Geometrical Nonlinearities

An approach to topology optimization of thin shells in bending based on density distribution methods has been proposed. First, a mathematical formulation of the optimization problem and interpolation schemes for stiffness tensor, volume, and stress have been presented. Second, a sensitivity analysis for a gradient based optimization algorithm has been performed. The algorithm has been first tested on a classical benchmark problem, the Messerschmidt-Bölkow-Blohm (MBB) Beam problem, and the result has been compared to a solution found in literature. Then, a study of thin plates in bending has been performed and solutions to linear problems have been examined against solutions obtained with a commercial topology optimization tool. Finally, geometrically nonlinear problems with volume and stress constraints in the deformed configuration have been studied and successful solutions to a thin plate and a tape spring have been presented.

Contributions from this work are:

- A novel optimization algorithm that makes no assumptions on initial number, shape, and location of cutouts on deployable thin shells and that can impose volume and stress constraints in the deformed configuration of the shells, while also maximizing the deployed stiffness.

- An optimization analysis of the structure that is decoupled from the structural analysis, thus allowing the use of a commercial software to build the finite element model.

- A study of the effects of volume and stress constraints imposed in the deformed configuration of thin shell structures using both linear and geometrically nonlinear finite element models and a comparison of the solutions from the linear analysis to the results obtained with a commercial tool for topology optimization.

5.1.2 Topology and Shape Optimization of Composite Self-Deployable Thin Shells

Two optimization methods that provide more specific solutions to the problem of composite, deployable shells have been proposed. The first method uses level-set functions to place cutouts on the shells, so that they can fold without being damaged, while also maximizing the deployed stiffness. The second method uses a spline representation of the contour of a single cutout on the shell, thus performing fine tuning of the shape of the cutout. First, a design of a thin shell forming a corner with no cutouts has been presented and the choices of a particular material and laminate have been discussed. Then, techniques to analyze the shell have been introduced. Specifically, a geometrically nonlinear finite element analysis, to study the folding behavior of the shell, and a failure criterion. Preliminary design choices based on physical intuition have been shown and a first successful shape of cutout that satisfies the failure constraint has been found. Since the cutout removed a large area of the shell, the deployed stiffness was greatly reduced. Optimization studies have been carried out to maximize the stiffness of the shell.

Contributions from this work are:

- A topology optimization method that can find solutions to the concurrent optimization problem of composite, thin-shell structures with complex shapes and geometrical nonlinearities, while limiting the number of design variables to only 3, thus greatly restricting the computational cost of the analysis.

- A shape optimization method for fine tuning the contour of a single cutout on deployable thin shells.

- Fast and high-fidelity numerical simulations of the quasi-static folding behavior of thin, composite shells forming a corner that can accurately capture localized stress concentration.

- Experimental studies of the folding behavior of shells with cutouts derived from the optimization analysis that have demonstrated very good agreement with numerical simulations.

5.1.3 Size-Scaling Effects on Softening and Failure of Plain-Weave Astroquartz ® Laminates and Localized Damage Measurement

The behavior of thin, plain-weave composite material has been characterized and the first study of size-scaling effects at small length scales ($\leq$ 15 mm) in this type of material has been performed. Size-scaling effects on stiffness and strength have been introduced in numerical simulations of deployable thin shells. It has been shown that these effects influence the results of the failure analysis. First, the laminate stiffness and strength have been measured at macro-scale (12.7 mm - 15.0 mm). Then tensile tests of plain weave samples oriented at $\pm 45^\circ$ have been performed and a reduction of both shear stiffness and strength has been found in smaller samples. Finally, both numerical and experimental studies of deployable, thin shells forming a corner have been conducted and good agreement within the two has been found.

Contributions from this work are:

- Evidence that size-scaling effects in $\pm 45^\circ$ thin, plain-weave composites at length scales smaller than 15 mm produce a reduction in stiffness and strength of this type of material.

- Data demonstrating that these size effects influence the prediction of the onset of failure on deployable shell structures with cutouts forming small strips of material made of thin, plain-weave laminates.

- Measurement of localized damage in shells after quasi-static folding experiments that confirm the results from numerical simulations, which show the location on the shell where damage is predicted.

5.2 Future Work

The work reported in this thesis can be extended in several ways to improve upon current designs of deployable thin shells with cutouts. Key elements, which deserve

to be investigated further, have been identified in all three chapters, and suggestions for two future directions are provided here.

The first future direction concerns the optimization aspect of this research. Recent studies have proposed solutions to increase the computational efficiency of a density-based approach to topology optimization (Aage et al., 2017). Algorithms based on density distribution methods provide a very general approach to structural optimization because no assumptions are needed on the initial topology of the structure. Therefore, reducing the computational cost of these types of algorithms and applying them to more complex shapes of deployable thin shell structures would be extremely beneficial.

Additionally, the density-based algorithm proposed in this research uses a modified Solid Isotropic Material with Penalization (SIMP) approach to interpolate the stiffness tensor and studies are performed on shell structures made of isotropic material. The algorithm can be generalized to study more complex materials, such as fiber reinforced composites, which are more interesting for deployable space structures.

Finally, since an approximation has been made for the derivative of the global stress measure in deformed configuration, additional studies could be performed to determine whether more optimal solutions can be found without making this approximation. Current studies show that it is possible to efficiently assign local stress constraints and provide a sensitivity analysis of these constraints (Silva, Beck, and Sigmund, 2019a; Silva, Beck, and Sigmund, 2019b). These studies use a linear finite element analysis and further research is needed to generate solutions using a geometrically nonlinear formulation.

The second future direction concerns the failure analysis and material characterization aspect of this research. The failure criterion used in this study predicts the onset of failure on the shell, but the material model used in numerical simulation is not modified accordingly. For example, a crack propagation model could be used to propagate the numerical results once the maximum value of the failure index has reached its threshold value of 1.

Topology optimization methods that promote a design with a minimal amount of damaged material have been proposed (Verbart, Langelaar, and Van Keulen, 2016). A similar method could be applied to topology optimization of deployable shell structures once a model for damaged elements is introduced in the numerical simulations.

BIBLIOGRAPHY

Aage, N. et al. (2017). "Giga-voxel computational morphogenesis for structural design". In: *Nature* 550.2017–7674.

Allaire, G., F. Jouve, and A. M. Toader (2004). "Structural optimization using sensitivity analysis and a level-set method". In: *Journal of computational physics* 194.1, pp. 363–393.

Andreassen, E. and C. S. Andreasen (2014). "How to determine composite material properties using numerical homogenization". In: *Computational Materials Science* 83, pp. 488–495.

Andreassen, E., A. Clausen, et al. (2011). "Efficient topology optimization in MATLAB using 88 lines of code". In: *Structural and Multidisciplinary Optimization* 43.1, pp. 1–16.

Atkins, A. G. and R. M. Caddell (1974). "The laws of similitude and crack propagation". In: *International Journal of Mechanical Sciences* 16.8, pp. 541–548.

Bale, H. A. et al. (2013). "Real-time quantitative imaging of failure events in materials under load at temperatures above 1,600 C". In: *Nature materials* 12.1.

Banik, J. and T. Murphey (2010). "Performance validation of the triangular rollable and collapsible mast". In: *24th Annual AIAAUSU Conference on Small Satellites*.

Bar-Kochba, E. et al. (2015). "A fast iterative digital volume correlation algorithm for large deformations". In: *Experimental Mechanics* 55.1, pp. 261–274.

Barrett, R. et al. (2006). "Qualification of elastic memory composite hinges for spaceflight applications". In: *47th AIAA/ASME/ASCE/AHS/ASC Structures, Structural Dynamics, and Materials Conference*. 2006–2039.

Bay, B. K. (2008). "Methods and applications of digital volume correlation". In: *The Journal of Strain Analysis for Engineering Design* 43.8, pp. 745–760.

Bažant, Z. P. (2019). "Design of quasibrittle materials and structures to optimize strength and scaling at probability tail: an apercu". In: *Proc. R. Soc. A* 475.2018–0617.

Bažant, Z. P. and E. P. Chen (1999). "Scaling of structural failure". In: *Applied Mechanics Reviews ASME* 50.10, pp. 383–433.

Bažant, Z. P., J. J. H. Kim, et al. (1999). "Size effect on compression strength of fiber composites failing by kink band propagation". In: *International journal of Fracture* 95.103, pp. 1–4.

Bažant, Z. P. and J. L. Le (2017). *Probabilistic mechanics of quasibrittle structures: strength, lifetime, and size effect*. Cambridge University Press.

Bendsøe, M. P. and N. Kikuchi (1988). “Generating optimal topologies in structural design using a homogenization method”. In: *Computer methods in applied mechanics and engineering* 71.2, pp. 197–224.

Bendsøe, M. P. and O. Sigmund (2013). *Topology optimization: theory, methods, and applications*. Springer Science & Business Media.

Bendsoe, M. P. et al. (2005). “Topology optimization-broadening the areas of application”. In: *Control and Cybernetics* 34, pp. 7–35.

Bower, A. F. (2011). *Applied mechanics of solids*. CRC press.

Bruggi, M. and P. Venini (2008). “A mixed FEM approach to stress-constrained topology optimization”. In: *International Journal for Numerical Methods in Engineering* 73.12, pp. 1693–1714.

Bruns, T. E. and D. A. Tortorelli (1998). “Topology optimization of geometrically nonlinear structures and compliant mechanisms”. In: *7th AIAA/USAF/NASA/ISSMO Symposium on Multidisciplinary Analysis and Optimization*. 1998–4950.

– (2001). “Topology optimization of non-linear elastic structures and compliant mechanisms”. In: *Computer methods in applied mechanics and engineering* 190.26-27, pp. 3443–3459.

– (2003). “An element removal and reintroduction strategy for the topology optimization of structures and compliant mechanisms”. In: *International journal for numerical methods in engineering* 57.10, pp. 1413–1430.

Buhl, T., C. B. W. Pedersen, and O. Sigmund (2000). “Stiffness design of geometrically nonlinear structures using topology optimization”. In: *Structural and Multidisciplinary Optimization* 19.2, pp. 93–104.

Bullock, R. E. (1974). “Strength ratios of composite materials in flexure and in tension”. In: *Journal of Composite Materials* 8.2, pp. 200–206.

Carpinteri, A. and P. Bocca (1987). “Transferability of small specimen data to full-size structural components”. In: *Composite Materials Response: Constitutive Relations and Damage Mechanisms*, pp. 111–31.

Cho, S. and H. Jung (2003). “Design sensitivity analysis and topology optimization of displacement–loaded non-linear structures”. In: *Computer Methods in Applied Mechanics and Engineering* 192.22-24, pp. 2539–2553.

Chung, H. et al. (2019). “Topology optimization in OpenMDAO”. In: *Structural and multidisciplinary optimization* 59.4, pp. 1385–1400.

Daniel, I. M. and O. Ishai (1994). *Engineering mechanics of composite materials*. Vol. 3. Oxford university press New York.

De Leon, D. M. et al. (2015). “Stress-constrained topology optimization for compliant mechanism design”. In: *Structural and Multidisciplinary Optimization* 52.5, pp. 929–943.

Delgado, D. and D. Goods (2015). *JPL Orbit Pavilion*. URL: http://www.davidjdelgado.com/orbit-pavilion.

Diaz, A. and O. Sigmund (1995). "Checkerboard patterns in layout optimization". In: *Structural optimization* 10.1, pp. 40–45.

Dontchev, K. (2009). "Michigan Multipurpose MiniSat M-Cubed". In: *Summer CubeSat Workshop*. San Louis Obispo, CA, USA.

Duysinx, P. and M. P. Bendsøe (1998). "Topology optimization of continuum structures with local stress constraints". In: *International journal for numerical methods in engineering* 43.8, pp. 1453–1478.

Duysinx, P. and O. Sigmund (1998). "New developments in handling stress constraints in optimal material distribution". In: *7th AIAA/USAF/NASA/ISSMO symposium on multidisciplinary analysis and optimization*. 1998–4906.

Fleck, N. A. and B. Budiansky (1991). "Compressive failure of fibre composites due to microbuckling". In: *Inelastic deformation of composite materials*. Springer, pp. 235–273.

Footdale, J., J. Banik, and T. Murphey (2010). "Design developments of a non-planar deployable structure". In: *51st AIAA/ASME/ASCE/AHS/ASC Structures, Structural Dynamics, and Materials Conference*. 2010–2608.

Francis, W. et al. (2003). "Development and testing of a hinge/actuator using elastic memory composites". In: *44th AIAA/ASME/ASCE/AHS/ASC Structures, Structural Dynamics, and Materials Conference*. 2003–1496.

Gea, H. C. and J. Luo (2001). "Topology optimization of structures with geometrical nonlinearities". In: *Computers & Structures* 79.20-21, pp. 1977–1985.

Geiss, M. J. et al. (2019). "Combined Level-Set-XFEM-Density Topology Optimization of Four-Dimensional Printed Structures Undergoing Large Deformation". In: *Journal of Mechanical Design* 141.5.

Greschik, G. (1996). "Deployment of dishes with surface discontinuities". In: *Journal of spacecraft and rockets* 33.4, pp. 569–574.

Guilherme, C. E. M. and J. S. O. Fonseca (2007). "Topology optimization of continuum structures with epsilon-relaxed stress constraints". In: *Alves M, da Costa Mattos HS (eds) Solid Mechanics in Brazil* 1, pp. 239–250.

Haftka, R. T. and R. V. Grandhi (1986). "Structural shape optimization—a survey". In: *Computer methods in applied mechanics and engineering* 57.1, pp. 91–106.

Haplin, J. C. and S. W. Tsai (1969). *Effect of environmental factors on composite materials*.

Hashin, Z. and A. Rotem (1973). "A fatigue failure criterion for fiber reinforced materials". In: *Journal of composite materials* 7.4, pp. 448–464.

Jackson, K. E., S. Kellas, and J. Morton (1992). “Scale effects in the response and failure of fiber reinforced composite laminates loaded in tension and in flexure”. In: *Journal of composite materials* 26.18, pp. 2674–2705.

Jain, A. K. (1989). *Fundamentals of digital image processing*. Englewood Cliffs, NJ: Prentice Hall,

Jog, C. S. and R. B. Haber (1996). “Stability of finite element models for distributed-parameter optimization and topology design”. In: *Computer methods in applied mechanics and engineering* 130.3-4, pp. 203–226.

JPS, Composite Materials (2017). *"JPS Technical Reference Handbook"*. 2200 South Murray Avenue, P.O. Box 2627, Anderson, SC, 29622.

Le, C. et al. (2010). “Stress-based topology optimization for continua”. In: *Structural and Multidisciplinary Optimization* 41.4, pp. 605–620.

Liu, L. and E. F. Morgan (2007). “Accuracy and precision of digital volume correlation in quantifying displacements and strains in trabecular bone”. In: *Journal of biomechanics* 40.15, pp. 3516–3520.

Lund, E. (2009). “Buckling topology optimization of laminated multi-material composite shell structures”. In: *Composite Structures* 91.2, pp. 158–167.

Mallikarachchi, H. M. Y. C. and S. Pellegrino (2010). “Optimized Designs of Composite Booms with Tape Spring Hinges”. In: *51st AIAA/ASME/ASCE/AHS/ASC Structures, Structural Dynamics, and Materials Conference*. 2010–2750.

– (2011). “Quasi-static folding and deployment of ultrathin composite tape-spring hinges”. In: *Journal of Spacecraft and Rockets* 48.1, pp. 187–198.

– (2013). “Failure criterion for two-ply plain-weave CFRP laminates”. In: *Journal of Composite Materials* 47.11, pp. 1357–1375.

Maute, K. and E. Ramm (1997). “Adaptive topology optimization of shell structures”. In: *AIAA journal* 35.11, pp. 1767–1773.

Maute, K., A. Tkachuk, et al. (2015). “Level set topology optimization of printed active composites”. In: *Journal of Mechanical Design* 137.11.

Mobrem, M. and D. Adams (2009a). “Deployment analysis of the lenticular jointed antennas onboard the mars express spacecraft”. In: *Journal of Spacecraft and Rockets* 46.2, pp. 394–402.

– (2009b). “Lenticular jointed antenna deployment anomaly and resolution onboard the Mars Express spacecraft”. In: *Journal of Spacecraft and Rockets* 46.2, pp. 403–410.

Mobrem, M., L. Peterson, et al. (2017). “An Evaluation of Structural Analysis Methodologies for Space Deployable Structures”. In: *4th AIAA Spacecraft Structures Conference*. 2017–0851.

Murphey, T. W. et al. (2015). “High strain composites”. In: *2nd AIAA Spacecraft Structures Conference*. 2015–0942.

Nguyen, M. H. et al. (2019). “Particle Toughened Interfaces Enhance Mechanical Response of Composites”. In: *AIAA Scitech 2019 Forum*. 2019–1041.

NTPT, North Thin Ply Technology (2018). *"ThinPreg^{TM} 380CE uni-directional carbon fibers impregnated with a cyanate ester resin system"*. Chemin du Closel 3, 1020 Renens, Switzerland.

Osher, S. J. and F. Santosa (2001). “Level set methods for optimization problems involving geometry and constraints: I. Frequencies of a two-density inhomogeneous drum”. In: *Journal of Computational Physics* 171.1, pp. 272–288.

Osher, S. and J. A. Sethian (1988). “Fronts propagating with curvature-dependent speed: algorithms based on Hamilton-Jacobi formulations”. In: *Journal of computational physics* 79.1, pp. 12–49.

Pajot, J. M. and K. Maute (2006). “Analytical sensitivity analysis of geometrically nonlinear structures based on the co-rotational finite element method”. In: *Finite Elements in Analysis and Design* 42.10, pp. 900–913.

Paris, J. et al. (2009). “Topology optimization of continuum structures with local and global stress constraints”. In: *Structural and Multidisciplinary Optimization* 39.4, pp. 419–437.

PATZ, Materials & Technologies (2019). *"PMT-F6 toughened cyanate ester resin system"*. 4968 Industrial Way, Benicia, CA 94510.

Pedersen, C. B. W., K. Bose, et al. (2017). “Latest Developments for Industrial Adjoint Sensitivity Analysis and Non-Parametric Optimization”. In: *12th World Congress on Structural and Multidisciplinary Optimization*.

Pedersen, C. B. W., T. Buhl, and O. Sigmund (2001). “Topology synthesis of large-displacement compliant mechanisms”. In: *International Journal for numerical methods in engineering* 50.12, pp. 2683–2705.

Pellegrino, S. (2015). “Folding and deployment of thin shell structures”. In: *Extremely deformable structures*. Springer, pp. 179–267.

Pereira, J. T., E. A. Fancello, and C. S. Barcellos (2004). “Topology optimization of continuum structures with material failure constraints”. In: *Structural and Multidisciplinary Optimization* 26.1-2, pp. 50–66.

Perez, R. E., P. W. Jansen, and J. R. R. A. Martins (2012). “pyOpt: a Python-based object-oriented framework for nonlinear constrained optimization”. In: *Structural and Multidisciplinary Optimization* 45.1, pp. 101–118.

Peterson, L. and M. Mobrem (2017). “Structural Analysis Methodology for Space Deployable Structures using a High Performance Parallel Nonlinear Finite Element Solver”. In: *4th AIAA Spacecraft Structures Conference*. 2017–0852.

Powell, M. (1994). “A direct search optimization method that models the objective and constraint functions by linear interpolation”. In: *Advances in optimization and numerical analysis*. Springer, pp. 51–67.

Rafsanjani, A., L. Jin, et al. (2019). “Propagation of pop ups in kirigami shells”. In: *Proceedings of the National Academy of Sciences* 116.17, pp. 8200–8205.

Rafsanjani, A., Y. Zhang, et al. (2018). “Kirigami skins make a simple soft actuator crawl”. In: *Science Robotics* 3.15, eaar7555.

Rimrott, F.P.J. (1966). “Storable tubular extendible members”. In: *Engineering Digest*.

Rupp, C. J. et al. (2009). “Design of piezoelectric energy harvesting systems: a topology optimization approach based on multilayer plates and shells”. In: *Journal of Intelligent Material Systems and Structures* 20.16, pp. 1923–1939.

Saxena, A. and G. K. Ananthasuresh (2001). “Topology synthesis of compliant mechanisms for nonlinear force-deflection and curved path specifications”. In: *Journal of mechanical Design* 123.1, pp. 33–42.

Sethian, J. A. and A. Wiegmann (2000). “Structural boundary design via level set and immersed interface methods”. In: *Journal of computational physics* 163.2, pp. 489–528.

Sigmund, O. (2000). “A new class of extremal composites”. In: *Journal of the Mechanics and Physics of Solids* 48.2, pp. 397–428.

– (2001). “A 99 line topology optimization code written in Matlab”. In: *Structural and multidisciplinary optimization* 21.2, pp. 120–127.

– (2007). “Morphology-based black and white filters for topology optimization”. In: *Structural and Multidisciplinary Optimization* 33.4-5, pp. 401–424.

Sigmund, O. and K. Maute (2013). “Topology optimization approaches”. In: *Structural and Multidisciplinary Optimization* 48.6, pp. 1031–1055.

Sigmund, O. and J. Petersson (1998). “Numerical instabilities in topology optimization: a survey on procedures dealing with checkerboards, mesh-dependencies and local minima”. In: *Structural optimization* 16.1, pp. 68–75.

Sigmund, O. and S. Torquato (1996). “Composites with extremal thermal expansion coefficients”. In: *Applied Physics Letters* 69.21, pp. 3203–3205.

Silva, G. A. da, A. T. Beck, and O. Sigmund (2019a). “Stress-constrained topology optimization considering uniform manufacturing uncertainties”. In: *Computer Methods in Applied Mechanics and Engineering* 344, pp. 512–537.

– (2019b). “Topology optimization of compliant mechanisms with stress constraints and manufacturing error robustness”. In: *Computer Methods in Applied Mechanics and Engineering*.

Soykasap, O. (2006). “Micromechanical models for bending behavior of woven composites”. In: *Journal of Spacecraft and Rockets* 43.5, pp. 1093–1100.

– (2009). “Deployment analysis of a self-deployable composite boom”. In: *Composite Structures* 89.3, pp. 374–381.

Stabile, A. and S. Laurenzi (2014). “Coiling dynamic analysis of thin-walled composite deployable boom”. In: *Composite Structures* 113, pp. 429–436.

Standard D3039/D3039M, ASTM (2009). *"Standard test method for tensile properties of polymer matrix composite materials"*. American Society for Testing and Materials.

Standard D3518/D3518M, ASTM (2007). *"Standard test method for in-plane shear response of polymer matrix composite materials by tensile test of a* $\pm 45^\circ$ *laminate"*. American Society for Testing and Materials.

Standard D6272-02, ASTM (2008). *"Standard test method for flexural properties of unreinforced and reinforced plastics and electrical insulating materials by four point bending"*. American Society for Testing and Materials.

Stock, S. R. (2008). “Recent advances in X-ray microtomography applied to materials”. In: *International Materials Reviews* 53.3, pp. 129–181.

Sutton, M. A., J. J. Orteu, and H. Schreier (2009). *Image correlation for shape, motion and deformation measurements: basic concepts, theory and applications*. Springer Science & Business Media.

Svanberg, K. (1987). “The method of moving asymptotes—a new method for structural optimization”. In: *International journal for numerical methods in engineering* 24.2, pp. 359–373.

Tan, L. T. and S. Pellegrino (2006). “Thin-shell deployable reflectors with collapsible stiffeners Part 1: approach”. In: *AIAA journal* 44.11, pp. 2515–2523.

Tortorelli, D. A. and P. Michaleris (1994). “Design sensitivity analysis: overview and review”. In: *Inverse problems in Engineering* 1.1, pp. 71–105.

Townsend, S. and H. A. Kim (2019). “A level set topology optimization method for the buckling of shell structures”. In: *Structural and Multidisciplinary Optimization*, pp. 1–18.

Tsai, S. W. and E. M. Wu (1971). “A general theory of strength for anisotropic materials”. In: *Journal of composite materials* 5.1, pp. 58–80.

Verbart, A., M. Langelaar, and F. Van Keulen (2016). “Damage approach: A new method for topology optimization with local stress constraints”. In: *Structural and Multidisciplinary Optimization* 53.5, pp. 1081–1098.

Wang, A. S. D., R. W. Tung, and B. A. Sanders (1980). “Size effect on strength and fatigue of a short fiber composite material”. In: *Emerging technologies in aerospace structures, design, structural dynamics and materials*, pp. 37–52.

Wang, F. et al. (2014). “Interpolation scheme for fictitious domain techniques and topology optimization of finite strain elastic problems”. In: *Computer Methods in Applied Mechanics and Engineering* 276, pp. 453–472.

Wang, M. Y., X. Wang, and D. Guo (2003). “A level set method for structural topology optimization”. In: *Computer methods in applied mechanics and engineering* 192.1-2, pp. 227–246.

Watt, A. M. and S. Pellegrino (2002). “Tape-spring rolling hinges”. In: *36th Aerospace Mechanisms Symposium*. Glenn Research Center, Cleveland, OH, USA, 15–17 May 2002.

Weibull, W. (1939). “A statistical theory of strength of materials”. In: *IVB-Handl.*

Wisnom, M. R. (1991). “Relationship between strength variability and size effect in unidirectional carbon fibre/epoxy”. In: *Composites* 22.1, pp. 47–52.

Withey, P. A. (1997). “Fatigue failure of the de Havilland comet I”. In: *Engineering failure analysis* 4.2, pp. 147–154.

Xu, F. (2018). “Quantitative characterization of deformation and damage process by digital volume correlation: A review”. In: *Theoretical and Applied Mechanics Letters* 8.2, pp. 83–96.

Ye, Q. et al. (2019). “Topology optimization of conformal structures on manifolds using extended level set methods (X-LSM) and conformal geometry theory”. In: *Computer Methods in Applied Mechanics and Engineering* 344, pp. 164–185.

Yee, J. C. H. and S. Pellegrino (2005). “Folding of woven composite structures”. In: *Composites Part A: Applied Science and Manufacturing* 36.2, pp. 273–278.

Yoon, G. H. and Y. Y. Kim (2005). “Element connectivity parameterization for topology optimization of geometrically nonlinear structures”. In: *International journal of solids and structures* 42.7, pp. 1983–2009.

Zweben, C. (1981). “The effect of stress nonuniformity and size on the strength of composite materials”. In: *Journal of Composites, Technology and Research* 3.1, pp. 23–26.

Appendix A

SILICONE MOLDING MANUFACTURING TECHNIQUE

A novel manufacturing technique was developed to build thin shells forming a corner. Silicone rubber was used to build the internal (male) and external (female) molds needed to support, shape, and apply pressure on a composite layup. An investigation into different silicone materials resulted in the final use of Mold Max XLS II liquid silicone rubber, from Reynolds Advanced Materials. This material has acceptable pour time (40 min), low mixed viscosity (30,000 cP), and low impact cost on the manufacturing procedure. Silicone rubber thinning fluid, from the same vendor, was also added as 5% of the total weight to lower the viscosity.

The steps involved in manufacturing the silicone molds are shown in Fig. A.1. The male mold is composed of an intersection piece and two cylindrical tubes. The tree parts are connected through two internal aluminum rods. A 3D printed, L-shaped mandrel is used to build the mold intersection piece. The piece features a smooth joint between the two cylindrical surfaces and two holes that do not connect at the center, thus leaving a small, solid silicone region. The holes host the two thinner aluminum rods, which connect the intersection piece to the two tubes. Uncured silicone rubber, with low viscosity, was poured with a syringe through a small, circular cavity placed in one of the caps of the 3D printed mandrel. The silicone was then cured at room temperature for 24 hours. Afterwards, the resulting silicone part was easily removed from its mandrel.

The tubes are hollow cylinders obtained pouring silicone into a mandrel built with 3D printed base and top caps and commercially available materials. The same curing process was applied. The female mold was built of two identical components, which were used to enclose the layup. A low-density foam mandrel and an aluminum cage were used to manufacture each component. The silicone rubber molds can be reused multiple times.

The composite manufacturing procedure is shown in Fig. A.2. Pre-impregnated fiber is assembled directly on the male mold, which is stiff enough to provide support for assembling the layup. The stiffness comes from the two aluminum rods that run through its core. One ply of the layup is cut into four geometric patterns, thus creating overlapping strips of material along the axial direction of each tube. Subsequent

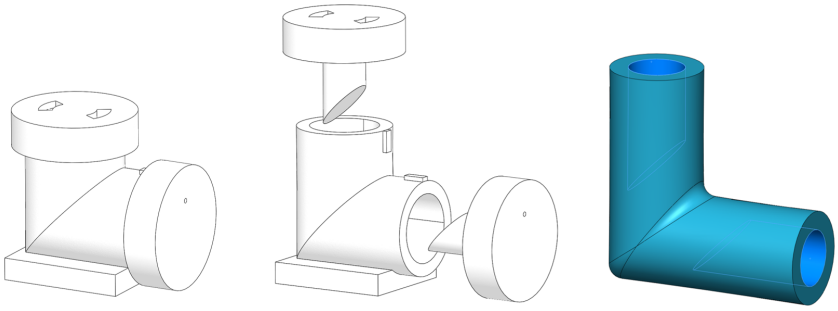

(a) Design of L-shaped, 3D printed mandrel used to build the intersection of a male silicone mold.

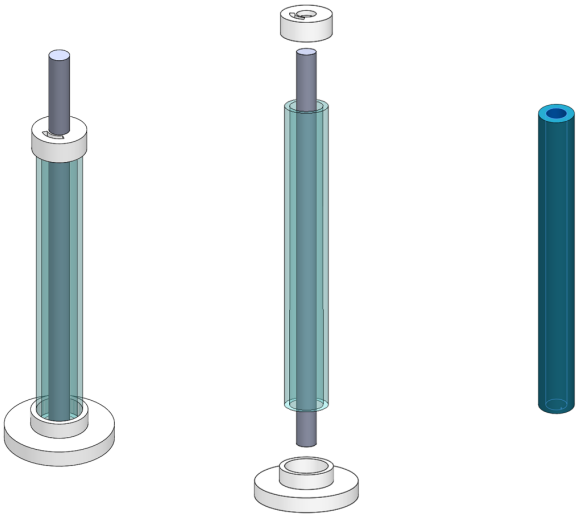

(b) Assembly of 3D printed caps and commercially available hollow tubes used to build two tubes of a male silicone mold.

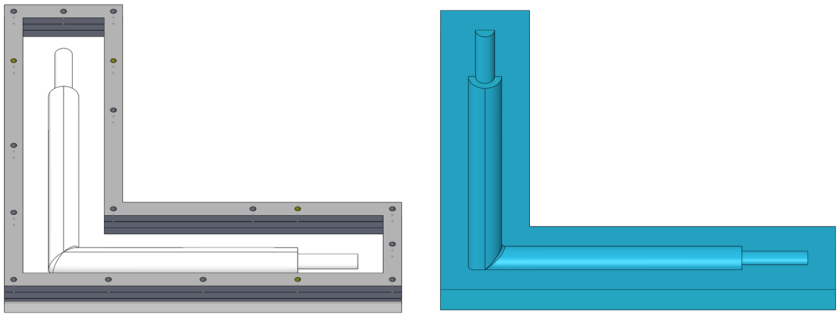

(c) Assembly of low-density foam base and aluminum cage used to build two halves of a female silicone mold.

Figure A.1: Design of mandrels used to build male and female silicone molds.

plies are assembled following an identical procedure. The male mold and the composite layup are positioned inside the female mold. An external aluminum cage is used to constrain the expansion of the silicone during the curing process. The high coefficient of thermal expansion of the silicone makes it expand much

more compared to the aluminum cage when subjected to high temperatures. This provides enough pressure for the layup to cure without the need of an autoclave. A high temperature, 180°C, curing cycle performed in oven completes the curing process. Once the cure is complete, the aluminum rods can be removed and the silicone mold, remaining inside the composite, is compliant enough to be squeezed out.

An example of thin shells built using this manufacturing technique is shown in Fig. A.3.

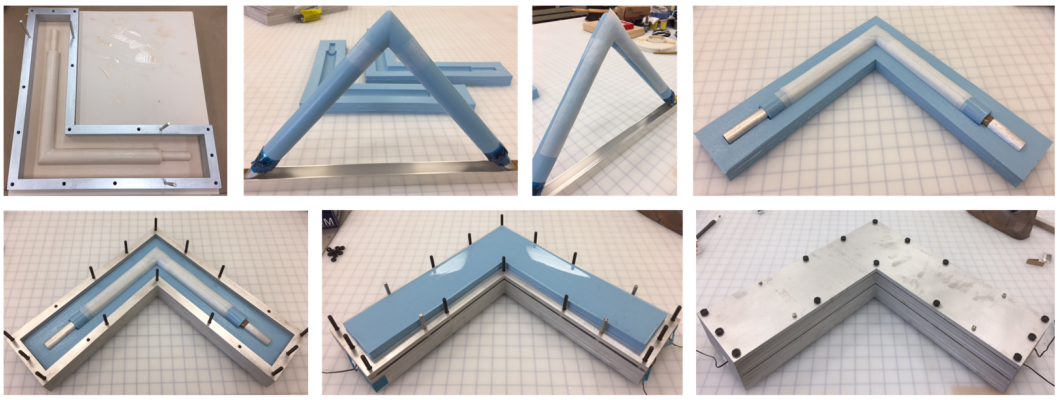

Figure A.2: Composite manufacturing procedure to build thin shells forming a corner.

Figure A.3: Example of thin shell built using the silicone molding manufacturing technique.